The investigation of geothermal temperature anomalies and structures using airborne TIR and LiDAR data: a case study in Bajawa area, Indonesia

MUHAMMAD REZA RAMDHAN
February, 2019

SUPERVISORS:
Dr. Christoph Hecker
Dr. Francesco Nex

The investigation of geothermal temperature anomalies and structures using airborne TIR and LiDAR data: a case study in Bajawa area, Indonesia
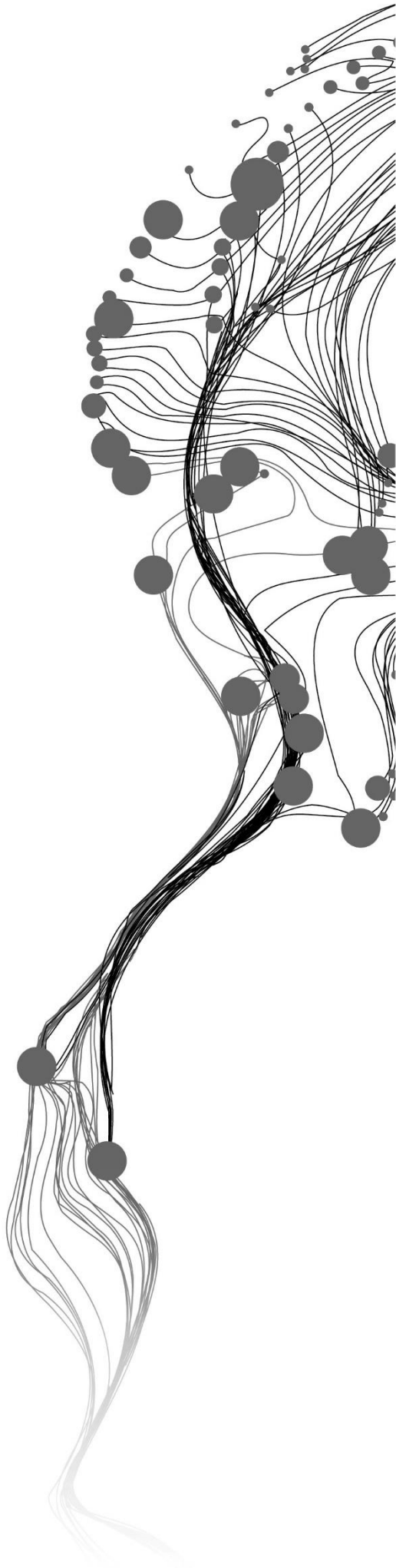
MUHAMMAD REZA RAMDHAN
Enschede, The Netherlands, February, 2019

Thesis submitted to the Faculty of Geo-Information Science and Earth Observation of the University of Twente in partial fulfilment of the requirements for the degree of Master of Science in Geo-information Science and Earth Observation.
Specialization: Applied Earth Sciences – Geological Remote Sensing

SUPERVISORS:
Dr. Christoph Hecker
Dr. Francesco Nex

THESIS ASSESSMENT BOARD:
Prof. Dr. M. van der Meijde (Chair)
Dr. Fred Beekman (External Examiner, Utrecht University)

ABSTRACT

Surface temperature anomalies and geologic structures are essential indicators of geothermal potential in the subsurface. Many remote sensing data from spaceborne platforms have been used to investigate these indicators. However, a typical coarse-spatial resolution is found as a prominent limitation of satellite imageries to detect geothermal temperature anomalies and geologic structures on a detailed scale. In this research, integration of high-resolution airborne remote sensing including thermal infrared (TIR) and Light Detection and Ranging (LiDAR) data was used for the first time to investigate the surface geothermal indicators in Bajawa area, Indonesia. This research was carried to evaluate whether the integration of TIR and LiDAR data is technically reliable and could provide additional information to the traditional 3G survey (geology, geophysics, and geochemistry) for geothermal resource exploration.

In this research, we successfully processed more than 8000 TIR images derived from FLIR x6570sc camera into a consistent orthoimage using a fully automatic IBM workflow. The level of accuracy is approximately 5 meters for the horizontal and vertical direction and therefore considered suitable for geothermal anomaly mapping. Secondly, we performed Decision Tree Classification (DTC) to suppress the false positives and detect the true geothermal anomalies with an overall classification accuracy of 87.9%. The results are consistent with the ground truth in Mataloko Geothermal Field (MGF) containing hot springs, fumaroles, mud pools, and steaming-grounds with temperature variation between 34-95°C. These manifestations align with the pattern and density of the lineaments that were automatically extracted from LiDAR DEM using the modified Multi-Hillshade Hierarchic Clustering (MHHC) workflow.

We integrated the results with the geological and geophysical data from literature and could not confirm an earlier proposed NW-SE Wae Luja fault, but rather found a strong indication of NE-SW oriented structures in the alignment of the surface manifestations and the lineaments pattern. This NE-SW trend consistent with the regional structures described for Flores Island, besides it also correlates with the extension of Hg soil anomaly and with the shallow fractured zones reported in drilling result of well MT-1 and MT-2 in MGF. We interpret this NE-SW trend as shallow structures that control the secondary pathway of geothermal fluids in MGF. We conclude that the integration of the airborne TIR and LiDAR data provides a new understanding to the geothermal system in MGF and promising to support the 3G survey at reconnaissance as well as a developmental stage of geothermal energy resources.

ACKNOWLEDGMENTS

TABLE OF CONTENTS

LIST OF FIGURES

LIST OF TABLES

LIST OF APPENDIXES

LIST OF ABBREVIATIONS

ALS	Aerial Laser Scanner
ASTER	Advanced Spaceborne Thermal Emission and Reflection Radiometer
BBA	Bundle Block Adjustment
COP	The Conference of the Parties
DC	Direct Current
DEM	Digital Elevation Model
DHS	Dynamic Histogram Stretching
DoD	DSM of Difference
DSM	Digital Surface Model
DTC	Decision Tree Classification
DTF	Dynamic Threshold Filter
ESA	European Space Agency
FLIR	Forward-looking Infrared
FOV	Field of View
GCM	Grouping analysis for Cluster Mapping
GEOCAP	The Geothermal Capacity Building Programme
GPS	Global Positioning System
GSD	Ground Sampling Distance
GW	Gigawatt
HSV	Horizontal Shift Vector
IBM	Image-Based Modeling
IMU	Inertial Measurement Unit
IRIG	Inter-Range Instrumentation Group
LDM	Linear Directional Mean
LiDAR	Light Detection and Ranging
MGF	Mataloko Geothermal Field
MHHC	Multi-Hillshade Hierarchic Clustering
MHz	Megahertz
MW	Megawatt
OHT	Optimised Hough Transformation
SfM	Structure from Motion
SIFT	Scale Invariant Feature Transform
SRTM	Shuttle Radar Topography Mission
STA	Segment Tracing Algorithm
TIR	Thermal Infrared
UAV	Unmanned Aerial Vehicle

1. INTRODUCTION

1.1. Background

Geothermal energy is an essential backbone for the world's sustainable energy sources. Its development has been increasingly important to diminish the greenhouse emission after the historic agreement among the nations in Paris Climate Conference - COP 21 (Cagatay, 2015). Over 24 countries are currently producing electricity from geothermal energy with a total installed capacity of 14 gigawatts (GW) with the main contribution from the United States, Indonesia, Philippines, Turkey, and New Zealand (Richter, 2018a). In 2021, the world geothermal capacity is expected to rise to approximately 17 GW (The World Bank, 2018).

Indonesia is currently producing 1.9 GW of electricity from geothermal energy. The production will potentially grow to 3.7 GW over the next five years, surpass the United States as the world's largest geothermal power producer (Richter, 2018a). This increase will be focused on the lesser developed area in Eastern Indonesia to boost their economic and infrastructure growth, such as Flores Island which currently needs more baseload energy to support their emerging tourism and growing population.

Several studies have been conducted to explore the geothermal resources in Flores. Pioneering study was carried out by the Indonesia-Japan Research Cooperation Program in 1997-2002 which included 3G surveys (geology, geophysics, and geochemistry) and shallow exploration wells drilling. These surveys have yielded the conceptual model of the geothermal system and the reserves characteristic in the Bajawa area (Central Flores), as it published by Akasako et al. (2002); Muraoka et al. (2005); and Nanlohy et al. (2001). They suggested some high enthalpy geothermal prospects in the Bajawa area as a part of volcanic rift zone which is controlled by *en échelon* structures as subduction products of the Australian Plate with the lesser Sunda-Banda Arc.

As a lesson learned from the former studies, high risk and uncertainty in the early stages of exploration are the main issues for geothermal development in the frontier field like Flores Island. According to IFC (2013), during the early stages, the success rate of exploration is approximately 50% in most of the geothermal field, it means one out of two geothermal projects fails in this phase. Therefore, every effort through the most current cutting-edge technologies and techniques like remote sensing are necessary to reduce the risks and costs as well as increase the success rates of geothermal exploration.

New insight to boost geothermal exploration in Flores has been carried through the collaborative project between Indonesia and the Netherlands for Geothermal Capacity Buildings (GEOCAP). This project has acquired airborne remote sensing data using the thermal infrared (TIR) camera together with Light Detection and Ranging (LiDAR) sensor over the Bajawa area in Central Flores. This thesis which is a part of GEOCAP project mark out the first use of an integration of airborne TIR and LiDAR data for geothermal exploration in Indonesia, particularly on Flores island.

1.1.1. Remote sensing for geothermal exploration

Remote sensing has been recognized as a viable tool for geothermal exploration. It has primary advantages in minimizing the cost and effort of ground-based surveys. It can give valuable information such as surface temperature anomalies and structural control of the earth surfaces that could lead to the findings of geothermal surface expressions and ultimately to locate new geothermal prospect areas. There are three types of remote sensing platform used for geothermal exploration, namely satellite-borne, airborne, and Unmanned Aerial Vehicle (UAV).

Several studies have been carried out for geothermal exploration using satellite imageries. For example, Hecker et al. (2017) examined the used of multi-source satellite remote sensings such as Advanced Spaceborne Thermal Emission and Reflection Radiometer (ASTER) and Shuttle Radar Topography Mission (SRTM) for targeting the geothermal anomaly in Flores Island. This research inferred that the low spatial resolution has been a prominent limitation of satellite imageries because most of the geothermal anomalies are relatively small as compared to the image pixel size. Besides, structural detection using SRTM likely included the general trends of geomorphological features rather than faults or fractures.

On the other hand, a very high spatial resolution data could be acquired using UAV platform. For example, UAV has been used for monitoring geothermal heat flux and detecting temperature anomalies of a geothermal field in New Zealand (Harvey et al., 2016; Harvey & Luketina, 2014). Throughout these studies, UAV has the advantage to provide a very high spatial (less than 10 cm) and temporal resolution images (possibly in order of the day). However, UAV platforms are still limited to small survey areas due to the limitation with power and maximum flight distance.

The intermediate platform like airborne remote sensing is the most appropriate tool for a large but detail geothermal prospection. The airborne-based images provide a sub-meter spatial resolution that is suitable for the detection of geothermal manifestations with small size (Haselwimmer & Prakash, 2013). Moreover, the airborne platform could also be equipped with a LiDAR sensor that has the advantage to generate a digital elevation model (DEM) with high resolution and accuracy (Jaworowski et al., 2010).

1.1.2. Measurable indicators by remote sensing

Temperature anomalies and geological structures at the surface are good indicators of geothermal potential in the subsurface. According to Van der Meer et al. (2014), these indicators could be retrieved through remote sensing instruments as indirect evidence to geothermal activity underneath the earth's surface. Besides, surface temperature anomalies and structures are essential as the analog of the geothermal reservoir condition and geothermal fluid pathways (Curewitz & Karson, 1997; Haselwimmer & Prakash, 2013). However, the link between the surface indicators to the subsurface features requires further geologic interpretation in particular coupling the remote sensing data with the subsurface geophysics (Van der Meer et al., 2014).

Geothermal temperature anomalies have been described as heat anomalies associated with the occurrence of geothermal manifestation such as fumaroles, geysers, and hot springs (Varghese, 2016). These anomalies are manifests of the elevated geothermal heat which transferred to the earth's surface through the convection of ground waters in the permeable rocks or structures. Moreover, there are also manifestations that occurred due to the conductive heat loss such as steaming grounds (Haselwimmer & Prakash, 2013). The temperature of geothermal fluids has a considerable range depending on the type of geothermal systems. The water-dominated system usually has a temperature lower than 90°C. Meanwhile, the vapor-dominated system varies from intermediate temperature, around 90-150°C to a high temperature, around 150-240°C (Stober & Bucher, 2013).

With the term "Structures" we refer in this thesis to the geological faults and fractures related to geothermal systems. Structures are a principal indicator of geothermal potential because they create a secondary permeability for the circulation of geothermal fluids (Houwers et al., 2015). Structures can enhance the permeability of rocks several times depending on their geometry and kinematic types. Typically, fractured rock has a permeability $10^1 - 10^{-3}$ Darcy, meanwhile non-fractured rock has a lower bulk permeability which is $10^{-4} - 10^{-17}$ Darcy and $10^{-2} - 10^{-11}$ Darcy for crystalline rock and sedimentary rocks, respectively (Curewitz & Karson, 1997).

1.2. Research problems

This research focuses on solving technical as well as geoscientific problems. The former is related to the production of geometrically corrected orthoimage of a newly acquired airborne TIR dataset. With the research area being vast and rural (mostly covered by mountainous terrains and dense forests) and with the TIR images having lower contrast than optical images (in the visible range), this process is challenging. It is not understood how this landcover setting would affect the quality of airborne TIR orthoimages. Moreover, processing large amounts of thermal images is labor-intensive and time-consuming. Therefore, an automatic approach like Image-Based Modeling (IBM) is essential to be used as an alternative to the traditional photogrammetry method. However, the reliability of the IBM method for airborne data with this specific thermal sensor (FLIR x6570sc) and the rural landscape is still unknown.

The second focus is on the detection of geothermal temperature anomalies using airborne TIR orthoimages. Coolbaugh et al. (2007) highlighted that the temperature anomalies detection using remote sensing imageries is not straightforward due to false positives that can be created by soil moisture, vegetation, illumination condition, and topographic effect. These factors could lead to the misinterpretation of elevated surface temperatures as geothermal anomalies. Several studies have investigated these effects to the geothermal anomaly detection using satellite remote sensing (e.g., Coolbaugh et al., 2007; Eneva & Coolbaugh, 2009; Gutiérrez et al., 2012; Varghese, 2016). However, it is not understood how these variables influence the detectability of geothermal temperature anomalies at the scale of airborne TIR images.

The third focus is to examine the structural control of a geothermal system using airborne LiDAR data. Although many studies have demonstrated the use of LiDAR data for detail structural mapping, most of them still rely on the manual interpretation, which is arguably prone to bias and inconsistency that could lead to different interpretations of the controlling structure of a geothermal system. On the other hand, some automated methods are emerging popular for structural analysis using remote sensing data, such as Segment Tracing Algorithm (STA), Optimised Hough Transformation (OHT), LINE module (Šilhavy et al., 2016). However, these automated approaches only focused on line detection but not fully developed for the filtering and quantification of the lineaments. Therefore, an integrated automatic workflow is in high demand for the effectiveness and reproducibility of structural analysis.

Lastly, the link between these two indicators (temperature anomalies and structures) with the subsurface geothermal features in the study area is still unknown. Therefore, the integrated interpretation of the airborne data, ground-data, and subsurface data are necessary to extract information about the subsurface geothermal reservoir and fluid pathways. This relationship is tested whether the surface indicators identified from airborne data can provide additional information to characterize the subsurface geothermal feature such as a reservoir and a fluid pathway.

1.3. Research objectives

The main objective of this thesis is to evaluate the airborne TIR and LiDAR data for the detection of geothermal temperature anomalies and structures as predictors of subsurface geothermal potential. The following objectives and research questions were addressed:

1. To evaluate the reliability of Image-Based Modeling (IBM) approach to produce airborne TIR data in a vast and mountainous area with dense vegetation cover.
2. To map geothermal temperature anomalies using airborne TIR data in the research area
3. To identify the geological structures using airborne LiDAR data in the research area
4. To assess the relationship between geothermal temperature anomalies and surface structures as predictors for the geothermal reservoir and fluid pathways in the research area

1.4.   Research questions

1. What is the horizontal and vertical accuracy of the airborne TIR orthoimage product derived from IBM?
2. How significant is the influence of internal camera parameters and external parameters (terrain, flying height, side overlap, and land cover type) to the reliability of IBM on producing orthoimage from airborne TIR data?
3. What is the typical temperature and size of the surface temperature anomalies? Which types of geothermal manifestations are associated with these features?
4. How to differentiate the geothermal temperature anomalies from non-geothermal (false) anomalies?
5. What are the orientations and the density of the identified surface structures? How do they relate to the occurrence of geothermal temperature anomalies?
6. How do the geothermal temperature anomalies and surface structures link with the subsurface features? What additional information can be provided by this link to predict geothermal reservoir condition and fluid pathways in the subsurface of the research area?

1.5.   Thesis structure

This thesis consists of a total of eight chapters. Since it contains a broad topic, the specific topics are written separately in three chapters containing basic theory, methodology, and results. The detailed description of each chapter is given below:

- **Chapter 1** provides a general introduction to this thesis including the backgrounds, research problems, research objectives, and research questions.
- **Chapter 2** highlighted the location of the case study and provided an overview of the geology and geothermal system of the study area.
- **Chapter 3** describes the underlying theory, methodology, and results of airborne TIR orthoimages production using the IBM workflow. The quality assessment of the orthoimage product is also presented here.
- **Chapter 4** describes the methodology and results of the geothermal temperature anomalies detection using airborne TIR orthoimages derived from Chapter 3. This chapter also describes the process of the production of input variables such as albedo, hillshade, and landcover images.
- **Chapter 5** describes the methodology and results of geological structures analysis from LiDAR DEM using automatic workflow.
- **Chapter 6** describes the integrated interpretation of the results of Chapter 4 and 5 with geophysical data to evaluate the relationship between the surface and subsurface anomalies.
- **Chapter 7** includes a discussion of the results from Chapters 3-6.
- **Chapter 8** provides conclusions and recommendations for future research.

2.   STUDY AREA AND DATASETS

2.1.   Study area

The study area lies in Bajawa area, capital of Ngada district in Flores Island (Fig 2.1). Bajawa is the highest town in Flores (about 1500 m above sea level). It could be reached using airplane from Kupang or using bus via Ruteng, East Nusa Tenggara. The study area itself is divided into two main blocks. The first is Inielika area (Block A), which extends north of Bajawa with an approximate area of 15 km². The second is Mataloko area (Block B) with an approximate area of 43 km². The general Bajawa area has at least four prospect locations of geothermal potential including the Gou, Nage, Wolo Bobo, and Mataloko area. However, only Mataloko area is included in this research since the airborne LiDAR data does not cover the other three prospect locations.
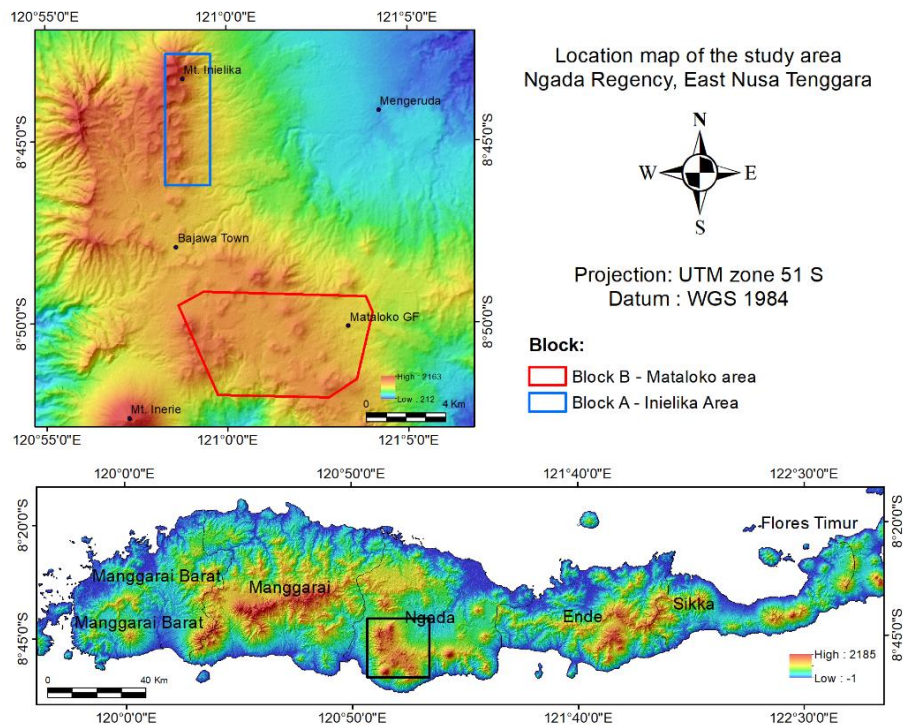
Figure 2.1 Location maps of the study area in Ngada Regency draped above SRTM DEM with hillshade effect using N45°E illumination azimuth. The map at the top is a spatial zoom of area highlighted by black box on the map at the bottom side.

2.1.1.   The tectonic configuration of the study area

The Bajawa area is a part of the volcanic rift zone that formed due to subduction between the Indo-Australian Plate with the Lesser Sunda-Banda Arc (Muraoka et al., 2002). This area is characterized by NNW–SSE left lateral shear stress regime which formed *en échelon* structures with the main orientation NE–SW along the Flores Island and the eastern island including Solor, Lembata, Pantar, and Alor (see Fig 2.2). An *en échelon* element that is crossing Bajawa area shows a combination between a large-scale anticline structure of the old basement volcanic units with the overlying young volcanoes (Muraoka et al., 2005).
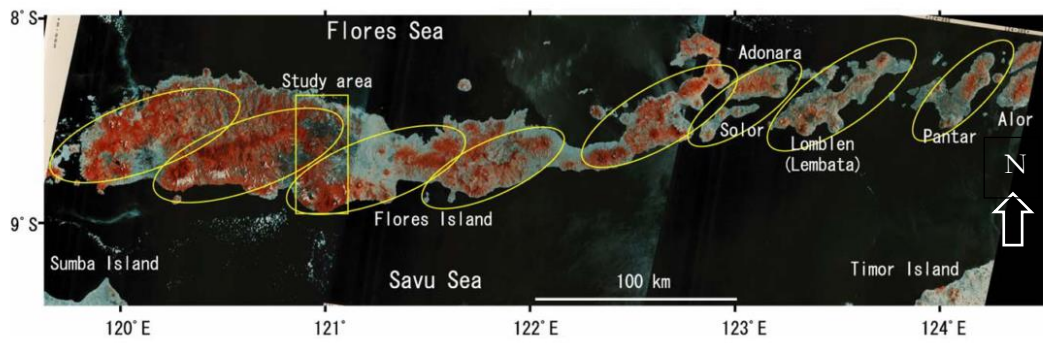
Figure 2.2 Landsat Multispectral Scanner imagery of the inner Lesser Sunda arc. The yellow ellipses show *en échelon* structures with orientation NE-SW that control the anticline and clustered young volcanoes in Flores island. The yellow box shows a study area of the original source of this figure. Source: Muraoka et al. (2005).
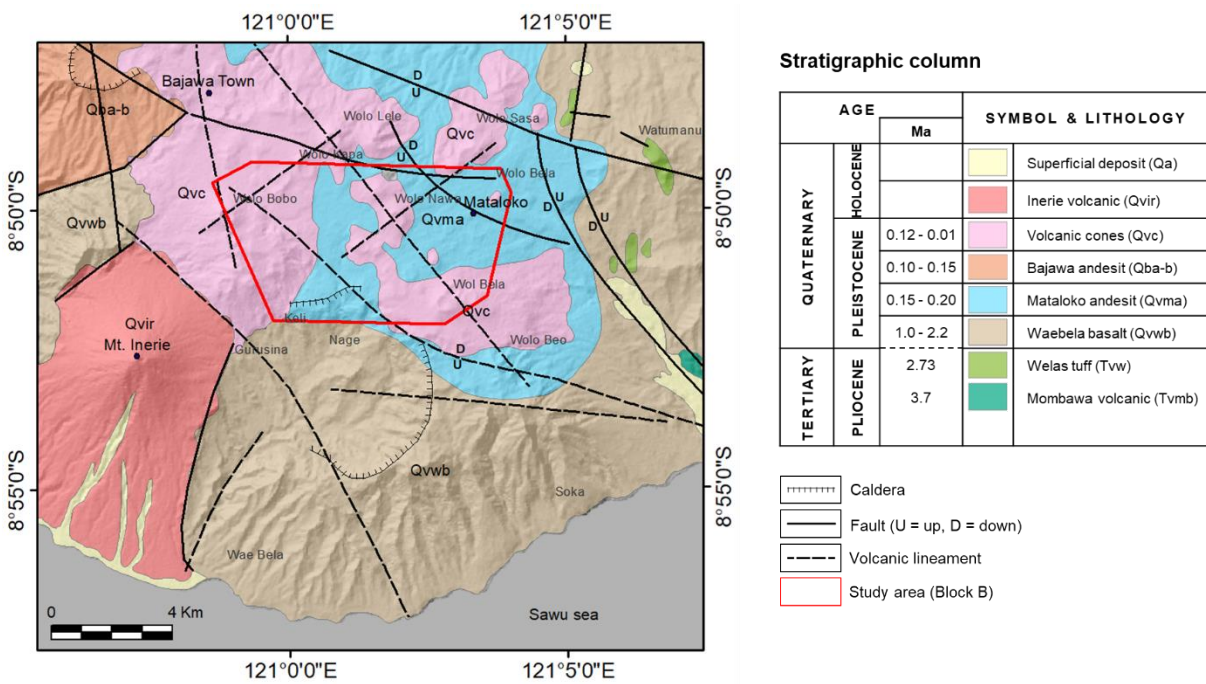
Figure 2.3 Geological map of the Bajawa area draped on top of the hillshaded SRTM imagery. The red polygon shows location of Block B. The caldera structure at the south of study area is the Nage Caldera. Modified from Nasution et al. (2000).

The tectonic event in the Bajawa rift zone was followed by formation of the cinder cone complex that consists of more than 60 cinder cones (Muraoka et al., 2002). These cinder cones surround the study area on the northern and southern side with the possible alignment in N-S and NW-SE directions. The north study area which called the Inielika volcanic complex consisted of 25 breccia cones elongated in N-S direction (see Block A in Fig 2.1). Meanwhile, the southern side is the Bobo and Mataloko complex which comprised of approximately 10 and 16 breccia cones, respectively (see Block B in Fig 2.1). Although these breccia cones are separated away, the similarity of lithology, magmatic affinity, and eruption type suggests that the Bajawa cinder cone complex is a connective dike complex at depth with the same magma chamber (Muraoka et al., 2005). The Bajawa area has two active volcanoes including Inerie volcano in the south and Inielika volcano in the north (Fig 2.1). The magmatic sources of these volcanoes are interpreted as the primary heat sources for the geothermal systems in Bajawa area.

2.1.2. Geology of the study area

According to Muraoka et al. (2002), the geology of Bajawa area is comprised of Tertiary and Quaternary volcanic rock (Fig 2.3). The oldest units are the Maumbawa basalt (Tvmb) and Welas tuff (Tvw) with ages of 3.37 and 2.73 Ma, respectively. The Maumbawa basalt consists of massive lava flows, meanwhile the Welas tuff is characterized by the voluminous ash-flow tuff containing altered greenish pumice and poorly sorted lithics. The source of this formation was presumably from the Welas caldera (~15 km to the north-east of Bajawa town) that erupted during the Pliocene volcanism. This unit was unconformably overlain by the Quaternary volcanic deposits including the Waebela basalt (Qvwb) which characterized by basaltic rocks with columnar join, massive lava flow, and pillow lava structure. The age of this unit is 1 – 2.2 Ma based on K-Ar dating.

The Mataloko andesite (Qvma) and the Bajawa Andesite (Qba-b) consisted of andesitic lavas and pyroclastic rocks. Based on K-Ar dating the ages of some rock samples of these units are between 0.1 – 0.2 Ma. The younger Quaternary volcanic cones (Qvc) unit are exposed at the surface as the monogenetic cones such as Wolo Bobo, Wolo Nawa, and Wolo Kapa. This unit is characterized by andesitic-basaltic composition with age younger than 0.01 Ma. The most recent volcanic deposit consists of the Inerie volcano (Qvir) and superficial deposit (Qa) (Nasution et al., 2000).

2.1.3. The geothermal system of the study area

The geothermal system in Bajawa area, particularly Mataloko Geothermal Field (MGF) is known as a steam-heated type or vapor-dominated system. Based on the interpretation of the resistivity and gravity data, previous studies associated the MGF with a normal fault system oriented in NW-SE direction which called the Wae Luja fault (Munandar et al., 2002; Tagomori et al., 2002). From the geochemical analysis of soil sample, the area along Wae Luja fault indicates a high anomaly Hg and CO_2 that suggest the upraising of hydrothermal fluids from a high-temperature reservoir (~283°C) to the surface throughout this fault. Additionally, the water chemistry of some hot spring sample showed a high sulfate content (SO_4) which indicated contamination of H_2S gas near the surface. Therefore, the Wae Luja fault is considered as an up-flow zone of the MGF. The alteration in MGF consists of alunite zone, kaolinite zone, and montmorillonite zone (Nanlohy et al., 2001).

A geophysical survey in 1997-1999 revealed that there is a shallow heat source which is presumed to be associated with a magmatic body of monogenetic breccia cones near MGF (Muraoka et al., 2005). The magneto-telluric survey discovered a very low-resistivity (1-2 Ωm) zone in depth 400-600 m which indicated an alteration cap rock. Meanwhile, the high resistivity zone (>100 Ωm) was found deeper than 900 m (Uchida et al., 2002). From the self-potential analysis, the recharge area with high permeability surface is concentrated in the high elevation topography near the top of monogenetic volcanoes (Dwipa et al., 2001).

Six geothermal exploration wells have been drilled between 2000 until 2006 in MGF with the main target was reservoir layer in depth of 1000 meters below the surface. Two of them (well MT-1 and MT-2) were stopped at a depth of 207 meters and 168 meters due to blew out. Meanwhile, four others (well MT-3, MT-4, MT-5, and MT-6) only reached the cap rock layer in depth between 160 – 760 meters (PT PLN Geothermal, 2010). The steams from the existing wells are used to produce electricity using a small-scale geothermal power plant with the production capacity of 2.5 MW. In 2020, the operator of MGF (PT PLN – an Indonesian state-owned electricity company) is planned to drill some production wells and develops a large-scale geothermal power plant with the production capacity of 22.5 MW (Richter, 2018b).

2.2.   Data description

The main datasets used in this thesis is airborne TIR and LiDAR data which were acquired by GEOCAP project on Mei – June 2018. The LiDAR data and its derivative including point clouds, intensity, Digital Elevation Model (DEM), Digital Surface Model (DSM) have been processed by PT ASI Pudjiastuti Geosurvey (operator hired by GEOCAP). Meanwhile, the airborne TIR data were processed independently as part of this thesis and described in the next chapter. The secondary dataset consisted of Planetscopes multispectral images which were obtained from the European Space Agency (ESA) third party mission. The detail specification of the dataset is given in Table 2.1.

Table 2.1. Detail specification of the data sets used in this thesis.

Data Type	Sensor	Specification		Acquisition date	File format
Airborne TIR	FLIR x6570sc	Wavelength range	: 7.7–9.3 µm	25 May – 5 June 2018	RAW: .ptw Calibrated: Float 32-byte
Airborne LiDAR (*)	Leica ALS70	Derivatives GSD Accuracy	: Point clouds, DSM, DTM : 0.5 m : 0.1 m	25 May – 5 June 2018	.Ply and .LAS .tif
Geolocation and orientation	GNSS & IMU Leica	Frequency	: 100 Hz	25 May – 5 June 2018	.txt
Multispectral image	Planetscopes ortho tile	Spectral GSD Level	: 4 bands (VNIR) : 3.125 m : 3A (at sensor radiance)	28 August 2017	.tif .xml (metadata)
Surface temperature (Fieldwork)	Fluke IR thermometer	Sensitivity Field of View (FOV)	: -40°C - 800°C : 2 – 5 cm	10 – 24 September 2018	Table

(*) processed by an operator

2.3.   Software used

The software used in this thesis is listed below:

1. ArcGIS   :   This software was mainly used for database management and processing of the airborne, satellite, and fieldwork data. It also used for the maps production.
2. ENVI + IDL   :   This software was used for the Dynamic Threshold Filtering (DTF) and the statistical analysis of airborne data.
3. ERDAS Imagine   :   It was used to produce the albedo images from the Planetscopes multispectral imagery using *ATCOR 3 workflow* tool.
4. Global Mapper   :   The automatic re-classification of LiDAR point clouds was carried out using this software.
5. Leapfrog   :   This software was used for presenting a multilayer of surface and subsurface data. A 14 days trial license was used during this research.
6. PCI Geomatica   :   This software provides an automatic lineament extraction module for LiDAR DEM. A 30 days trial version was used.
7. PiX4D mapper   :   This software was used to produce the airborne TIR orthoimage using Image Based Modeling (IBM) workflow.
8. RockWorks   :   It was used to create the rose diagrams and the lineament density maps. A trial version was used during this research.
9. RStudio   :   In this software, the script for Decision Tree Classification (DTC) was written and performed.

3. AIRBORNE TIR ORTHOIMAGE GENERATION

3.1. Introduction

This chapter describes the production of airborne TIR orthoimages using an automated Image-Based Modeling (IBM) workflow. This chapter consisted of three main part. First, it describes the acquisition process of airborne TIR data. In the second part, it focuses on designing the IBM workflow for more than 8,000 thermal images. In the last part, it presents the quality assessment and improvement of the orthoimage products. The outputs of this chapter were used in Chapter 4 as a basis for geothermal temperature anomalies detection.

3.1.1. Image-Based Modeling – A basic theory

IBM is a process to extract the 3-D perspective model from the sequence of overlapping images (Szeliski, 2011). Unlike the traditional photogrammetric method that requires manual image orientation, the IBM uses Structure from Motion (SfM) method to reconstruct the 3-D position and orientation of the camera automatically. The SfM identify the matching features in multiple images that taken from a different angle (see Fig 3.1 reprinted from Yilmaz & Karakuş (2016) for illustration). Many algorithms have been designed for feature detection and matching of digital images, but an emerging method is the Scale Invariant Feature Transform (SIFT) algorithm which adaptive to the angle, scale, and contrast variations in multiple images (Westoby et al., 2012).

The corresponding feature between images called tie points enables the initial estimation of camera position and object coordinate. The tie points are refined iteratively through Bundle Block Adjustment (BBA) algorithm that uses a non-linear least-squares minimization to build a 3-D sparse points structure (Westoby et al., 2012). During the early stage of SfM, the sparse points structure is constructed in the image-space coordinate system without an absolute position and scale. Later, to transform the relative orientation into the geographic coordinate system either some Ground Control Points (GCP) or absolute position of the camera is required for the scaling, translating and rotating the 3-D sparse points structure.
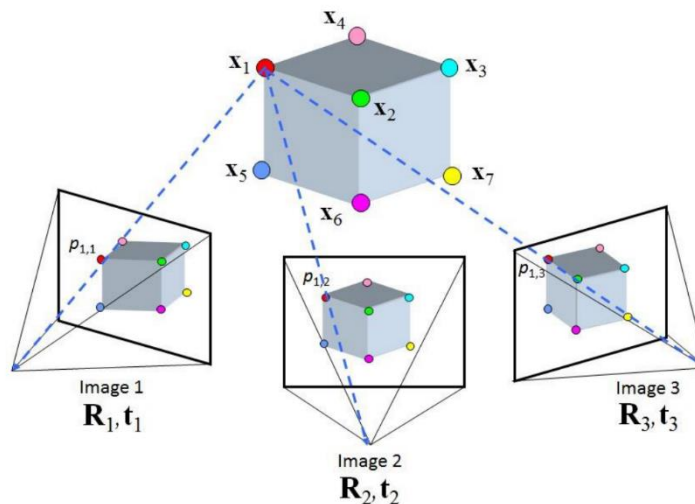
Figure 3.1 An illustration of Structure from Motion (SfM) process. The cube at the top is a reconstructed object from the three images taken from different viewpoints (image 1-3). The dashed blue lines connecting locations of some specific features in multiple images ($P_{1,1}$, $P_{1,2}$, and $P_{1,3}$, ….) with the corresponding features in 3D object (X_1, ….). From these lines the camera position (R_1, t_1, …) is estimated. Source: Yilmaz & Karakuş (2016).

3.2. Methodology

3.2.1. Airborne data acquisition and the instruments setup

The airborne data were acquired on 25 May – 5 June 2018 through the GEOCAP project over the Bajawa area in the East Nusa Tenggara province. The acquisition was operated by PT ASI Pudjiastuti Geosurvey (APG) using a Pilatus Porter PC6 aircraft combining the LiDAR and TIR sensor. These sensors were installed side by side in the aircraft to synchronize their geolocation and orientation that were recorded by Global Navigation Satellite System (GNSS) receiver and the Inertial Measurement Unit (IMU). The TIR camera was mounted on a metal bracket and a shock absorbing platform to fit the camera into the port as well as reduced the vibration from the airplane (Van Veen, 2017). A detail configuration of the LiDAR and FLIR camera systems is illustrated in Fig 3.2.

The airborne data acquisition was carried out in the early morning until a maximum at 10:00 am WITA (Central Indonesia Time). This timeframe was chosen since the night time acquisition was not possible due to a restriction from the local air traffic authority. The weather during image acquisition was reported fine on the first and the last day (26 May and 5 June 2018). The acquisition was carried out at 750 – 1000 meters above the grounds with the forward overlap and side overlap of approximately 80% and 30%, respectively. The distance between the flight line was between 150 – 250 meters.
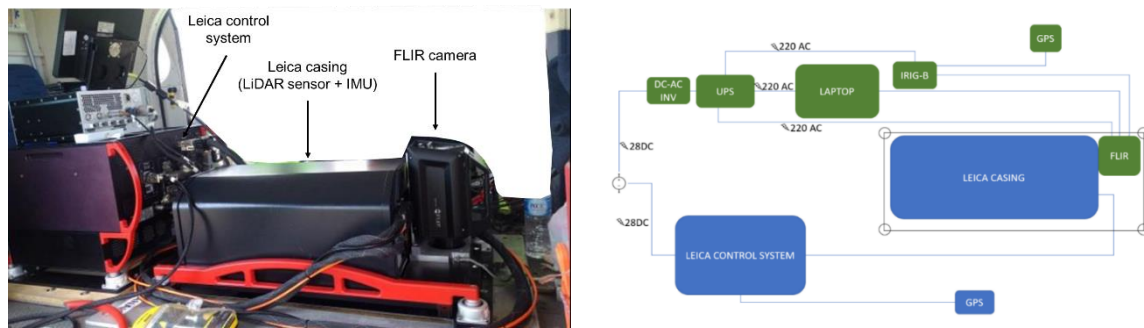
Figure 3.2 The configuration of LiDAR and TIR sensor inside the aircraft (left). The FLIR camera was installed next to the Leica casing containing LiDAR sensor and IMU. A detail schematic illustration of the main and supporting component for LiDAR (in blue) and TIR sensor (in green) (right). Source: PT ASI Pudjiastuti Geosurvey (2018) and Van Veen (2017).

Table 3.1. Super framing mode setup in the ResearchIR with different integration time and temperature sensitivity range. The shortest integration time (Preset2) has higher sensitivity range than Preset 0 and 1 but contain more noise.

Preset	Integration time (µs)	Temperature range (°C)	
		Min	Max
0	500	5	30.6
1	300	5	63.2
2	100	7.1	150

The TIR images were obtained using broadband FLIR x6570sc camera owned by Geoscience Laboratory, University of Twente. This camera is sensitive in the longwave infrared domain between 7.7 – 9.3 µm. The camera was operated at 1 Hz frequency controlled by ResearchIR software. From this software, the FLIR camera was forest to three different integration times (called preset) with different temperature ranges (see Table 3.1). The longest integration time has the least noise but low saturation temperature. In order to capture hotspots at the surface with a wide temperature range, a shorter integration time was also used although it has higher noise. The TIR images were stored on a laptop. The header of TIR images contain a

time stamp that was derived from the IRIG-B time code generator. This time stamp was used to register the external orientation provided by GPS receiver and IMU to the individual TIR images.

The Leica ALS70 sensor was used for the LiDAR data acquisition with pulse rate in 1 MHz frequency. The laser return signals were stored together with GPS and IMU information in the Leica control system that was powered by the aircraft's power supply with 28 V direct current (DC) (PT ASI Pudjiastuti Geosurvey, 2018). The laser return signals were processed by PT APG into LiDAR derivatives including point clouds data, DEM, and DSM as described in Section 2.2.

3.2.2. Block division and theoretical accuracy

The survey area was divided into two blocks which are labeled as Block A and B (Fig 3.3). These blocks contain 1,946 and 6,722 image files, respectively. To reduce the memory usage during the IBM processing, each block was divided into sub-blocks according to the spatial configuration and flight parameter criteria such as:

a) The images in a sub-block should have at least 80% forward overlap and 30% side overlap;
b) Every image in the edges of sub-block should have a duplicate or an overlapping image with the neighboring sub-block to allow the merging of initial structure (3-D sparse points);

A theoretical accuracy and an expected Ground Sampling Distance (GSD) were calculated using equations 3.1 − 3.3 for each block and sub-blocks to compare the results of IBM workflow with this estimation. This calculation refers to the theoretical accuracy equation used by Förstner (1998) for stereo-pair photogrammetry.

$$GSD = \frac{X * H}{f} \qquad (3.1)$$

$$\sigma z = \frac{H^2 * Spx}{B * f} \qquad (3.2)$$

$$\sigma x = \frac{H^2 * Px * Spx}{f^2 * B} \qquad (3.3)$$

Where σz and σx is the theoretical vertical and horizontal accuracy respectively. H is the relative flying height above the ground that was calculated from an average of the flying altitude of the aircraft subtracted by an average of the LiDAR DSM. B is the distance between strips, f is focal length, x is pixel size. Spx is the expected collimation accuracy which pessimistically maximum two pixels, and Px is the maximum parallax that can be obtained from homologous points in the stereo pair (50% percent from width of the TIR image). The theoretical accuracy estimation of Block A and B is given in Table 3.2.

Table 3.2 The estimation of vertical (σz), horizontal (σx) accuracy and ground sampling distance (GSD) for each block and sub-block project based on equation 3.1 − 3.3 (unit in meter). A typical GSD is 0.45 m, σz and σx are 3.7 − 4.7 m and 0.7 − 0.9 m respectively. Block B and its sub-block have relatively higher GSD and accuracy than Block A.

Sub-block	Flying altitude		Surface elevation		Flightline distance		Flying height	GSD	σz	σx
	Mean	St dev	Mean	St dev	Mean	St dev				
A	2138.56	134.03	1359.99	184.80	168.66	30.02	778.57	0.47	4.31	0.83
B	1988.25	7.97	1308.52	116.42	147.31	11.30	679.73	0.41	3.76	0.72
A1	2168.60	153.33	1421.89	251.82	160.29	31.05	746.71	0.45	4.17	0.80
A2	2111.50	117.64	1367.55	189.04	175.16	24.66	743.95	0.45	3.79	0.73
A3	2114.79	119.99	1322.99	129.64	158.91	51.86	791.80	0.48	4.73	0.91
B1	1983.19	3.56	1308.99	120.11	144.35	8.31	674.20	0.40	3.78	0.73
B2	1992.68	8.11	1308.32	111.72	149.89	12.83	684.36	0.41	3.75	0.72
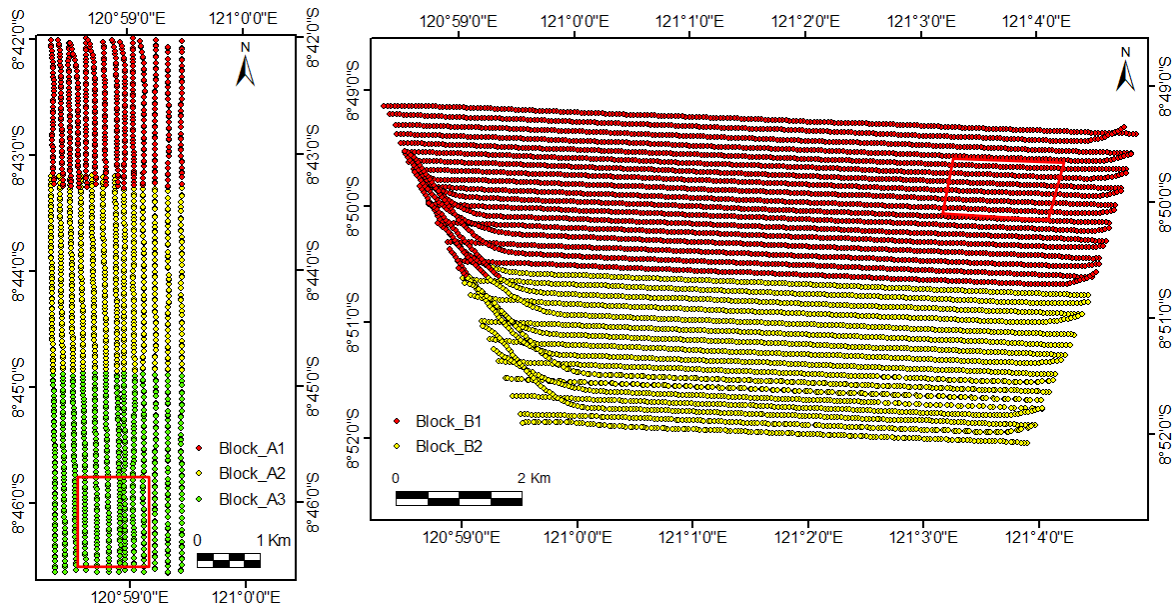
Figure 3.3 The division of Block A (left) and Block B (right) into sub-block projects. The camera position was extracted from GPS data. The edge of each sub-block contains some overlapping images with the neighbouring sub-block. The red squares indicate training locations that were used for internal camera parameter optimization (described in Section 3.3.1).
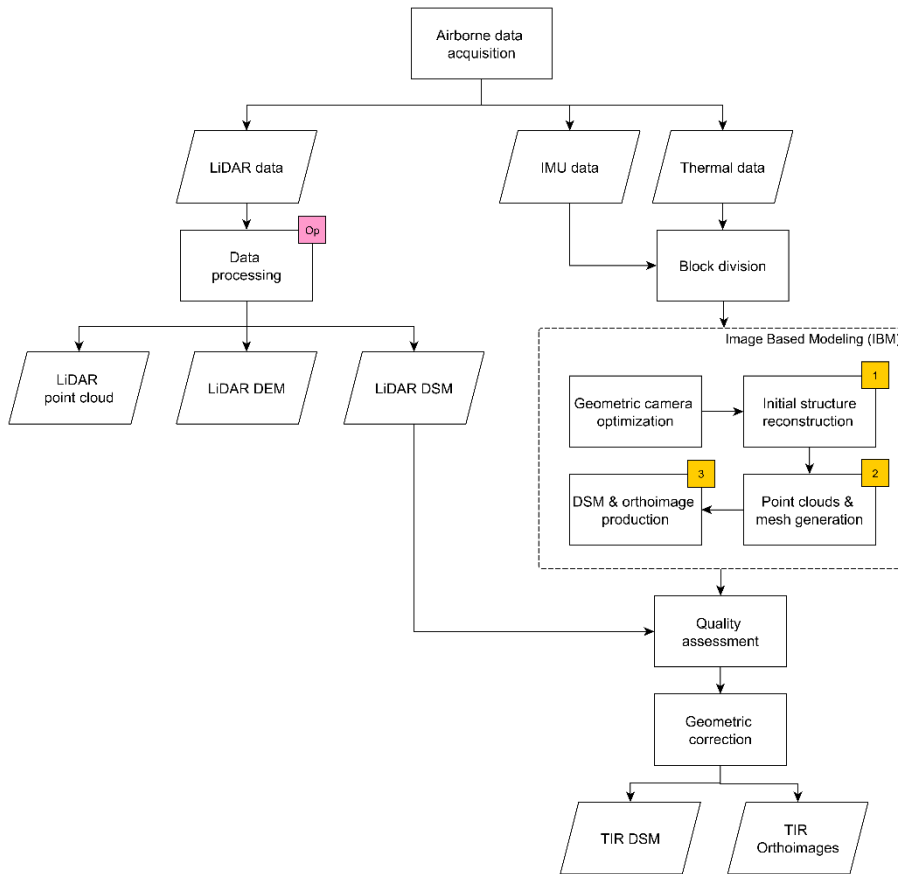
Figure 3.4 Flowchart of Image Based Modeling (IBM) workflow. The light red box indicates the process that was taken by the operator hired by the GEOCAP project. The yellow boxes show sequence of IBM process in Pix4D mapper software.

3.2.3.   Image-Based Modeling workflow

The IBM process was conducted in Pix4D mapper. This software provides an advanced template for thermal image processing which allowed a contrast enhancement using a Dynamic Histogram Stretching (DHS). This DHS improves feature extraction and matching of the overlapping images acquired by thermal camera even if they have low contrast as were acquired at slightly different times. However, this function was not available as a default setting for specific thermal camera type like the FLIR x6570sc. Therefore, to use this DHS function, a simple recognition code needs to be set manually in Pix4D project file. The code was obtained from personal communication with a software engineer of Pix4D mapper (Appendix A).

Pix4D mapper performed the IBM in three steps, including a) initial processing, b) point cloud and mesh densification, and c) orthoimage and DSM generation (see Fig 3.4). The processing time for each step depended on the total number of input images, the speed and memory of a computer. The server computer Intel Xeon 3.10 GHz with memory 49 GB and operating system Windows 10 was used to speed up the IBM process. Before the initialization of the first step, the input images for each sub-block were organized in a separate folder to allow multiple selections at once during the project file import (detailed explanation in Appendix B). The IBM workflow in this chapter use no ground control point (GCP) but camera position from differential GNSS and IMU as a starting point for thermal images orientation.

The IBM was first initiated with the iterative optimization of the geometric camera (interior) parameter from two training area with a small number of overlapping images (ref to Fig 3.3). This optimization was aimed to increase the level of automatic image calibration and feature matching, as well as minimize the geometric error of the 3-D sparse point structure. This optimization is an important step to minimize the error yielded by the interior camera parameter changes during the acquisition that were possibly caused by factors such as low-frequency vibration of the aircraft and a variation in the FLIR camera temperature during the acquisition. This optimization was carried out in three iterations, where the first iteration was aimed to evaluate the default camera parameters given in the specification list of FLIR x6570sc. The second optimization was aimed to re-evaluate the optimized camera parameters given by the first iteration, and the third iteration was conducted to test the stability of the optimized parameters given by the second iteration (further explanation in Section 3.3.1).

The internal camera parameters of the third iteration were applied to each sub-block by re-initializing the first step of IBM. This process was yielded 3-D sparse point clouds for each sub-block project. Then, the initial structure (3-D sparse points) of all sub-blocks were merged to build a rigid structure of a block project using *merged project* tool in Pix4D mapper. This tool performed reorientation using tie-points and BBA to align the different 3-D sparse point structures from the sub-blocks. Then, the merged block was re-optimized automatically to make sure that the overlapping features fitted together. The IBM was continued by the second step which is dense point cloud extraction, then the third step which is the orthoimage and DSM generation. The last two processes were straightforward, where no user interference was required except for the inspection of error in the dense point clouds.

3.2.4.   Quality assessment and geo-correction

A direct comparison with LiDAR data was undertaken to assess the geometric quality of TIR orthoimage and DSM products both for the horizontal and vertical direction. The reason for this comparison because there was no GCP available for the TIR images at the study area. Hence, a comparison with the LiDAR DSM which has an accuracy of 0.1 meters is a reasonable method for assessing the quality of airborne TIR orthoimages. For the horizontal accuracy assessment, the horizontal shift vector (HSV) was analyzed by manually digitizing points in the TIR orthoimages with the corresponding points in the low-angle hillshaded LiDAR DSM. The points were mainly digitized in the artificial objects that have a distinct

feature in both images such as a road intersection, a corner of the building, and an edge of the agriculture land. Besides, some points on distinct morphological features were also digitized. In the following step, the extracted points were converted into the line vector with the length indicating the magnitude of the horizontal shift, and their azimuth indicating the direction of shift.

The geometric error (horizontal shift) of the airborne TIR orthoimages was corrected using a *rubber sheeting* function in ArcMap. This technique adjusts the geometric of raster by stretching the linking points of a source image to the corresponding point's position in the underlying image as a reference, in this case the LiDAR DSM. Rubber sheeting works similarly to image transformation, where the displacement links are used to determine the direction and position of a feature. However, the moving distance of a feature depends on its proximity and the length of a link (ESRI, 2016b). In practice, the HSV(s) containing an initial coordinate of features in the airborne TIR orthoimages and the target coordinate in the LiDAR DSM were used as the links in *rubber sheeting* transformation.

The DSM of Difference (DoD), a terminology representing the vertical shift, was produced by subtracting the elevation of TIR DSM with LiDAR DSM. A positive and negative value indicates the shift direction, where the positive DOD means the shift direction of the TIR DSM is upward, meanwhile the negative indicated the downward shift. The scalar value of the DoD indicates the magnitude of the vertical shift. In this research, this DoD was used as a basis to assess the performance of IBM workflow for the airborne TIR data. However, no correction was implemented to improve the vertical shift of the TIR DSM since it is less critical for 2-D geothermal anomaly mapping purpose.

3.3. Results

3.3.1. Interior camera optimization

Table 3.3 and Table 3.4 show the results of interior camera parameter optimization for Block A and Block B, respectively. The optimized value on this table was acquired by iteratively processed the first step of IBM both for the training area of Block A and Block B (ref Fig 3.3). These tables show eight components of the optimized camera parameter including focal length, principle point X and Y, and the geometric distortion parameters of the lens. These parameters were evaluated based on two indicators including the number of calibrated images (%) and the total number of matching features per image.

According to Table 3.3, the first iteration which used a default camera setting (without geometric lens distortion) had yielded a success rate of 92% calibrated images and 6,374 matching feature per image. These number rose in the second iteration, where the calibrated images increased significantly to 97% and the matching features slightly increased by 13 points. The third iteration showed a surprising result where 100% of the thermal images were calibrated, and the matching features increased 15 points. From this result, it shows that the optimized interior camera parameter yielded a significant improvement to all indicators of the initial structure (3-D sparse points) reconstruction for Block A.

The same pattern is also shown in Table 3.4 for Block B, where the optimized interior camera parameters produced a better quality in all indicators. The first iteration yielded 95% of the calibrated images and 6,083 matching feature per images. In the second iteration, these number increased significantly to 100% and 6,124 points for calibrated images and the number of matching features per image, respectively. However, in the third iteration, the number of calibrated images was stabled in level 100% but the number of matching features decreased to 6,085. This trend indicates that the over iterations did not guarantee the improvement of the indicators of initial structure (3-D sparse points) quality.

Table 3.3. Iterative optimization of the interior parameter of the FLIR camera for the training area of Block A. Total input of this training area is 186 images. The R1-R3 and T1-T2 are the radial and tangential distortion parameter of the lens of FLIR camera, respectively. The sigma indicates the uncertainty of the optimization process.

Iteration	1st		2nd		3rd	
Parameters	Initial	Sigma	Optimized	Sigma	Optimized	Sigma
Focal length (mm)	25	0.050	25.320	0.053	24.834	0.053
Principle point x (mm)	4.8	0.007	4.565	0.008	4.541	0.008
Principle point y (mm)	3.84	0.009	3.908	0.010	3.921	0.009
R1	0	0.005	-0.487	0.005	-0.473	0.005
R2	0	0.165	1.233	0.154	1.031	0.174
R3	0	1.791	-15.357	1.611	-12.632	1.893
T1	0	0	0.002	0	0.002	0
T2	0	0	0	0	0	0
Indicators						
Calibrated image	92%		97%		100%	
Matching per image	6374.46		6387.59		6392.5	

Table 3.4. Iterative optimization of the interior parameter of the FLIR camera for the training area of Block B. Total input of this training area is 190 images. The R1-R3 and T1-T2 are the radial and tangential distortion parameter of the lens of FLIR camera, respectively. The sigma indicates the uncertainty of the optimization process.

Iteration	1st		2nd		3rd	
Parameters	Initial	Sigma	Optimized	Sigma	Optimized	Sigma
Focal length (mm)	25	0.145	25.283	0.146	25.203	0.147
Principle point x (mm)	4.8	0.006	4.557	0.006	4.565	0.006
Principle point y (mm)	3.84	0.019	4.079	0.019	4.094	0.019
R1	0	0.007	-0.476	0.007	-0.477	0.007
R2	0	0.145	0.729	0.148	0.945	0.148
R3	0	1.584	-10.278	1.642	-13.153	1.636
T1	0	0	-0.001	0	-0.001	0
T2	0	0	0	0	0	0
Indicators						
Calibrated image	95 %		100%		100%	
Matching per image	6083.36		6124.4		6085.73	

3.3.2. External quality assessment

The thermal orthoimage products from the IBM workflow are presented in Fig 3.5. The output GSD for Block A and B are 50.12 cm and 40.35 cm, respectively. Block B has a higher resolution than its theoretical GSD estimation of 41 cm (ref Table 3.2). Meanwhile, the orthoimage of Block A has slightly lower resolution than its theoretical GSD of 47 cm. This difference is relatively low considered the variability of the flying height of the aircraft and focal length of the camera as the most determinant parameters of the GSD outcome. This GSD is expected to give sufficient information for the detection of geothermal temperature anomalies with the size of sub-meter.

HSV was manually extracted by comparing the airborne TIR orthoimages with the LiDAR DSM as a reference (Fig 3.5). In total, 180 and 245 HSVs have been manually extracted for Block A and Block B, respectively. This comparison revealed that Block A has an average HSV for X and Y direction of 1.4 m and 2.4 m, and the standard deviation of 4.3 m and 5.6 m, respectively. Most HSV of Block A has a magnitude between 0 – 5 meters and 5 – 10 meters. Some HSV higher than 10 meters is distributed mainly at the edges of Block A. These high HSV produced a relatively high overall RMSE of 7.6 m, which is nine times higher than the expected horizontal accuracy of Block A (Table 3.2). For Block B, the average HSV for X and Y direction is 0.6 m and 1.3 m, and the standard deviation of 1.2 m and 3.4 m,

respectively. The total RMSE for Block B is 3.9 m, which is five times higher than their expected theoretical accuracy. However, almost 90% HSV of Block B has a magnitude of fewer than 5 meters. HSV higher than 5 meters is mainly distributed at the south and the west of Block B, where they exceed 10 m. From the rose diagrams in Fig 3.7, the HSV of Block A and Block B is systematic with the main error direction is towards north and south, respectively.

DoD was created by subtracting the airborne TIR DSM with the LiDAR DSM as a reference to inspect the vertical shift (see Fig 3.6). The results in Fig 3.6 and Fig 3.8 reveal that 67% of Block A and 66% of Block B have overlapping DoD value in the range between -10.0 – 10.0 meters, with approximately 37% of DoD are within in the range of their theoretical accuracy. Overall, Block A and Block B show a relatively low vertical shift where the mean DoD for Block A is -4.5 m and for Block B is 1.2 m. The standard deviation of DoD is 20 m and 13 m for Block A and Block B, respectively.
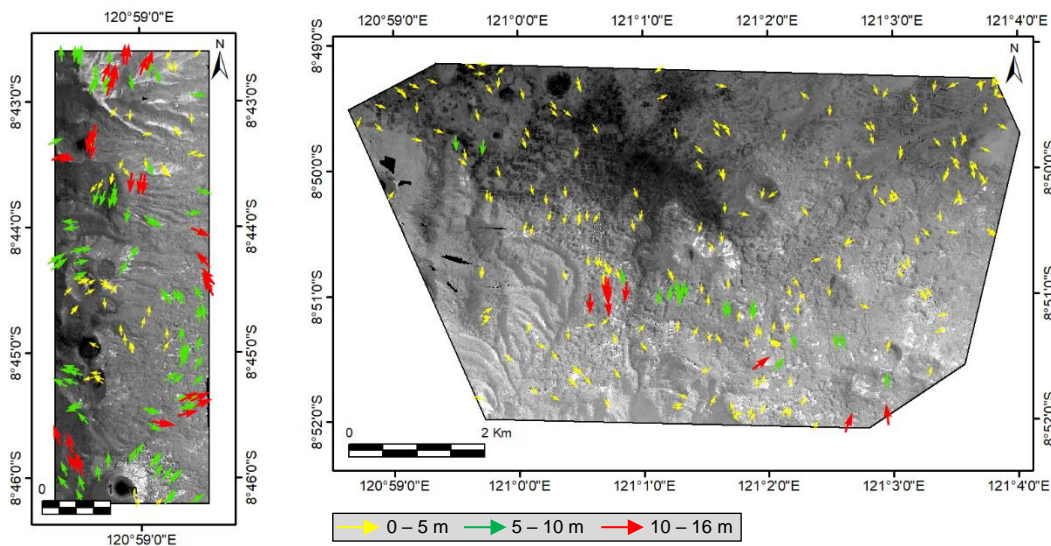
Figure 3.5 Horizontal Shift Vector (HSV) of Block A (left) and Block B (right) draped on top of the TIR orthoimages that was produced from IBM workflow. The arrows direction indicates co-registration error direction of the TIR orthoimages from a reference (the LiDAR DSM). The length of the vectors is exaggerated in this figure.
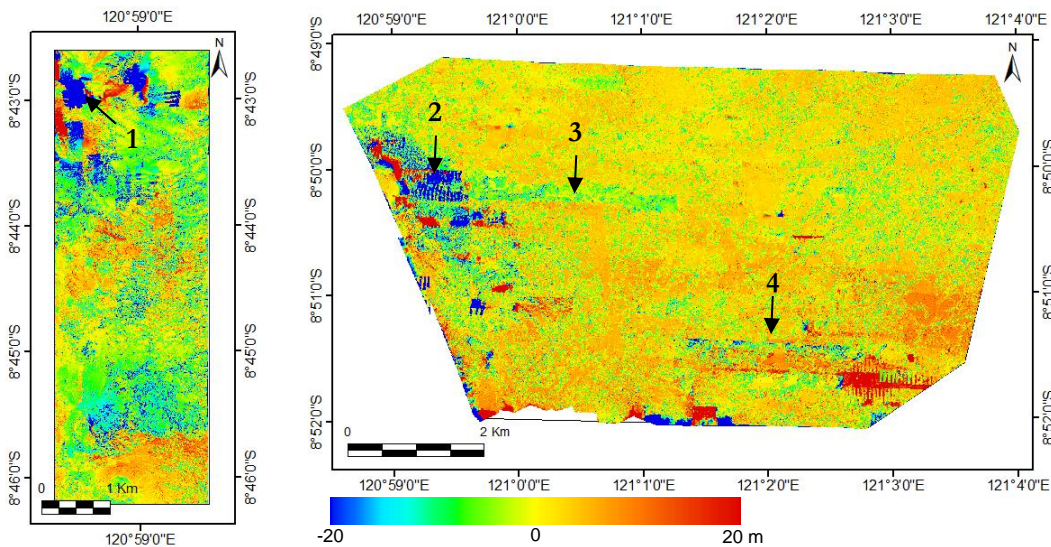
Figure 3.6 DSM of difference (DoD) between FLIR DSM and LiDAR DSM indicates the vertical error of Block A (left) and Block B (right). The positive DoD indicates that the FLIR DSM has higher elevation than the LiDAR DSM. The highest vertical error for Block A is given in the NW corner (location 1), meanwhile for Block B given in the west (location 2) and southeast side. Some unexpected errors are observed at location 3 and 4 in Block B (discussed in Chapter 7).

Fig 3.9 shows a significant variation of DoD in respect to the landcover type including ground, low vegetation, high vegetation, and building. The landcover image was produced from LiDAR point clouds classification (described in Chapter 4). In Block B, all land cover types have a positive mean DoD. Meanwhile, the mean DoD of Block A for the grounds, the low and high vegetations are negative. Moreover, only the building class has a positive value. In particular, the buildings have a similar statistic pattern for Block A and Block B, where the mean DoD value is the highest, and the standard deviation is the lowest among others. Additionally, the high-vegetations show an interesting pattern where the mean DoD for Block A and Block B is different, but the standard deviation DoD almost shows a similar value and the highest among the other classes.
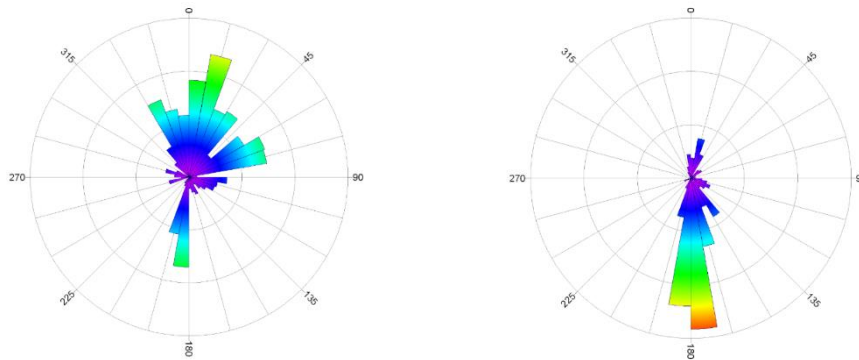
Figure 3.7 Rose diagram showing frequency of the horizontal shift vector (HSV) directions for Block A (left) and Block B (right). The HSV of Block A has more directional variation with the dominant direction is north. Meanwhile the main HSV directions of Block B is toward south.
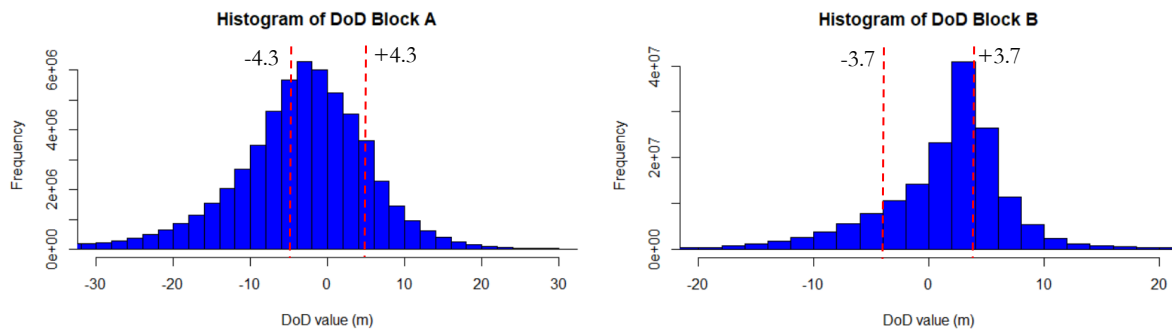
Figure 3.8 Histogram of DoD between the FLIR DSM and the LiDAR DSM for Block A (Left) and Block B (right). 37% DoD of Block A and Block B are within the range of their theoretical vertical accuracy (dashed line).

	Ground	Low vegetation	High vegetation	Building
Block A	-3.221098	-4.096501	-3.377313	5.618708
Block B	1.67154	0.772443	0.626663	4.055939

	Ground	Low vegetation	High vegetation	Building
Block A	7.94564	8.011295	8.524582	3.777239
Block B	4.798928	6.132263	8.44885	1.572744
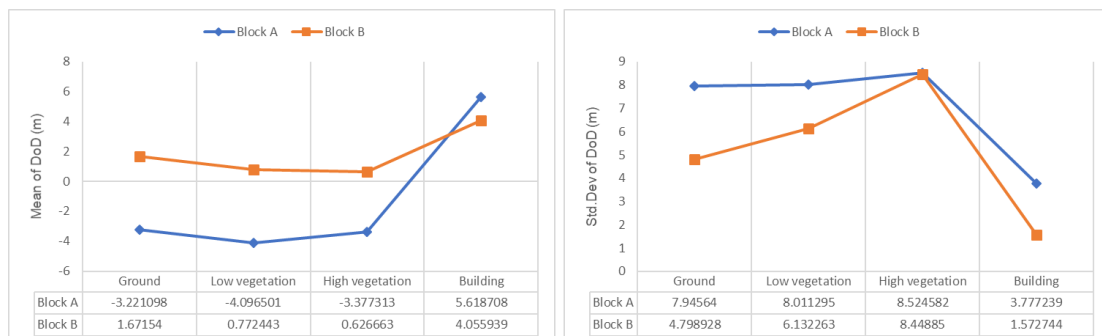
Figure 3.9 The mean (left) and standard deviation (right) DoD for different land cover type. Building class has a high positive mean and low standard deviation for Block A and B. The other classes have relatively high standard deviation for the two blocks except for the ground class for Block B.

4. GEOTHERMAL TEMPERATURE ANOMALIES DETECTION USING AIRBORNE TIR IMAGES

4.1. Introduction

This chapter describes a new approach for geothermal temperature anomalies detection using airborne TIR images and its combination with LiDAR data and multispectral imagery. The key development of this chapter is an implementation of machine learning technique for the two main part of the tasks, which are 1) threshold determination of temperature anomalies and 2) discrimination of the true and false anomalies. The former was introduced by the Dynamic Threshold Filtering (DTF) technique according to the statistical characteristic of temperature as a basis to separate temperature anomalies from background temperature. The second task was developed using a Decision Tree Classification (DTC) model integrating several variables such as ground albedo, hillshade, and land cover images to filter the false positives and emphasise the geothermal temperature anomalies.

4.1.1. Differences to existing approaches

Previous works had been mainly focused on the demonstration of the ability of airborne data for geothermal anomalies detection and monitoring (Haselwimmer et al., 2013; Hodder, 1970). The technique like visual analysis of contrast stretched TIR images, and band threshold was mainly used as common methods for discriminating geothermal anomalies from background temperature. Although they are found to be a simple way, these approaches have a high dependency on the experience of the user to recognize the geothermal feature. Besides, a technique like a band threshold often worked only for the local scale and very specific to the geothermal site. Moreover, it is effective only for night time and predawn acquisition when the solar illumination does not significantly cause surface temperature variation.

The issue of false positives due to the solar heating effect has been investigated for geothermal temperature anomalies detection using satellite imageries. Some study using ASTER TIR data incorporated the external variables such as ground albedo, thermal inertia, emissivity, and topographic slope/aspect as factors that determine temperature variation of the earth surfaces. These factors were modeled by Coolbaugh et al. (2007) using the simplified heat energy model describing net surface radiation flux. The surface heating due to the radiative transfer of the Sun's light is determined by the integrated factor of albedo and incident angle between the Sun's rays and the surface normal (see Eq 4.1).

$$Q = So \, (1 - A) \, M \, (\theta) \, cos \, \theta' \qquad\qquad (4.1)$$

Where Q is the net flux at the surface, So is a constant for solar radiation, A is ground albedo, $M(\theta)$ is atmospheric transmittance as a function of zenith angle θ, and $cos \, \theta'$ is the cosine of the angle between the surface normal and the Sun's rays (see Fig 4.1 retrieved from ITACA, (n.d.) for illustration). According to this equation, the $cos \, \theta'$ corresponds to the solar incident angle of a topographic surface which has a positive correlation with the net surface flux at the surface, which also means if the $cos \, \theta'$ is high it would directly relate to the increment of surface temperature. On the other hand, the albedo is negatively correlated with the net flux at the surface which means if the albedo is low (dark material) the surface temperature will be higher.
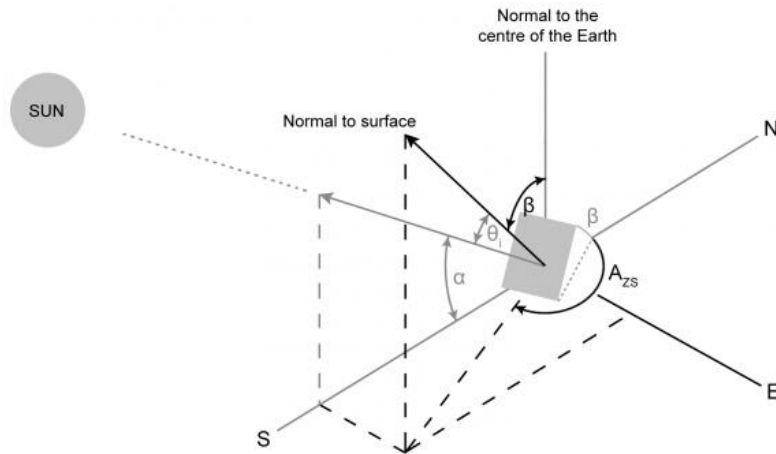
Figure 4.1 Schematic illustration of the Sun's rays and surface angle. β is the angle of inclination of the surface from the horizontal. α is the altitude angle of the Sun, and θ is the angle of incident. Source: ITACA (n.d.), retrieved at 2018-12-26.

The solar heating effect on a geothermal field is simpler to model on spaceborne rather than airborne TIR images because satellite data capture a large area on a single frame at a single time. Meanwhile, the airborne TIR system requires a longer time to acquire images for a large area. Consequently, a multi-incident angle during airborne TIR data acquisition cannot be avoided, especially for the daytime acquisition. This issue can emerge a non-linear increment of surface temperature over an area. The sun illumination has a different effect on the location that is acquired at slightly different times. For example, the late morning acquisition contains higher surface temperatures than the early morning acquisition. Hence, this high-temperature surface (false anomaly) potentially mixes with geothermal manifestations with relatively low temperature on a daytime airborne TIR image.

In this chapter, two different approaches were designed to overcome the earlier problems given by the complexity of physical variables during the daytime acquisition of the airborne TIR images. First, unlike the previous studies that commonly rely on either visual analysis or global band threshold, here we used a DTF method that works based on the dynamic statistical threshold to separate temperature anomalies from background temperatures. This approach is independent of a priori knowledge of the geothermal system and potentially minimized bias due to the user's subjectivity and inaccurate use of the global threshold. Secondly, the discrimination of the true and false anomalies was developed differently from the existing model. While the earlier studies performed a forward modeling of the simplified heat budget concept, this chapter demonstrate for the first time a Decision Tree Classification (DTC) method to filter the false anomalies and predict the distribution of true anomalies by combining several physical variables including ground albedo, topographic relief, land cover types, and DTF image.

The methodology presented in this chapter has the potential to 1) handles both the linear and non-linear relationship between variables and the predicted anomalies, 2) avoids overfitting by pruning the parameters of the model, and 3) provides the probability of the classification results of the true anomalies. Here, the model was built on a known geothermal area that has been surveyed in September 2018, and it was tested on the entire scene to identify unknown geothermal manifestation.

4.2. Methodology

4.2.1. Fieldwork measurement

In order to understand the characteristic of the geothermal and non-geothermal anomalies, the fieldwork has been carried out between 10 – 24 September 2018. This fieldwork was focused on ground truthing

hotspots that show high temperature on the airborne TIR orthoimages. These locations were measured using a handheld/non-contact Fluke IR thermometer. Several measurements using a mercury glass thermometer was recorded to calibrate the measurement from Fluke IR thermometer (detailed in Appendix D). The measurement was conducted at around 7:30 until 14:30 WITA (Central Indonesia Time). Each hotspot was in the field identified as geothermal or non-geothermal anomalies based on Fluke temperature measurement and their physical expression (described further in Section 4.3.1).

The sample locations of geothermal and non-geothermal hotspots were organized in a geodatabase and digitized in ArcMap as polygon feature. The boundary of sample locations was interpreted from the airborne TIR orthoimages. The polygons then were indexed using the identification code (Code ID). Then, the indexed polygons were exported as region of interest (ROI) features in ENVI IDL to obtain the statistics of each hotspot in the airborne TIR orthoimage including the minimum, maximum, mean, and the standard deviation. The maximum temperature of the hotspots measured in the airborne TIR orthoimages was compared to the field-based temperature measurement.

4.2.2. DTC input variable creation

To discriminate the geothermal and non-geothermal (true and false) anomalies, several variables including surface albedo, hillshade, land cover, and DTF image were produced and analyzed as a fundamental input in decision tree classification (DTC). The following sub-sections are designated to describe the production of input variables for DTC modeling.

4.2.2.1. Dynamic threshold filtering

In this chapter, we used the modified version of the Interactive Data Language (IDL) script from Kuenzer et al. (2008) and Zhang (2004) to separate the temperature anomalies in the airborne TIR orthoimages from the background temperatures. This DTF algorithm was originally designed for coal fire detection using satellite TIR imagery by identifying pixels that have a higher temperature than the surroundings. Here, the aim of this process was to transform the airborne TIR orthoimages into a floating raster containing only the anomalous pixels (higher temperature than the local surrounding). And to convert the absolute temperature value into a number describing the relative difference between the anomalies with the other pixels in term of their probability as the outstanding anomalies.

The DTF works through a moving window which simultaneously computed a histogram statistic of subset window. The fundamental principle of this method was built on the assumption that within a subset window there would be two groups of histograms, first is a temperature cluster that belongs to the anomalies and the second cluster that representing the background temperatures. The DTF algorithm worked in several steps (Fig 4.2). First, the size of the kernel window was selected considering the GSD of the input image and the spatial extent of the known geothermal manifestation (in this case we used 401 x 401 pixels). Secondly, the threshold was set based on the statistic and the histogram of the kernel window containing temperature information of the pixels. The threshold was set as the first minimum histogram after the mean plus standard deviation. Then, the pixels on the kernel window with the temperature higher than the threshold were tagged.

This kernel window moved with 20 pixels steps in the horizontal direction and then recalculated the threshold using the same principle with the second step. This stepping was applied to reduce the processing time but still let the kernel window investigated every pixel several times (the original algorithm does not use stepping). In the last step, the window was continuously moving until reaching the last row and column of the airborne TIR orthoimages. While it was moving, the number of tags was accumulated for each pixel and then converted to a percentage. The output image is a floating raster with the value

between $0 – 1$ where the high values are the pixels that are, as compared to their surroundings, most likely a thermal anomaly (of geothermal origin or not).
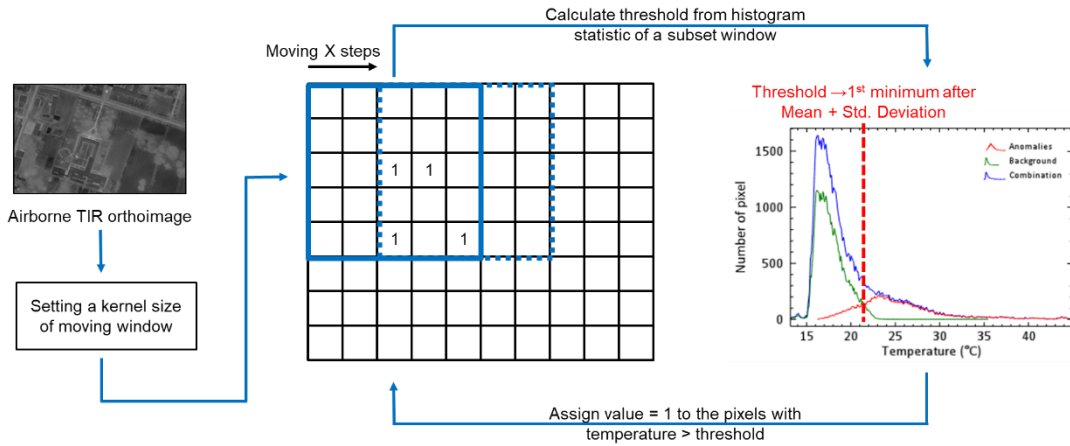
Figure 4.2 Schematic workflow of Dynamic Threshold Filter (DTF) algorithm. The histogram shows an example of kernel window statistic which contained anomalies (highlighted in red) and the background pixels (in green). The blue histogram indicates a combination of backgrounds and anomalies pixels.

4.2.2.2. Surface albedo and hillshade

The albedo image was produced using the ATCOR workflow in ERDAS Imagine. The image derived as an added value product of *ATCOR 3* that designated for atmospheric correction of rugged terrain. The input file to generate albedo consisted of the Planetscopes image with GSD of 3.125 m and the resampled LiDAR DEM (3.125 m). The parameters in Table 4.1 were applied for the albedo image production. The main output from *ATCOR 3* was a haze-reduced reflectance image. Meanwhile, the added value product consisted of six bands, where the albedo corresponded to the third band. The albedo image then was resampled to 0.51 m using the nearest neighborhood interpolation.

Table 4.1. The parameters of albedo image creation using *ATCOR3* workflow in ERDAS imagine software. The value of the parameter was obtained from metadata of the Planetscopes image.

Solar zenith	48.3°	Water vapor category	Tropical
Solar azimuth	62.4°	Aerosol-type	Automatic
Sensor zenith	2.3°	Reflectance scale factor	100
Sensor azimuth	11.3°		

The shaded relief topography that corresponds to the incident angle parameter was derived from LiDAR DSM using a *hillshade* tool in ArcMap. This tool worked by determining illumination values for each cell in a DSM to obtain the hypothetical illumination of the surface. The basic algorithm of *hillshade* is given in Eq 4.2. The author suggests referring to ESRI (2016a) for a detailed explanation of this algorithm. The outcome of the hillshade processing is a shaded relief (hillshade) image with the value between $0 – 1$.

$$Hillshade = ((\cos(Zenith\_rad) * \cos(Slope\_rad)) + (\sin(Zenith\_rad) \\ * \sin(Slope\_rad) * \cos(Azimuth\_rad - Aspect\_rad))) \qquad (4.2)$$

To accommodate the multi-angle of the Sun's azimuth and elevation during the airborne data acquisition, the LiDAR DSM was clipped into several pieces according to the GPS time and trajectory of the aircraft. Firstly, the aircraft trajectory was plotted in ArcMap and then was grouped into 15 minutes interval according to the GPS time which previously had been converted to local time. Secondly, several polygons were created to delineate the flight trajectory within this time interval (see Fig 4.3). After that, the LiDAR

DSM was clipped using these polygons. Lastly, a *hillshade* analysis was applied to each piece of clipped LiDAR DSM using the information of sun azimuth and elevation for the Bajawa area retrieved from Hoffmann, (2018) (see Table 4.2). The results of multi-hillshaded LiDAR DSM are presented in Fig 4.4.

Table 4.2. Sun position for Bajawa area, East Nusa Tenggara Province. Source: Hoffmann (2018).

Time	Date: 2018-05-27		Time	Date: 2018-06-05	
WITA	**Azimuth (°)**	**Elevation (°)**	**WITA**	**Azimuth (°)**	**Elevation (°)**
5:45	69.39	0.52	**5:45**	68.11	0.85
6:00	68.76	0.89	**6:00**	67.55	1.38
6:15	68.18	2.12	**6:15**	66.99	1.64
6:30	67.52	5.41	**6:30**	66.34	4.87
6:45	66.77	8.77	**6:45**	65.59	8.20
7:00	65.92	12.14	**7:00**	64.75	11.53
7:15	64.97	15.50	**7:15**	63.8	14.85
7:30	63.9	18.83	**7:30**	62.73	18.15
7:45	62.7	22.13	**7:45**	61.53	21.42
8:00	61.36	25.40	**8:00**	60.19	24.65
8:15	59.86	28.62	**8:15**	58.69	27.83
8:30	58.18	31.79	**8:30**	57.00	30.97
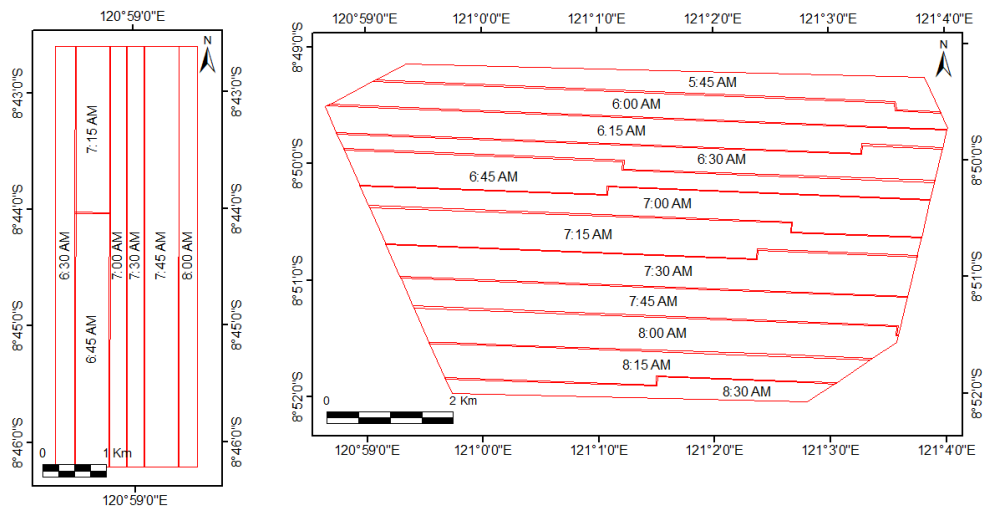
Figure 4.3 The polygons that are used for clipping the LiDAR DSM. Each polygon represents 15 minutes interval of the aircraft's trajectory during the image acquisition. On the left side is Block A, and Block B is on the right side.
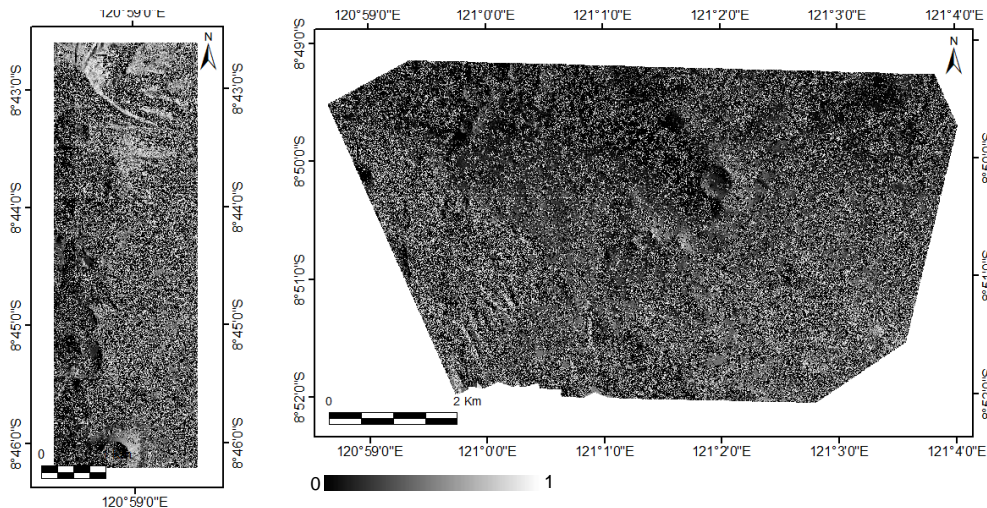
Figure 4.4 Hillshade DSM generated from a multi-angle illumination of LiDAR data for Block A (left) and Block B (right). The high value means the surfaces (also object above the surfaces) that facing to the Sun during the airborne data acquisition.

4.2.2.3. Landcover image

In this chapter, the land cover image was used to filter the false anomalies that associated with the vegetations and buildings. This image was derived from LiDAR point clouds reclassification using the Global Mapper software version 19. This reclassification was aimed to improve the point clouds data received from PT APG (operator of data acquisition) as it contained some misclassification. The point clouds were reclassified into five classes including ground, low vegetation, high vegetation, building, and other. The fundamental logic of this classification was based on the return signal and geometric properties of the point clouds.

The first step was the identification of ground points from the first and single returning signal. The parameter setup for ground reclassification is given in Table 4.3. The next step was an identification of points above the ground using a specific algorithm and parameter setups to classify points into low vegetation, high vegetation, and building classes. The reclassified point clouds then were inspected visually using the *LAS* tool in ArcMap software to filter misclassification error. For example, at the Mataloko Geothermal Field (MGF), some water vapor from an active geothermal manifestation was misclassified as high vegetation because of their similarity in the signal characteristic and point clouds geometry (see Fig 4.5). Therefore, in this case, the point clouds were manually assigned to class "other".

Table 4.3. Parameter setup for point cloud classification using Global Mapper software.

Ground classification parameter	Value	Non-ground classification parameter	Value
Bin size	2	Bin size	0.6
Minimum height departure (m)	0.3	Minimum height above the ground (m)	0.7
Maximum height delta (m)	100	Maximum co-planar distance (m)	0.2
Expected terrain slope (%)	30	Maximum vegetation distance (m)	0.2
Maximum building width (m)	100	Maximum co-planar angle difference	5
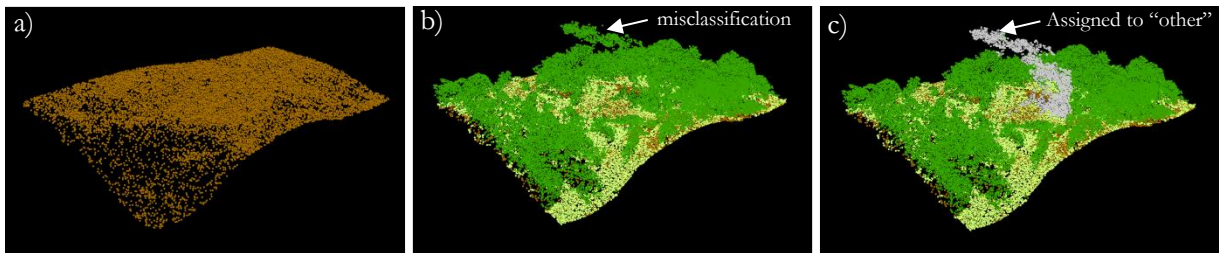
Figure 4.5 A) Classification of ground points as the first step of automatic point cloud classification. B) Misclassification of water vapour as vegetation classes in some geothermal manifestations in Mataloko Geothermal Field. C) This misclassification was manually fixed by reassigning these points into class "other" (see the grey point clouds).
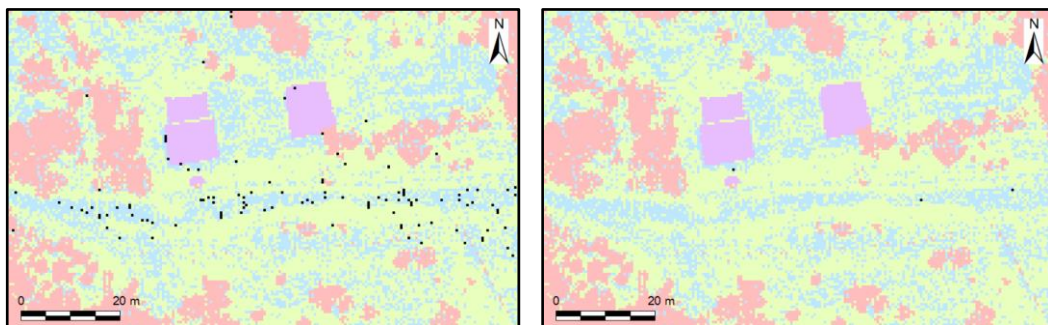
Figure 4.6 An image before (left) and after (right) interpolation of null value (the black pixels) using focal statistic of 5 x 5 neighbourhood majority in ArcMap. The null pixels were reduced after interpolation

The results of point cloud classification then were converted to the raster data file using *LAS to raster* tool based on the majority classification type. The spatial resolution of raster was configured to 0.51 meters (same with the other dataset). Some number of cells contained a null value because of point clouds spacing variation, where the point clouds have wider spacing than the desired raster resolution. Hence, some cells did not have any point to be sampled as raster value. The conditional interpolation technique then was applied to replace the null value with the majority value of the 5 x 5 neighboring pixels (see Fig 4.6). This process was performed through ArcMap raster calculator using the following formula:

$$New\ Raster = Con(\ IsNull\ ("raster\_name"), FocalStatistics\ ("raster\_name",$$
$$NbrRectangle(5,5), "MAJORITY"), "raster\_name") \tag{4.3}$$

Consider an assumption that the true anomalies are not associate with building and high vegetation pixels, therefore these classes were merged into one class (ID 2). The other classes including ground, low vegetation, and others were combined into a single class (ID 1). Overall, the landcover image used in DTC is a binary image containing Class 1 and Class 2 which represent the landcover that possibly associated with true anomalies and false anomalies, respectively.

4.2.3. Decision tree classification

Decision tree classification (DTC) is a statistical model in the form of a tree structure. It is built from a given training dataset to perform classification of a predictive class. A training dataset consists of several input variables X and a corresponding response vector Y as a discrete class membership. Training dataset is recursively split into smaller subsets using a machine learning environment based on impurity (entropy) of the dataset. The splitting criteria are searched from a single input variable that produces the largest impurity reduction of the output variable. The splitting continuously carried until the maximum reduction of impurity or when a specific parameter is set as a stopping criterion (Aldrich & Auret, 2013).

In this chapter, DTC was performed in R studio software using the *Ctree* module of the *Partykit* package (detail script in Appendix C). In the first step, a DTC model was built using a training dataset which consists of four input variables including albedo, hillshade, landcover, and DTF result. This training dataset also consisted of a predicted class which obtained from the ground truth data representing the sample location of the true and false anomalies. In the second step, the resulting DTC model was applied to the entire research area to predict the true anomalies. The detailed explanation of each step is provided in the subsections below.

4.2.3.1. Training dataset

The dataset of the sample class was built from fieldwork data that has been explained in section 4.2.1. The polygon of the hotspots sample was converted to a raster image based on the class ID. The raster value for the geothermal anomalies sample is 1, meanwhile for the non-geothermal anomalies sample is 2. This raster was generated with spatial resolution 0.51 meters which aimed to keep the similarity of spatial resolution and extent with the input variable images. The variable and sample class image were stacked in a single raster with the configuration given in Table 4.4. In total, this raster dataset has 48,675 pixels where each pixel contains information of the four variables and the information whether they are true anomalies or false anomalies. To avoid bias in the DTC model, a random sampling was used to collect a separate training and validation dataset from this raster dataset. 70% pixels of the sample dataset were used as a training data for building the DTC model. Meanwhile, 30% pixels of the sample dataset were used for validation. This random sampling was performed using the *train* function of the *CRAN* module.

Table 4.4. Band configuration of training dataset of decision tree classification. All bands have the same spatial extent and spatial resolution of 0.51 meters. Band 1 – 4 are the input variables (predictor), and Band 5 is a response class (predictand). The training dataset contains 48,675 pixels.

Band No.	Input dataset	Value range	Data type
1	Surface albedo	0.0 – 1.0	Float raster
2	Hillshade	0.0 – 1.0	Float raster
3	Landcover	1 and 2	Binary raster
4	DTF result	0.0 – 1.0	Float raster
5	Sample classes	1 and 2	Binary raster

4.2.3.2. Model creation and validation

The determination of the DTC model was carried out through an evaluation of the tree structure in term of the robustness and complexity of the model. A too complex structure tended to overfit the dataset by modeling the noise rather than the training dataset itself. Meanwhile, a too simple tree structure prone to give poor performance on the prediction. In this chapter, the overfitting was avoided by pruning the parameter of the tree model. Since the tree structure could grow without limits, therefore a *mincriterion*, *minsplit,* and *maxdepth* parameter were set as splitting and stopping criteria of the tree.

According to (Hothorn, n.d.), the *mincriterion* and *minsplit* determined whether the node is split or not, the higher the value, the simpler the tree is growing. The *mincriterion* has a range value from 0-1. For example, *mincriterion* = 0.95 means the p-value must be smaller than 0.05 in order to split the node. This p-value is a statistical parameter which indicating the deviation from the partial hypothesis of the independent variable. *Minsplit* determines the splitting criteria of a node based on the minimum sum of weight statistic. *Maxdepth* limits the growth of the tree based on the depth level. In this chapter, the DTC model was produced with the *mincriterion* = 0.95; *minsplit* = 1000; and *maxdepth* = 4. The resulting model then was applied to the validation dataset to evaluate the performance of classification. The output classification then was compared to the sample dataset (ground truth data) using a confusion matrix. This matrix provides information about misclassification and the level of accuracy of the DTC model.

4.2.3.3. Prediction

In the final stage, the validated model was used to predict the geothermal (true) and non-geothermal (false) anomalies for the entire study area. The prediction was carried using *predict* function which can produce several responses including a hard classification result and a probability result. Here, we did not used the hard classification results as the final output, but the probability information because it could explain with what confidence a pixel is classified as the true anomaly.

4.3. Results

4.3.1. True and false anomaly characteristic

The preliminary interpretation of the airborne TIR orthoimage as well as fieldwork was carried out to understand the characteristics of the geothermal and non-geothermal anomalies. During the fieldwork 78 geothermal hotspots and 47 non-geothermal hotspots have been measured (see Fig 4.7). The geothermal hotspots are mainly located at Mataloko Geothermal Field (MGF). In this location, the geothermal hotspots consist of mud pools, fumaroles, and hot springs with the temperature range between 37.5° to 95.3°C. The size of geothermal hotspots varies between 0.5 m² to approximately 93 m². Some examples of the geothermal hotspots and their expression in the TIR orthoimage are given in Fig 4.8 (details in Appendix E). Based on this figure, the shape and pattern of the geothermal anomalies are clearly shown by the airborne TIR orthoimage. However, the hotspot's temperature in the airborne TIR orthoimage

shows significant discrepancy with the actual temperature measured in the field (Fig 4.9). Where the airborne based temperature for all presets underestimated the ground-based temperature measurement (discussed further in Chapter 7).
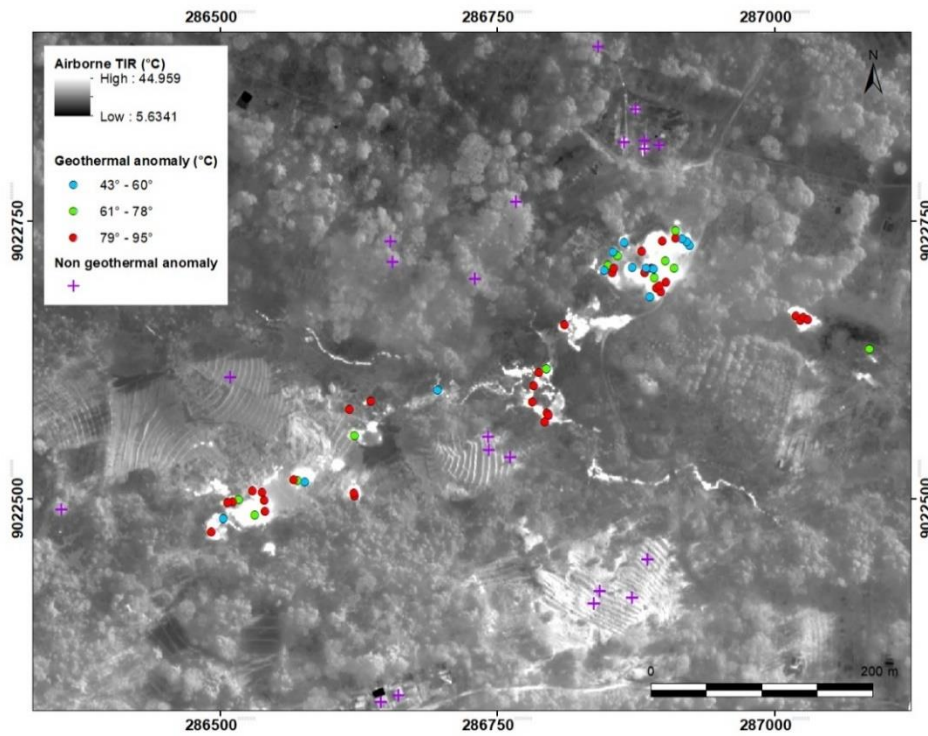
Figure 4.7 Distribution of geothermal anomalies in Mataloko Geothermal Field that were measured during fieldwork draped on top of the airborne TIR orthoimage. The background image was stretched using the 1st standard deviation statistic. Some non-geothermal anomalies were observed at the field (cross sign).
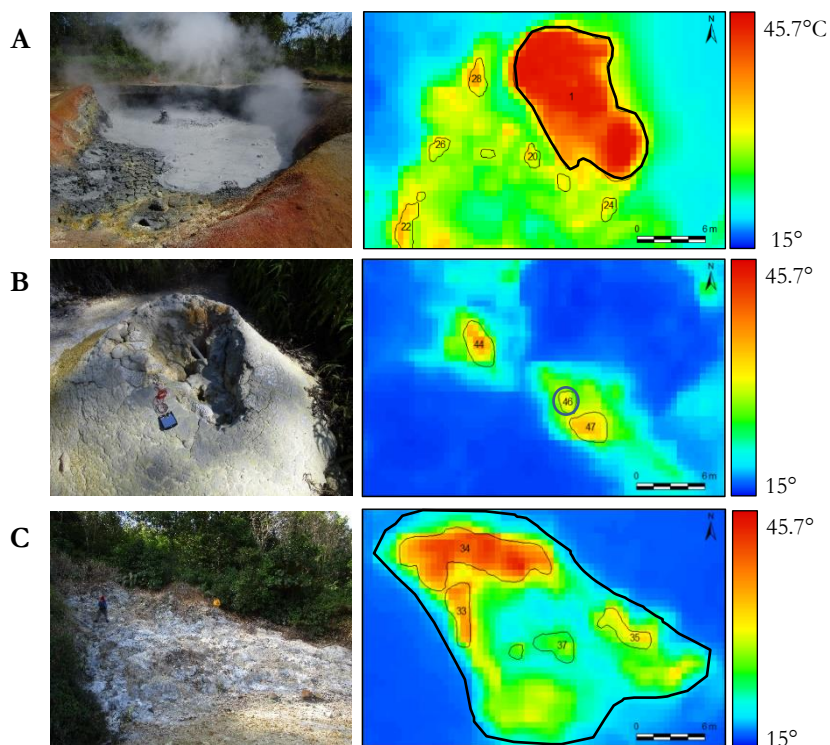
Figure 4.8 Some of the expression of geothermal hotspots in the field (left) and in TIR orthoimage (right) for A) Mud pool, B) mud volcano, and (C) fumaroles with steaming grounds.
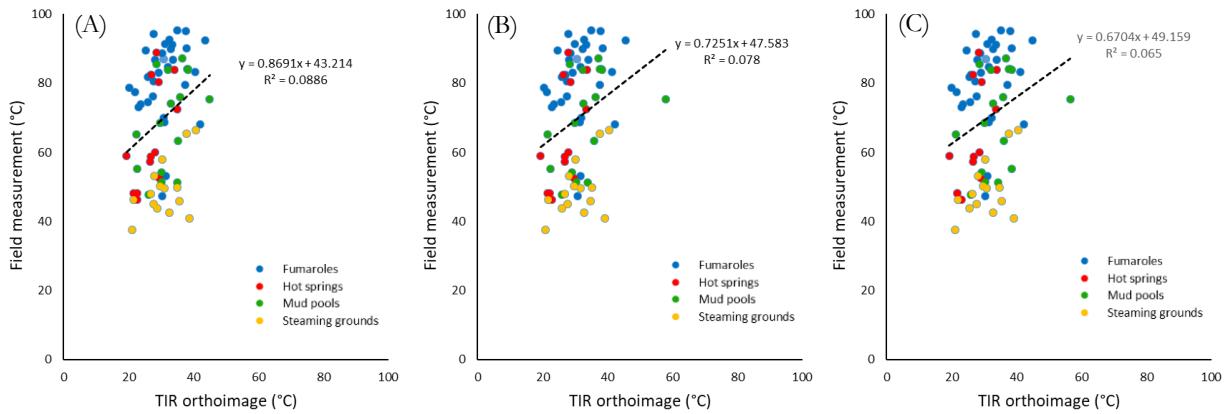
Figure 4.9 Scatter plot of geothermal hotspot temperature measured in the field (Y-axis) and from the airborne TIR orthoimage for Preset 0 (A) and Preset 1 (B) and Preset 2 (C). The scale of X and Y axis is 1:1. These graphs show an underestimation of geothermal hotspot temperature measured by airborne TIR orthoimage for all presets. The three presets show similar value although they have different temperature sensitivity range. The only significant difference is shown by a mud pool (green) where the temperature in Preset 1 and Preset 2 is higher than Preset 0.

Based on the preliminary interpretation of the TIR orthoimage and the ground truth data, it was found that the non-geothermal anomalies are mainly associated with buildings, vegetations, and dark soils with the temperature varies between 25 to 44°C. To give some example, these false anomalies objects are presented in Fig 4.10. From that figure, it is apparent that the type of material and color properties of an object significantly determine the temperature in the airborne TIR orthoimage. For example, the oxidized metal-roofs has a higher temperature than the white fresh metal roofs and the clay tile roofs. Similarly, the dark soils are easily misinterpreted as an anomaly because it absorbs the sun radiation faster than the altered or vegetated soils with a lighter color. Furthermore, the direction of the surface to the sun also influences the temperature variation of an object, where a surface facing the sun often has a higher temperature than a surface facing away from the sun or in the shadow.
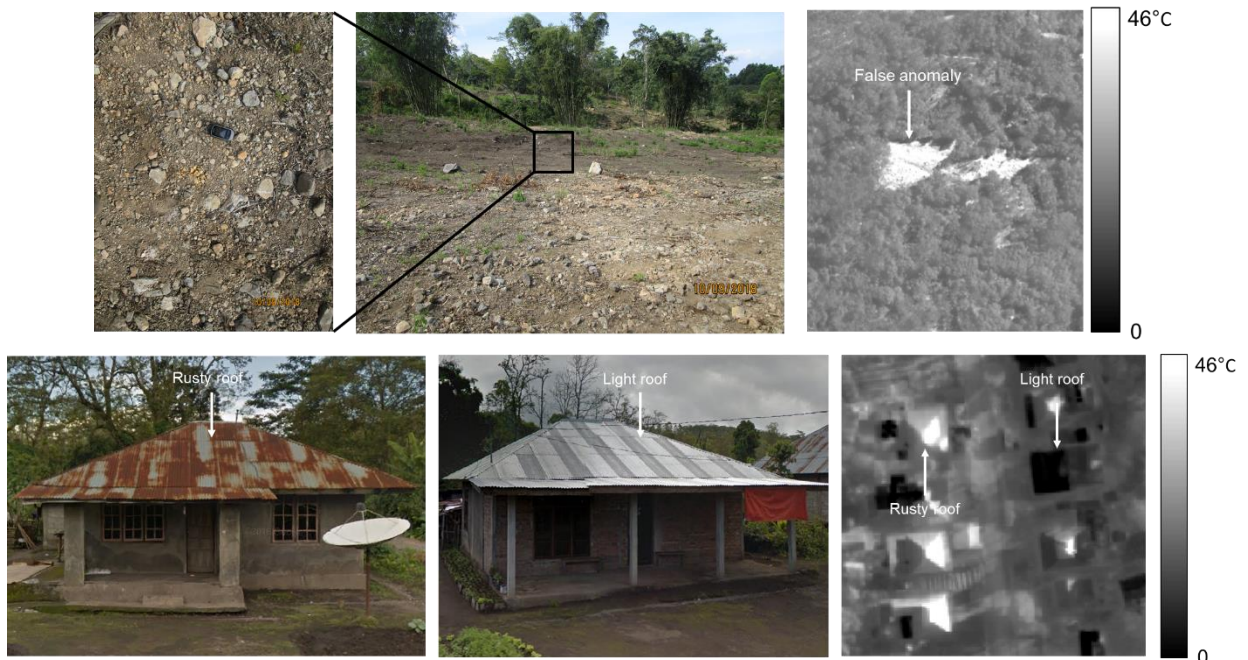
Figure 4.10 Some expression of the false anomalies that were observed in the field and in the TIR orthoimage. The dark soils show a significant different contrast with the surrounding objects due to their higher temperature (top). The rusty roof (bottom left) has a higher temperature than the light roof (bottom middle) that made from the same metal material. This infer that the dark objects (low albedo) have a higher temperature than the brighter objects.
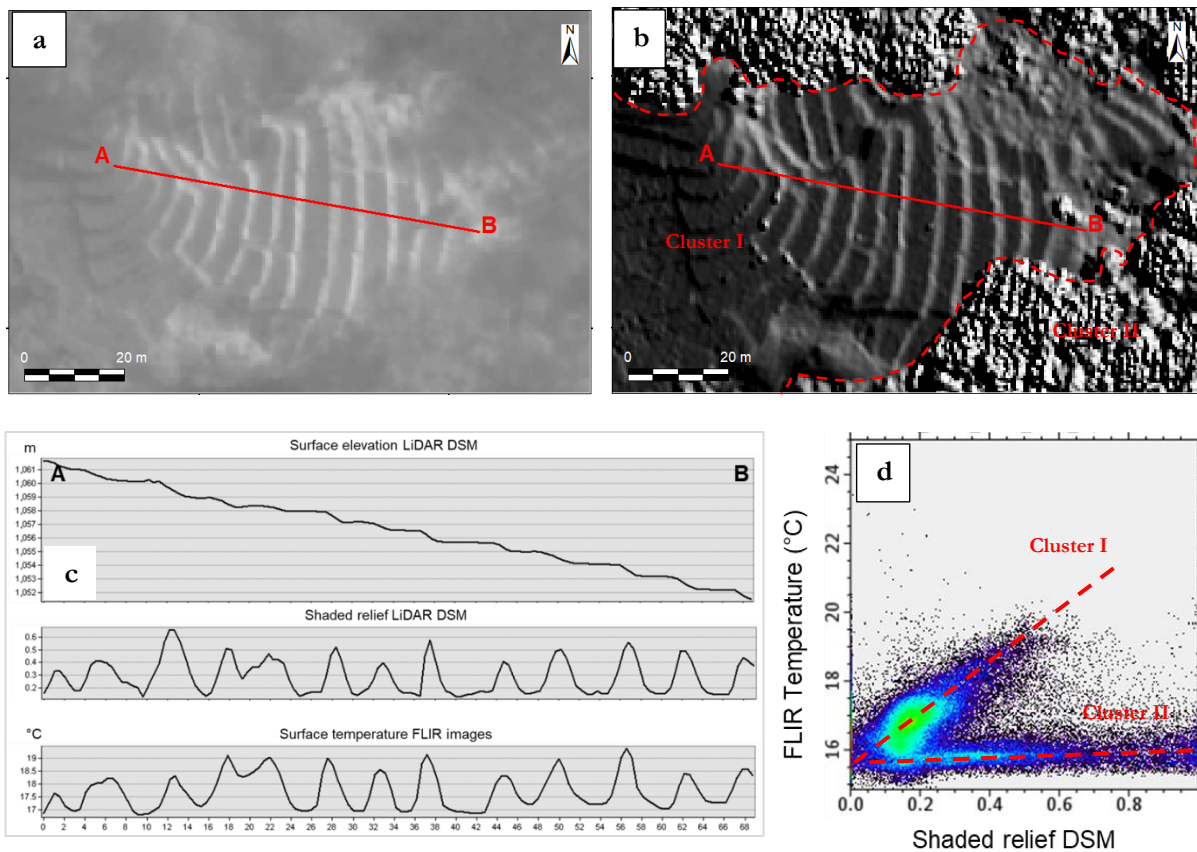
Figure 4.11 Graphical representation showing the relationship between topography, shaded relief DSM, and temperature of airborne TIR images of a terraced area in Mataloko Geothermal Field. The image a) and b) was illuminated in NE direction. The cross-section AB in figure c) show a significant correlation where the high shaded relief (hillshade) DSM that correspond to the slope facing to the Sun coincide with the high temperature of airborne TIR images. d) The same pattern also shows in the scatter plot where the Cluster I that belongs to the bare grounds has a high positive correlation between shaded relief (hillshade) with airborne temperature. Meanwhile, Cluster II that belongs to the vegetations has relatively lower correlation between these two variables.

Some inspection on the airborne TIR orthoimage and the hillshaded LiDAR DSM reveal a strong correlation between surface temperatures and the slope with respect to the sun's incident angle. Fig 4.11 shows a cross-section through a terraced area in MGF which shows a striping false anomalies pattern, where the higher temperature coincides with high hillshade value and the slope pointing to the sun's rays. Meanwhile, the relatively low temperature coincides with a low hillshade value. In addition to the cross-section, a scatter plot diagram provided in the same figure shows two main clusters, where the stronger correlation is given by the grounds and the weaker corresponds to the vegetated area. As this example has shown, the false anomalies potentially occur in an area with a low incident angle (high hillshade value) toward the Sun's rays.

4.3.2. Dynamic Threshold Filtering (DTF)

The DTF result (Fig 4.12) shows the distribution of the temperature anomalies which was separated from the background temperature. The value in this result indicates the probability of the pixel as an anomaly, where the higher value means that the pixels are more outstanding than the lower value. From this figure, it is apparent that DTF is not designated as the final output of geothermal anomalies detection because it also includes many false anomalies in the results. Nevertheless, since the output value of DTF is independent of the uneven heating by the sun illumination across the study area, this result has become an

important input in the DTC model. Regardless surface temperatures, the value of this DTF results have opened the same chance both for the large-outstanding anomalies and small-local anomalies to be considered as the true anomalies in the DTC model. Additionally, using this information the DTC could objectively assess the true and false anomalies based on this relative value with the other three designed variables, instead of only relying on the surface temperature which shows many variabilities that are not related to the geothermal activity.
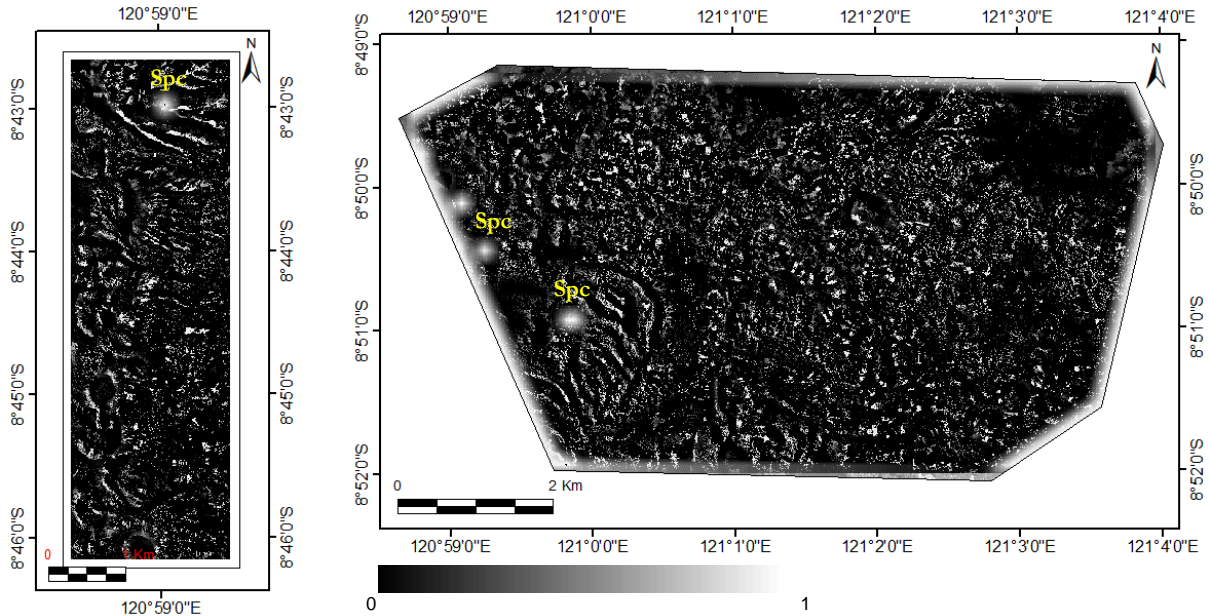
Figure 4.12 The result of the dynamic threshold filtering (DTF) for Block A (left) and Block B (right). The images indicate the temperature anomalies that were discriminated from their background. The brighter pixels show the anomalies that have more outstanding temperature than the surrounding pixels in a subset window. Some speckles are shown in this result due to the gaps in the input TIR orthoimage (see label *Spc*), also in the edges of Block B that occurred because the extent of input images is not rectangular.

4.3.3. Decision Tree Classification (DTC) model

The DTC model that was built from the training dataset is given in Fig 4.13. In term of the tree structure, this model consists of 11 split nodes and 12 leaf nodes. The split nodes are the 'if conditional' which split the training dataset into a binary path (Yes and No) based on the criteria of input variables. The leaf nodes are the endpoints of the tree that represent the output classes and the probability of the classification results. In this case, the output classes are the true anomaly (value = 1) and false anomaly (value = 2). Meanwhile, the probability value indicates the confidence level of training samples to be classified as the true anomaly. The probability value of 1 infers that the classified sample on a leaf node contains only true anomalies.

Leaf nodes with the highest probability are the main target that is most likely associated with the geothermal temperature anomalies (true anomalies). Based on the DTC model the highest probability to encounter true anomalies is given by the leaf nodes number 4 and 1 (Fig 4.13). The leaf node 4 as the highest probability can be achieved if the training dataset has relatively low hillshade (<0.244), high DTF result value (>0.898), relatively high albedo (>0.134), and the landcover type should be either bare ground or low vegetation (value = 1). The second highest probability given by the leaf node 1 where the criteria are the same as in the leaf node 4 except that the hillshade is lower than 0.13. On the other hand, the lowest probability (probably false anomalies) is given by the leaf node 5 and 9 where the land cover is building or high-vegetation (value = 2). Moreover, the relatively low probability is given by the leaf node 6-8 indicating the low-vegetations or bare grounds that are facing the Sun (high hillshade).
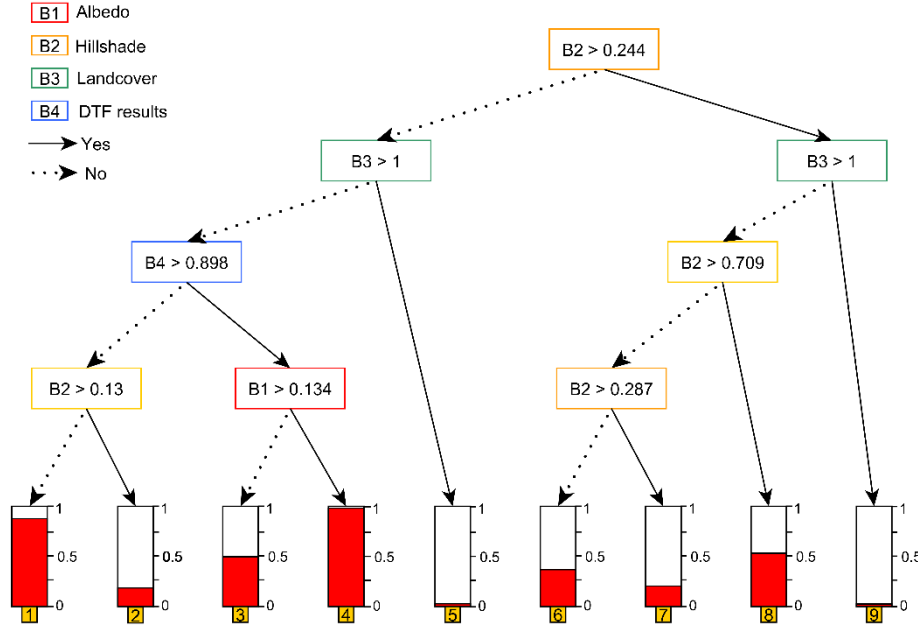
Figure 4.13 DTC model of the training dataset. The bar graphs at the bottom side are the leaf nodes which represent the probability of the classification results. The highest probability (true anomaly) given by the leaf nodes number 4, meanwhile the lowest probability (false anomaly) is given by the leaf nodes number 5 and 9.

Table 4.5 Confusion matrix of the DTC prediction results using the validation dataset (total 10,195 pixels). The overall accuracy of the DTC model is 87.9%. T = True anomaly and F = False anomaly.

		Reference		Total	Commission error
		T	**F**		
Prediction	**T**	**2961**	191	3152	0.061
	F	1036	**6007**	7043	0.147
Total		3997	6198	10195	
Omission error		0.259	0.031		**0.120**

Performance of the DTC model was assessed using the validation dataset that was described in Section 4.2.3. The confusion matrix in Table 4.5 shows that the overall accuracy of the DTC model is 87.9% with a kappa of 0.737. The misclassification occurred in both classes where 25.9% of the true anomalies are classified as false anomalies. On the other hand, 3.1% of the false anomalies are classified as true anomalies. This misclassification error generally occurred due to the noise in the training dataset or as a result of the pruning parameter to avoid overfitting. However, the overall accuracy of this DTC model is likely to be a good result considered a high number of the sample pixels.

4.3.4.   Geothermal temperature anomaly prediction

The DTC model was used to predict the location and distribution of the geothermal temperature anomalies. As explained in Section 4.3.3 that the true anomalies are associated with the leaf node 4 and 1 (probability > 0.89). Here, the pixels with probability greater than 0.89 are potential as the true anomalies, and below 0.89 were filtered out as the false anomalies. The distribution of the true anomalies is given in Fig 4.14. From this figure, it is apparent that most of the false anomalies has been removed significantly, where there is not a clear pattern of the non-geothermal anomalies remaining. On the other hand, this figure still represents almost all the measured geothermal anomalies in MGF (location 1). In addition, warm spring with temperature ~35°C in the river bed near the Golewa village (location 2) that was not included as the training dataset is detected in the result. Although these findings prove that the DTC model performs well to detect the geothermal temperature anomalies and removes the false anomalies,

some minor noises that have a relatively similar characteristic with the true anomalies (similar albedo, hillshade, DTF, and land cover) still exist in the results (discussed in Chapter 7).

The spatial pattern of the identified geothermal temperature anomalies shows some interesting pattern and distribution (see Fig 4.15). We observe there are two main orientations of the geothermal surface anomalies including NE-SW and NW-SE trends. The NE-SW trend looks obvious considering the alignment of the two main manifestations in location 1 (area X and Y) and the pattern of anomalies in location 2. Meanwhile, the NW-SE anomalies trend is also apparent in the Wae Luja river and some steaming ground (see line K, L, M). In addition, location Z shows anomalies oriented in a circular form. These alignments of the geothermal temperature anomalies were interpreted together with the lineament patterns derived from LiDAR DEM and subsurface data (Chapter 6).
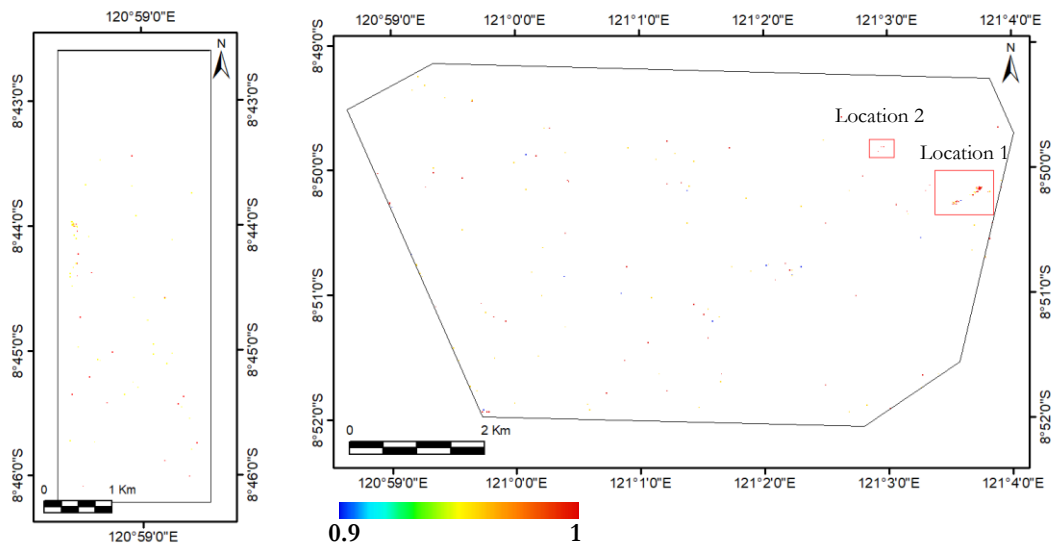
Figure 4.14 Prediction results of the DTC model. The coloured pixels show probability of the true anomalies for Block A (left) and Block B (right). The probability less than 0.9 was filtered out. Two geothermal anomaly localities were identified including Mataloko Geothermal Field (location 1) and a river in Golewa village (location 2). No geothermal temperature anomalies were confirmed in the other location beyond these locations.
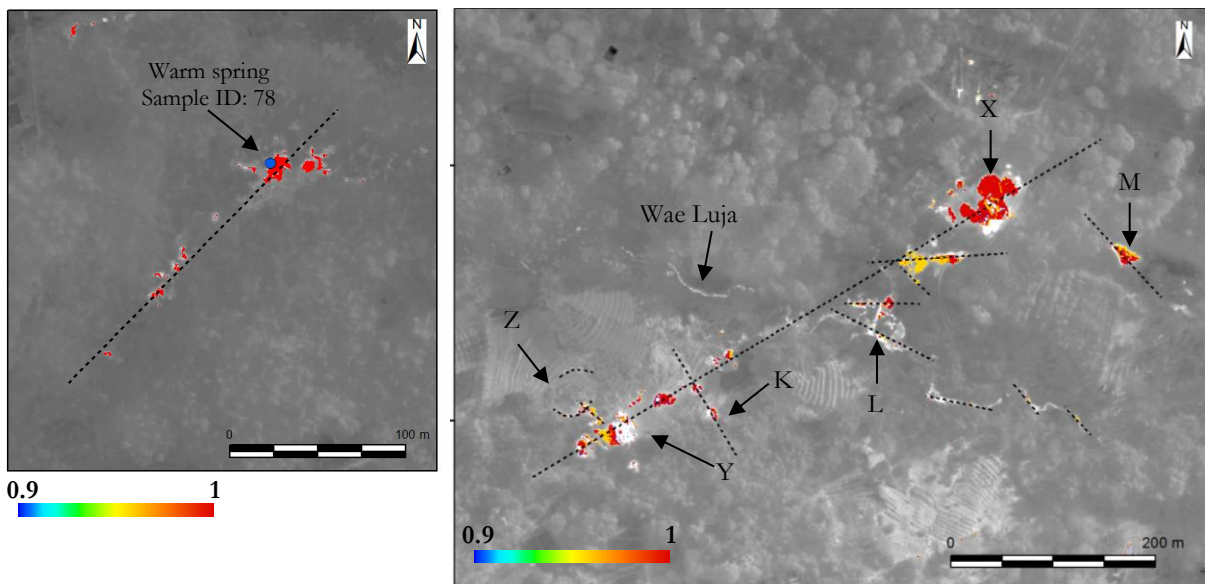
Figure 4.15 Predicted geothermal anomalies based on the DTC model in Location 2 (left) and Location 1 (right) (with the airborne TIR orthoimage as background). The interpreted alignments of the anomalies are shown by the dashed lines. There are two main orientations of the anomalies including NE-SW and NW-SE pattern.

5. STRUCTURAL ANALYSIS OF GEOTHERMAL AREA USING AIRBORNE LIDAR DATA

5.1. Introduction

Spatial distribution of the geothermal anomalies is commonly controlled by geological structures which allow geothermal fluids to flow from the subsurface to the surface. In this chapter, the structural control of the geothermal anomalies is analyzed based on the lineament interpretation of the LiDAR DEM. A lineament in this chapter is specifically defined as a linear feature on the LiDAR DEM that represents a natural object like geological fault, fracture, and morphological feature which presumably reflects a subsurface phenomenon. Meanwhile, a linear feature that produced by an artificial object such as road, building, pipeline, agriculture ground is considered as a noise which needs to be filtered out.

LiDAR-based DEMs allow the interpretation of lineaments at a detailed scale. In this chapter, with a spatial resolution 0.5 meters, the interpretation of the LiDAR DEM was focused on identification of local structures to interpret the controlling factor of the identified geothermal temperature anomalies (Chapter 4) without neglecting the regional structures from the previous satellite DEM-based studies. Moreover, the results of this chapter are interpreted in Chapter 6 to establish a model describing a possible relationship between the geothermal temperature anomalies and the structural pattern as predictors of a geothermal reservoir and fluid pathway of the geothermal system.

5.1.1. Existing study

There is a large number of published studies (e.g., Meixner et al., 2017; Saepuloh et al., 2018) that describe an investigation of geological structure based upon lineament features in remote sensing data. Three main approaches have been used to extract lineament information such as a) automated extraction, b) semi-automated extraction, and c) manual interpretation by a human operator. A manual interpretation technique can be a quick, cost-effective, and powerful method for lineament extraction. However, it has its limitation in low reproducibility and its strong dependency on scale factor, illumination azimuth, perception to the lineament, and experience of an operator (Scheiber et al., 2015). On the other hand, semi-automated and foremost automated techniques which rely on computing algorithms were found to be more objective and more reproducible for lineament extraction than a manual interpretation method.

Several algorithms have been established for automatic lineament extraction such as Segment Tracing Algorithm (STA), Hough Transformation (HT), and LINE module. As a widely used algorithm, STA works by detecting a line of the adjacent pixels as a vector element based on a local variance of gray level images and connecting retained line elements along their expected direction (Koike et al., 1995). STA has the advantage of being able to extract lineament parallel to the sun's azimuth as well as those in shadow areas. Differently, the HT works by enhancing the edge features in an image, then transforming it from an image space into a parametric space to obtain the edge direction according to the trend of the local linear feature (Han et al., 2018). The position and direction of the detected edges then are extracted as line features in an image coordinate space. Some optimization of HT algorithm has been developed to remove the noise that often occurred in the HT method, such as the Optimized-HT (Fitton & Cox, 1998) and the tensor voting coupled-based HT (Han et al., 2018).

The LINE module is a tool in PCI Geomatica software made for an automatic lineament extraction of remote sensing images. This algorithm relies on a *Canny* edge detector which is performed by filtering an input image using a Gaussian filter. The pixels which do not represent a local maximum are suppressed.

Then, the threshold is applied to binarizes the filter images. After that, the binary image is converted into the vectors using a curve extraction function (Mallast et al., 2011). In addition to the LINE module, the recently developed Multi Hillshade Hierarchic Clustering (MHHC) workflow was designed to remove the artifact that often shows up in the results of the LINE module (Šilhavy et al., 2016). The MHHC works firstly by extracting the lines from multi-hillshade DEM using the LINE module itself. Secondly, it filters the noise by introducing 'protolineaments' which represents the accumulation of the extracted lines from each hillshade DEM input. Then the protolineaments is converted into a binary raster to identify an area that has a high occurrence of lines. The lines in a low-frequency area are assumed to be noise and removed. Thirdly, the remaining lines are clustered based on their spatial distribution then a single line is extracted from each cluster as a representation of the linear features from different hillshade DEM. The MHHC workflow has the advantage to produce an unbiased lineament result as a basis of quantitative analysis for answering geoscientific problems.

Based on the advantages of the MHHC workflow over the other approach, the working principle of the MHHC workflow was implemented in this thesis to extract lineament from hillshaded LiDAR DEM as a basis of an interpretation of the surface structures in a geothermal system. Since the original MHHC algorithm was not available for this research, a slightly modified method of the MHHC was implemented using the available tools in PCI Geomatica and ArcMap. In this thesis the modified MHHC workflow is divided into five main steps including 1) automatic lineaments detection using the LINE module, 2) lineaments filtering, 3) lineament clustering, 4) line singularization, and 5) geostatistical analysis (See Fig 5.1).
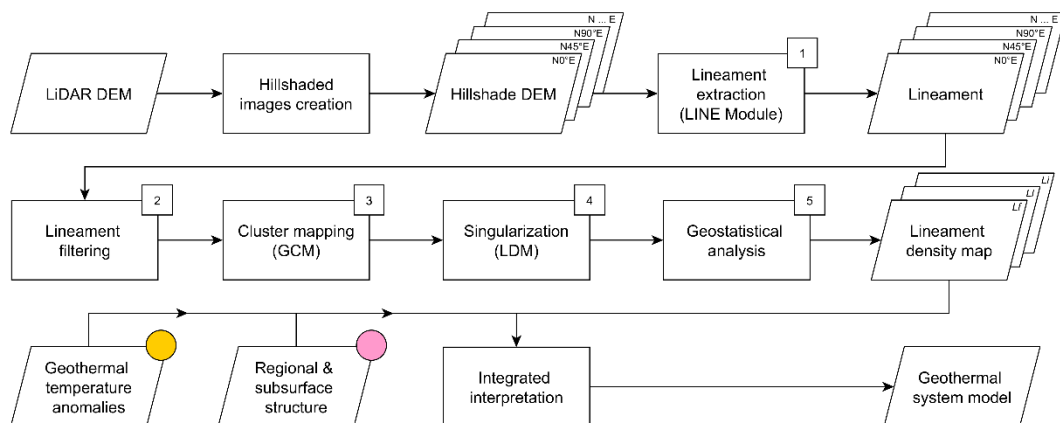
Figure 5.1. The workflow of structural analysis using LiDAR DEM in this chapter. The steps 1-4 were adapted from the MHHC method. The yellow circle indicates the result from Chapter 4 meanwhile the light red circle indicates the data from literatures. The integrated interpretation of structures and geothermal anomalies distribution with subsurface data is presented in the next chapter.

5.2. Methodology

5.2.1. Multi-hillshaded LiDAR DEM creation

Masoud and Koike (2011) described a dependency of automatic lineament extraction to the illumination azimuth and elevation angle. They explained that linear features with strike perpendicular to the illumination azimuth could be more emphasized than others parallel to the illumination direction. To overcome this issue, as suggested by many publications (e.g., Abdullah et al., 2010; Šilhavy et al., 2016) this research used a multi-directional illumination to create hillshade images of the LiDAR DEM. A low solar-elevation angle (30°) was selected for the eight different illumination azimuths with 45° interval (0°, 45°, 90°, ….). This step yielded eight hillshade images that were used as inputs in the LINE module for lineament extraction (see Fig 5.2).
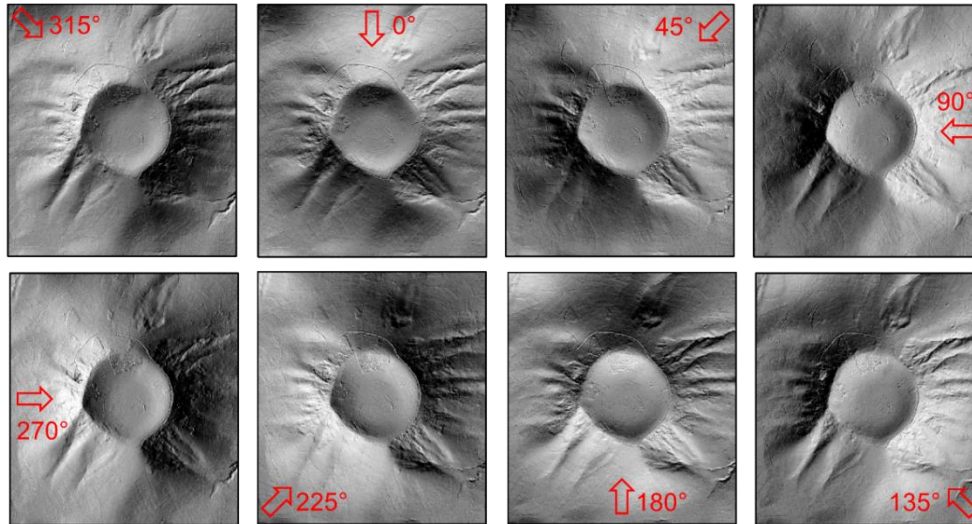
Figure 5.2. A monogenetic volcano in the study area that is presented in the multi-hillshaded LiDAR DEM images. The arrows show sun azimuth angle for each image with 45° interval and sun elevation 30°. The linear features with orientation perpendicular to the illumination direction are more emphasised.

5.2.2. Automatic lineament extraction

As described in section 5.1.1, the LINE module in PCI Geomatica software is working in three automatic sequences. Firstly, the input images were filtered using a Gaussian filter to enhance the edges of the adjacent pixels. The moving windows size which represented by filter radius (RADI) parameter determine the gradient of edge enhancement. The pixels that did not represent a local maximum were suppressed. In the second step, several parameters in Table 5.1 were considered as thresholds to convert the edge-enhanced images into a binary image. In the last step, a binary image was thinned using a thinning filter and converted to vector as the extracted lines. The author suggests referring to the internal PCI Geomatica Help for a detailed description of the LINE module workflow and parameter setting (PCI Geomatics, 2018).

Table 5.1. The default and optimal parameter settings for automatic lineament extraction of LiDAR DEM using the LINE module in PCI Geomatica. The abbreviation of each parameter was adapted from Mallast et al. (2011).

ID	Parameter	Default	Optimal
RADI	Filter radius	10	10
GTHR	Edge Gradient Threshold (0 – 255)	100	75
LTHR	Curve Length Threshold (pixel)	30	200
FTHR	Line Fitting Error Threshold (pixel)	5	10
ATHR	Angular Difference Threshold (0 – 90°)	30	30
DTHR	Linking Distance Threshold	20	20

In this thesis, the optimal parameters for the LINE module were carried out through the parameters tweaking by observing the outcomes of the lineaments qualitatively. The default parameter in PCI Geomatica was applied as the starting point. Then some parameters were changed one by one to evaluate the sensitivity of the parameters to the output lineaments. The most sensitive parameters were LTHR and FTHR which represents the threshold value for curve length and line fitting respectively. The default value of LTHR resulted in high noise levels in the extracted lineaments where the artificial features like agriculture fields are dominant instead of the geological features (see Fig 5.3). Therefore, a higher value of LTHR was set to reduce these noises. The higher FTHR was set to produce more straight line because the default value allows the lines to be fitted together which made the extracted lines curvier. The GTHR was decreased from the default parameter to allow the lower gradient (less contrast) to be extracted as the

edges. The other parameters except these three parameters were left at their default value. This extraction yielded eight sets of lineament vectors.
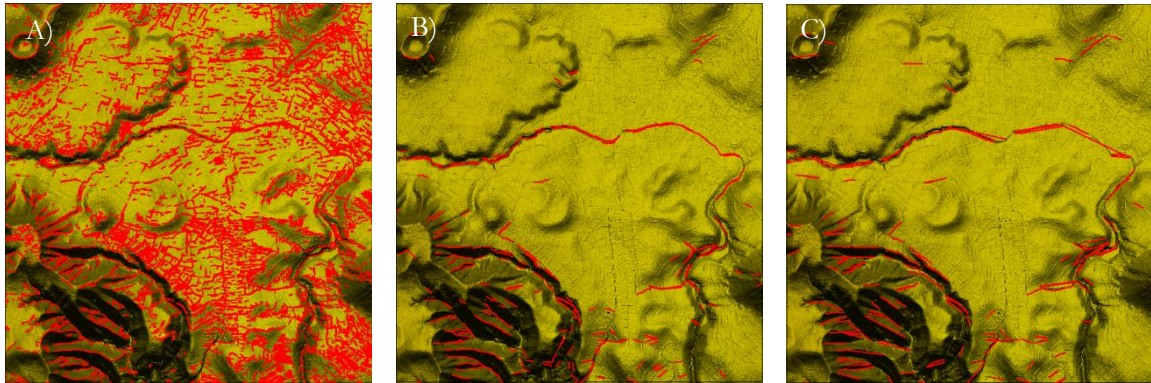
Figure 5.3 A) The extracted lines in a small part of study area using default parameter settings of the LINE module. B) With the increase of LTHR to 200 pixels, the noises was reduced significantly. C) The FTHR was decreased to make the lines more straight.

5.2.3. Lineament filtering, clustering, and singularization

In the following step, the noise was eliminated using a spatial-frequency (SF) filter. This method was based on the observation that the noises have a temptation to be isolated and disconnected. Hence, they often found to be in a low frequency within a particular area. In the first step, the eight sets of the extracted lineaments were assembled into a single layer. Secondly, the line density raster was computed, and then a threshold was set to indicate a location that potentially contained noises. The pixels with the value below a threshold were highlighted and then converted into a polygon. Finally, the lines located inside or intersected with this polygon then were removed. In addition, to removing the noises (particularly the roads) the road network layer from the Open Street Maps (OSM) was used to select and remove the extracted lineaments within a distance and parallel to this road network.

As can be seen from Fig 5.4, some lineaments extracted from different hillshaded DEM directions congregated in the same position and formed a cluster. A technique adapted from the MHHC method was performed to singularize the multi-lines clusters into a single line representation. This step was essential to avoid an overestimation of the extracted lineaments from different hillshade DEM in the same location. This singularization was performed in ArcMap through several steps as follow:

i.   **Grouping analysis for cluster mapping (GCM)**: Grouping analysis toolset was applied to clusterize the adjacent lineament features into a group based on their similarity of certain variables, such as length and direction of the extracted lines. The GCM algorithm considered a *K*-nearest neighborhood parameter as a spatial constraint for the grouping. The lineament features on closer proximity have a high chance to be grouped as a cluster. This tool requires the input of the number of output clusters as a basis of grouping (ESRI, 2018a).

ii. **Linear directional mean (LDM)**: It calculated a mean direction and length of the lineaments within a group and produced a single line as a representation. The location of the extracted lines was determined on the central mass of the grouped lineaments. The equation of LDM is given in Eq 5.1, and variance of the direction given in Eq 5.2. This variance indicates of how much the direction of a single line deviates from the directional mean. Where θ_i is the direction of a set of the lines from a single origin (ESRI, 2018b).

$$LDM = \arctan \frac{\sum_{i=1}^{n} \sin \theta i}{\sum_{i=1}^{n} \cos \theta i} \qquad (5.1)$$

$$Variance = 1 - \frac{\sqrt{(\sum_{i=1}^{n} \sin \theta i)^2 + (\sum_{i=1}^{n} \cos \theta i)^2}}{n} \qquad (5.2)$$
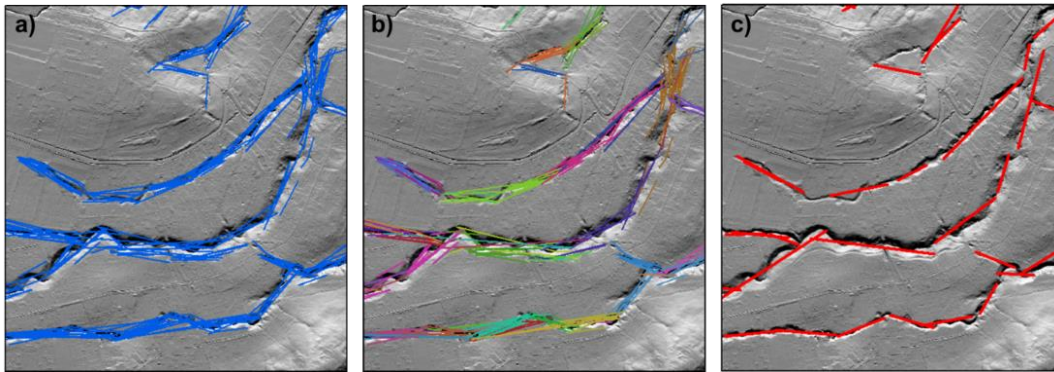
Figure 5.4 A) lineament extracted from eight directional hillshade LiDAR DEM. B) Clustering a set of lineaments based on their direction, length, and spatial distribution using Grouping Analysis for Cluster mapping (GCM). C) singularization of group of lineaments using Linear Directional Mean (LDM)

5.2.4. Geostatistical analysis

According to Saepuloh et al. (2018), highly fractured zones with high permeability have been found to be prospective locations for geothermal potential. To understand the relationship between the distribution of geothermal surface anomalies with the surface structures, a quantification of the extracted lineament was carried out together with their directional pattern. Three indices as suggested in Saepuloh et al. (2018) were applied here to quantify the density of the extracted lineaments per unit area, including a) lineament intersection (*Li*, counts of points/cell), b) lineament frequency (*Lf*, counts of lines/cell), and c) lineament length (*Ll*, meters/cell). Where *Li* describes the number of the intersected lineaments which may extend the estimated damaged zone due to multiple effects of fracturing. *Lf* is the number of extracted lineaments, and *Ll* is the total length of lineament in a grid. These indices were calculated in a grid with a cell size of 250 x 250 meters. Additionally, the frequency of lineament directions is presented in a rose diagram to analyze the main pattern of the lineaments.

5.3. Results

The results of automatic lineament extraction are shown in Fig 5.5. This figure represents the lineaments after LINE module extraction, SF filtering removal of roads and circular feature related to volcanic cones, and line singularization using GCM and LDM analysis. The extracted lineaments have a positional and directional uncertainty that is indicated by the variance number (Fig 5.6). In this result, there are 8% of the total lineaments of Block A and Block B with variance greater than 0.25 (the maximum variance for 45° interval of the hillshaded LiDAR DEM). To minimize the error in the geostatistical analysis, the lineaments with variance greater than 0.25 were removed.

The major direction of the lineaments is N100°E for Block A and N60°E for Block B (Fig 5.6). The main lineament direction for Block B is aligned with the NE-SW trend of the *en échelon* structure described in Section 2.1.1. This NE-SW lineament direction also reflects the pattern of the secondary magmatic lineament of young volcanic cones interpreted by Akasako et al. (2002) (see Fig 5.7). Differently, the dominant E-W lineament direction for Block A is not correlated to any regional structure pattern. This E-W pattern is somewhat perpendicular to the clustered monogenetic volcanoes of the Inielika complex

extending in the north-south direction. Most of the extracted lineaments in Block A are controlled by the drainage pattern of the Inielika volcanic complex which dominantly oriented to the east direction.
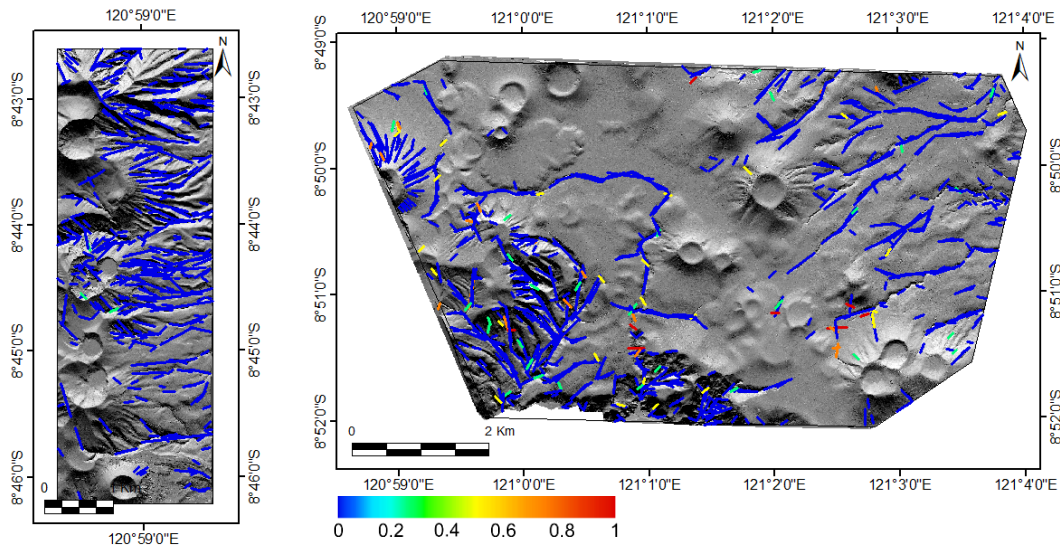
Figure 5.5 The extracted lineaments from multi hillshaded LiDAR DEM using LINE module after being filtered, clustered, and singularized. The colour indicates variance of the singularized lineaments (before removal of the variance > 0.25).
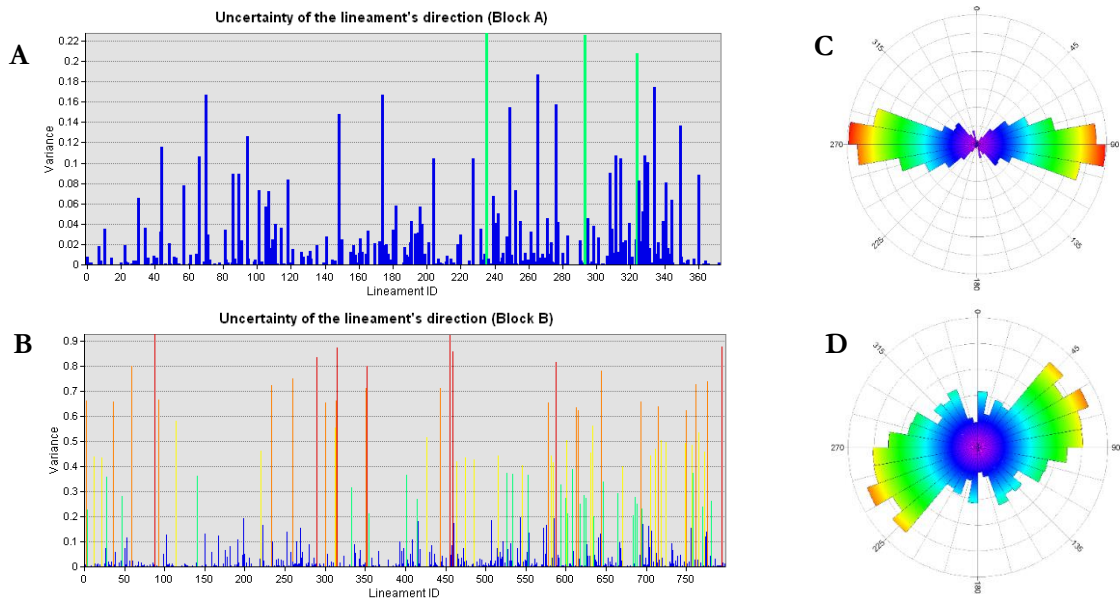
Figure 5.6 A) and B) show the graphic variance of the extracted lineaments in Fig 5.5 (with the same colour scheme). C) The rose diagram of the final lineaments of Block A with the main direction is E-W, and D) the main lineament direction of Block B is NE-SW.

Three lineament density indices including lineament frequency (Lf), lineament length (Ll), and lineament intersection (Li) were calculated to quantify and evaluate the pattern of surface structures. The average lineament frequency for Block A is 0.627 counts/cell meanwhile for Block B is 0.910 counts/cell (cell size 250 x 250 m). The highest lineament frequency is mainly distributed along the high-relief topographies such as the flanks of the volcanoes, valleys, and rivers (See location A, B, C, and D at Fig. 5.7). Additionally, some of the moderate lineament frequency in Block B (Lf of 3 to 6 counts/cell) are located around the regional lineaments and the faults gathered from several sources (Akasako et al., 2002;

Nasution et al., 2000). In location E and F, some of the moderate lineament frequency zones coincide with the distribution of the geothermal temperature anomalies described in Section 4.3.4. The orientation of the moderate lineament frequency indices around location E and F shows an NE-SW trend which is aligned with the regional structures (see Fig 5.7 A) and with the main pattern of the geothermal temperature anomalies shown in Section 4.3.4.

The average lineament length for Block A is 543 meters/cell meanwhile for Block B is 239 meters/cell. The lineament intersection index map shows an average value of 0.25 intersections/cell for Block A, and for Block B is 0.11 intersections/cell. In term of the spatial pattern, the lineament length map looks similar to the lineament frequency map, where the high lineament length coincides with the location with high lineament frequency. Also, the locations with low lineament length index also correspond with the low lineament frequency. Surprisingly, some interesting pattern is given by the lineament intersection map where the majority of points with high lineament intersection align with the regional structures. Fig 5.7 (C) shows an interpretation of the alignments of the high lineament intersections for Block A and Block B. From this figure, the high lineament intersections of Block A are oriented in N-S direction which corresponds to the extension of the Inielika volcanic complex. Meanwhile, for Block B, the orientations of the high lineament intersections are NW-SE and NE-SW which correspond with the regional structure in the study area.

In summary, the spatial pattern of the three lineament indices shows a good agreement with regional structures pattern that was identified from previous studies. Besides, they also indicate a correlation with the distribution of the geothermal temperature anomalies in the study area. Therefore, this relationship between lineament indices, regional structures, and the occurrence of geothermal anomalies have provided important information for interpreting the fluid pathway of the geothermal system in the study area. However, the value given by these three lineament indices is difficult to be related directly to the permeability of the structures because no data was available for comparison in this thesis.
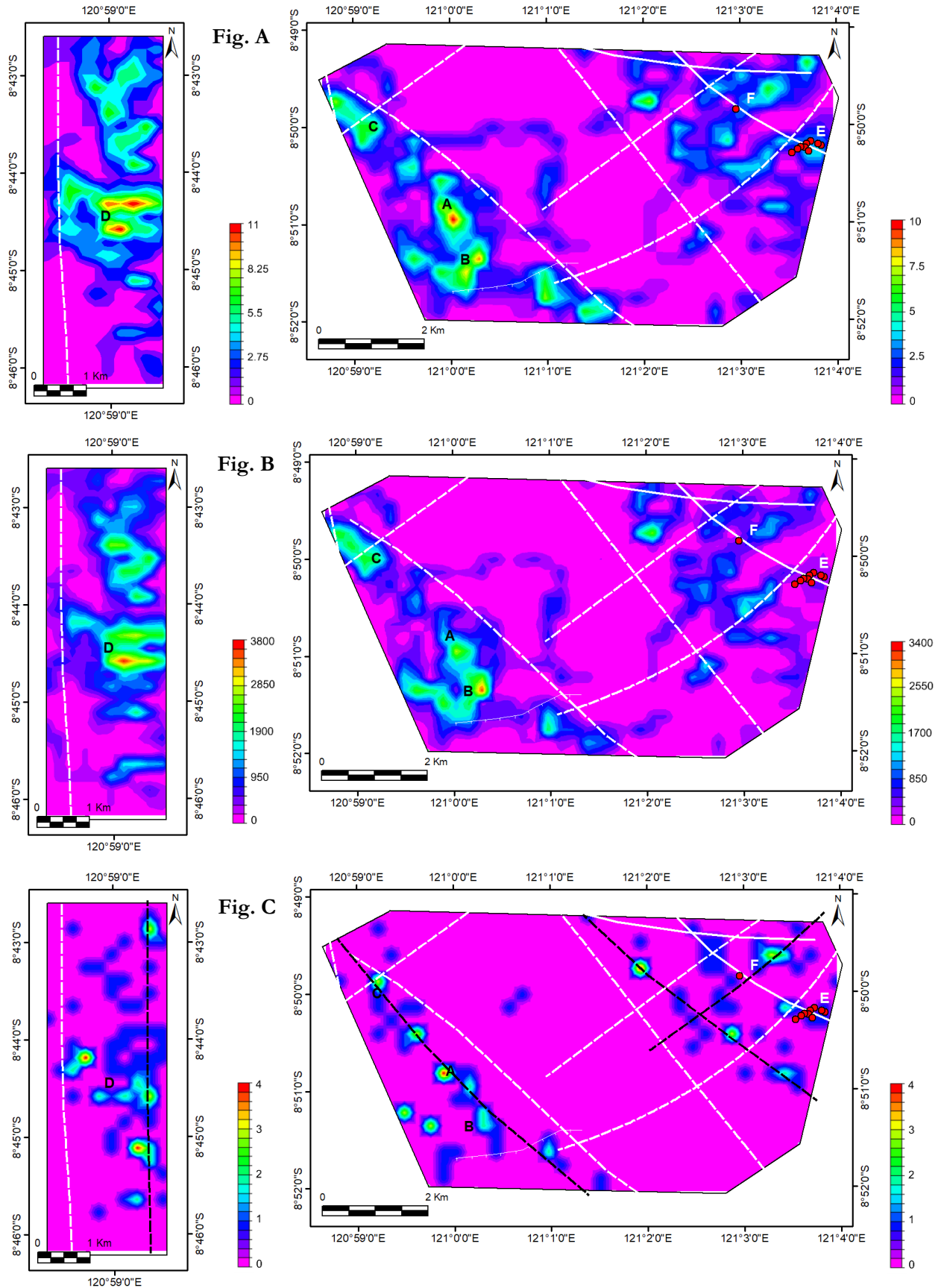
Figure 5.7 A) The lineament frequency map, B) lineament length map, and C) lineament intersections map for Block A (left) and Block B (right). These lineament indices were calculated in a grid with cell size of 250 x 250 m. The white solid lines indicate normal faults, white dashed-lines indicate regional magmatic lineaments, both interpreted by Akasako et al. (2002). The black dashed-lines in Figure C show the interpreted alignment of the high lineament intersection points. The red dots represent the confirmed geothermal temperature anomalies location that was described in Section 4.3.4. The pattern of the Figure A and B is similar, meanwhile the Figure C show relatively different pattern.

6.   INTEGRATED INTERPRETATION OF SURFACE AND SUBSURFACE ANOMALIES PATTERN

In this chapter, the findings from Chapter 4 and 5 are integrated with the subsurface data to investigate whether the airborne data give valuable information to predict the subsurface geothermal features. The focus of this chapter is to evaluate the relationship between geothermal indicators at the surface (temperature anomalies and structures) with the geological, geophysical, and geochemical data in Mataloko Geothermal Field (MGF) as one of the prospect locations that was identified in the previous chapters.

As shown in Fig 6.1, the multiple layers containing airborne data, geological map, and geophysical data were stacked to show the surface and subsurface anomalies in MGF. The first layer shows the topography of MGF derived from LiDAR DEM. The second layer represents the geological map that was digitized from Nasution et al. (2000) and the extracted lineaments as the result of Chapter 5. Layer 3 shows the lineament density map as the outcomes of Chapter 5. Layer 4 shows the iso apparent resistivity map derived from 2-D inversion of direct Schlumberger-resistivity data. Layer 5 shows the residual magnetic anomaly derived from the magnetic survey at MGF. The last layer shows the 2nd order residual gravity anomaly derived after free air, terrain and Bouguer correction. The layer 4-6 were digitized from the original maps in Dwipa et al. (2001).

From Fig 6.1 the surrounding area of MGF is covered by Mataloko Andesite (Qvma) formation which is characterized by a thin surface layer with high-resistivity that indicate less-altered volcanic deposits, except at the geothermal manifestation zone where the volcanic rocks mainly were altered into the argillic and advanced argillic alteration minerals such as kaolinite, montmorillonite, and alunite (Nasution et al., 2000). The Qvma unit is surrounded by the younger volcanic unit (Qvc) that is consisted of monogenetic volcanoes (see Layer 1 in Fig 6.1). As stated in Muraoka et al. (2005) the magmatic source of the Qvc formation was presumed to be the heat source of the MGF. However, from the existing geophysical data, the specific location of a geothermal heat source is not clearly shown.

As described in the results of Chapter 4, the MGF is comprised of geothermal manifestations including fumaroles, hot springs, mud pools, and steaming grounds with the temperature varies between 35-95°C. These manifestations are oriented mainly in two directions including NE-SW and NW-SE trends (Fig 6.2). The NW-SE trend aligns with the extension of the low resistivity zone (<10 Ωm) as shown by the Layer 4 of Fig 6.1. This zone also coincides with the negative magnetic residual anomaly (-400 nTesla) which reflects the presence of demagnetized volcanic rocks due to hydrothermal alteration. Yasukawa et al. (2002) and Munandar et al. (2002) associated this NW-SE trend with the Wae Luja fault based on their findings of a high permeability zone derived from the numerical modeling of self-potential data. Also based on the head-on apparent resistivity profile that shows a normal fault with NW-SE orientation and dipping 53° north. From these indications, the previous studies interpreted the Wae Luja fault as the primary pathway of geothermal fluids in MGF.

However, the extracted lineaments from the LiDAR DEM could not confirm an earlier proposed NW-SE Wae Luja fault, but rather found strong indication of NE-SW oriented structures in alignment with geothermal temperature anomalies and with the extension of the Hg anomaly of soil samples as reported in Akasako et al. (2002) (see Fig 6.2). Nevertheless, this NE-SW trend is not reflected in the existing geophysical data. But the drilling report in MT-1 and MT-2 shows the Total Lost Circulation (TLC) and Partial Lost Circulation (PLC) at the 13.8 m, 98.3 m, and 103.23 m below the surface which indicates the presence of shallow structures just below the main manifestation area (Nanlohy et al., 2002). Hence, we

interpret that this NE-SW trend corresponds to the shallow structures that control the secondary pathway of geothermal fluids in MGF.
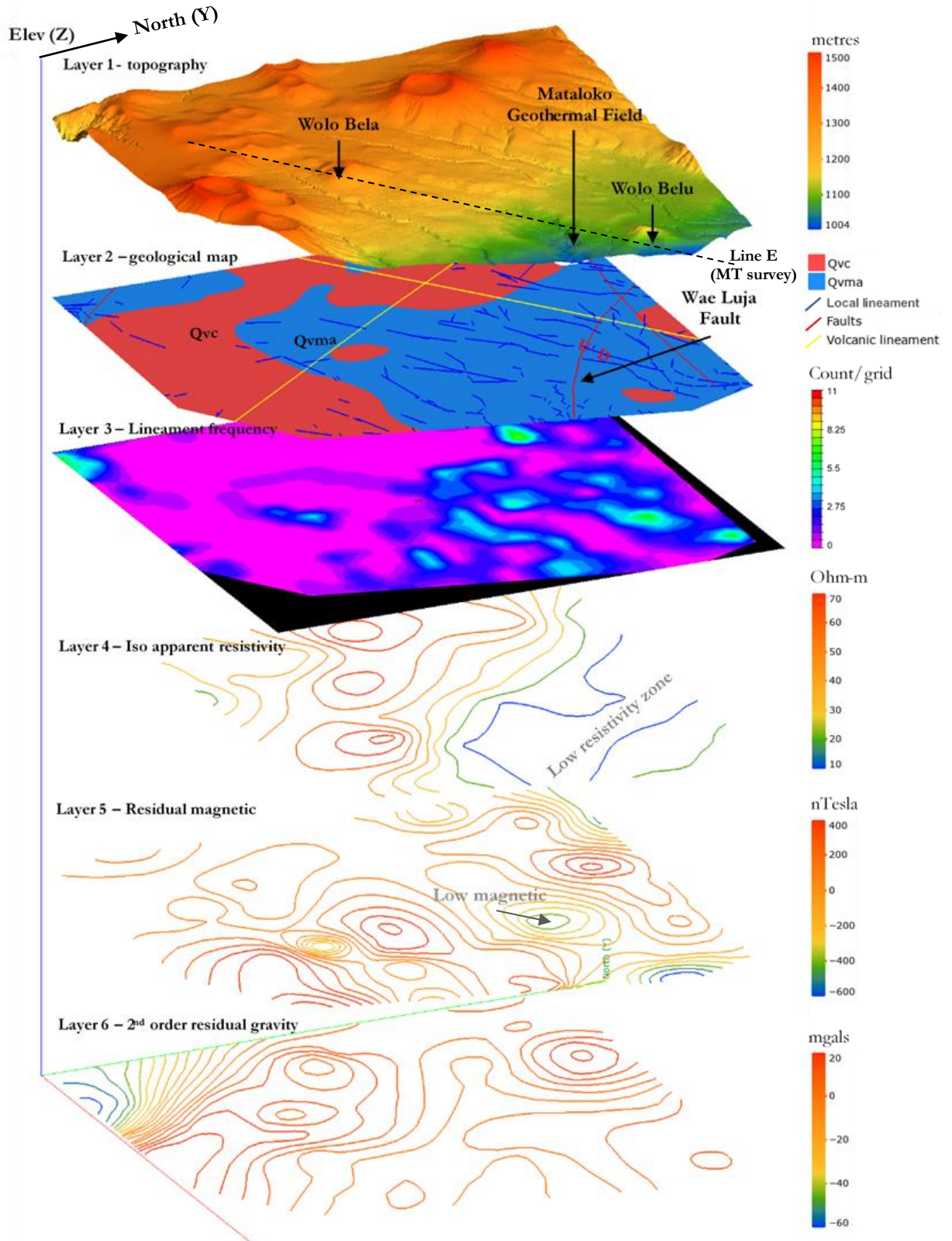
Figure 6.1 Multilayer of the surface and subsurface data of Mataloko Geothermal Field (MGF) collected from the previous chapters and from literatures. The 3-D topography (layer 1) shows the monogenetic volcanoes surrounding the MGF. This area is mainly controlled by the normal fault Wae Luja with NW-SE trend which is aligned with the low resistivity zone (layer 4) and the low magnetic anomaly (layer 5). As shown in layer 3, the MGF area is surrounded by the moderate lineament frequency zones that have trend in NE-SW which is suggested as the shallow structures controlling the recharge of meteoric water as well as up-flow zone of the geothermal fluid in MGF.
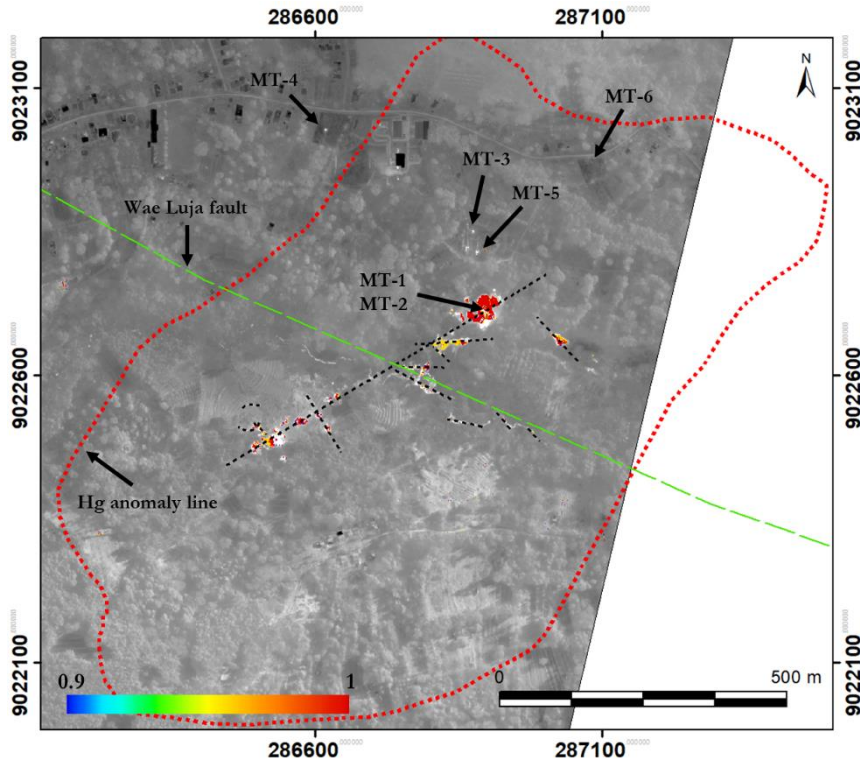
Figure 6.2 Geothermal temperature anomalies in Mataloko Geothermal Field (MGF) with NE-SW trend aligns with the extension of Hg anomaly (red dashed line) reported by Akasako et al. (2002). The MT-1 until MT-6 are the exploration wells that were drilled in two phases between 2000 until 2006.
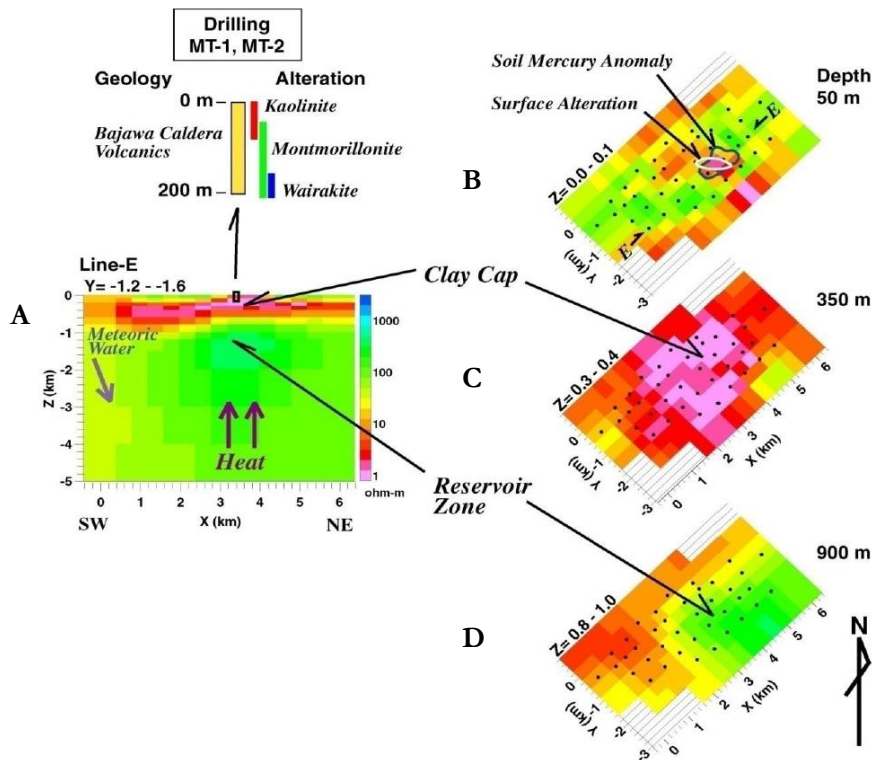
Figure 6.3 A) 2-D inversion model of magnetotelluric data in Mataloko Geothermal Field (MGF). B) This 2-D inversion indicates the geothermal system component of MGF including near surface geothermal anomalies, C) the low-resistivity (<10 Ωm) alteration caprock, and D) a very high-resistivity (>100 Ωm) reservoir layer. The maps on the right side (A, B, and C) are derived from 3-D inversion of resistivity data. The drilling data for well MT-1 and MT-2 are shown in the upper-left figure which indicates the extension of alteration minerals at the subsurface including kaolinite, montmorillonite, and wairakite. Source: Uchida et al. (2002).

According to Uchida et al. (2002), there are very low resistivity zone below the geothermal surface manifestations observed in the 2D and 3D inversion of magnetotelluric data. This zone extends until 400-500 meters below the surface with the horizontal extension approximately 2 km at 250 meters depth. This zone is interpreted as the alteration cap rock of the MGF (see Fig 6.3.C). The 3-D inversion of the MT data reveals a reservoir zone located deeper than 900 meters below the surface that is characterized by a high resistivity value (Fig 6.3.D). According to Nasution et al. (2000), the high ratio of CO_2/H_2S and H_2S/SO_2 of the fumarolic gas samples in MGF indicates that the temperature of the geothermal reservoir is around 283°C. Also, the present of wairakite mineral in the cutting samples of drilling well MT-1 and MT-2 at depth ~200 meters also indicates the very hot fluid circulation (between 220-300°C) in the geothermal reservoir.

We interpret the recharge area is located at the surrounding of monogenetic volcanoes near the MGF such as Wolo Nawa, Wolo Bela, and Wolo Belu. These areas are characterized by the moderate lineament frequency (3–6 lineaments/cell) indicating the occurrence of minor faults or fractures that enhance the secondary permeability of the volcanic rocks. The meteoric waters infiltrate the volcanic rocks through the faults or fractures and then circulate at the geothermal reservoir. We infer that the geothermal fluids elevate through the Wae Luja fault as the primary pathway and then some of them are transferred to the NE-SW oriented structures as the secondary pathway (see Fig 6.4). The hot fluids condense at the shallow depth and then formed geothermal manifestations including fumaroles, hot-springs, and mud-pools. Some of the heat is transferred through the conductive rocks into the surface as the steaming grounds.
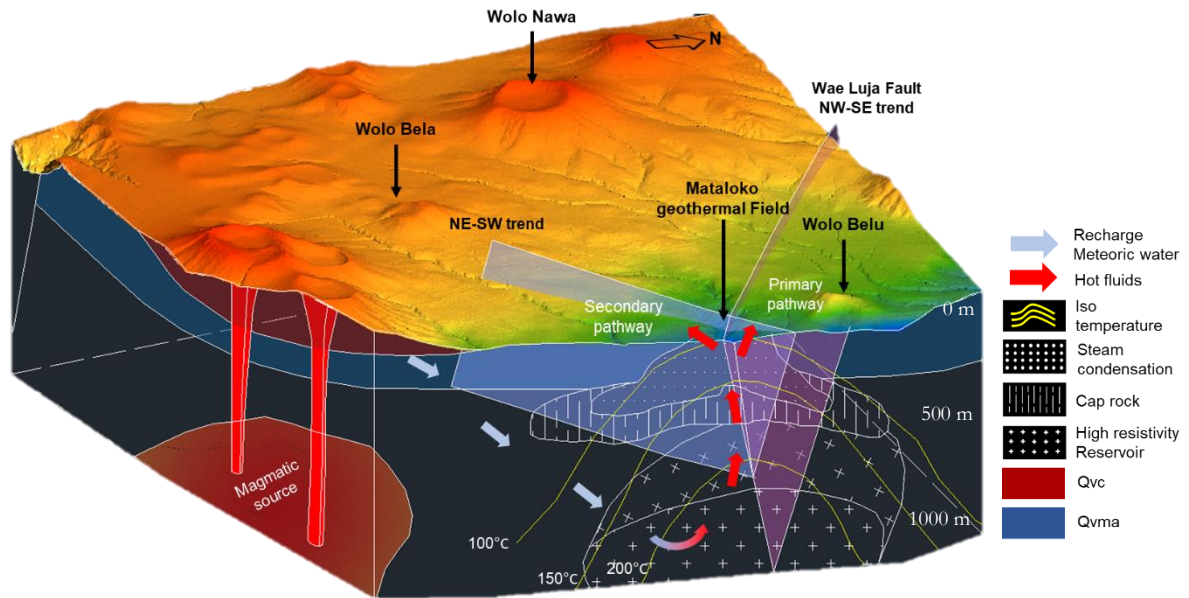
Figure 6.4 Conceptual model of the geothermal system in Mataloko Geothermal Field. The recharge zones are located at the monogenetic volcanoes surrounding the MGF such as Wolo Bela, Wolo Belu, Wolo Nawa. The meteoric waters infiltrate the volcanic rocks, then are circulated at the geothermal reservoir. The hot fluids are elevated through Wae Luja Fault as the primary pathway, and some of them are transferred through the NE-SW structure as the secondary pathway. These hot fluids are condensed near the surface and formed geothermal manifestations including hot springs, mud pools, steaming grounds, and fumaroles. The vertical scale of this model is an approximation.

7. DISCUSSION

7.1. Airborne TIR orthoimages generation

Table 3.3 and Table 3.4 indicates that the interior camera parameters significantly determine the total number of calibrated images in the first step of IBM. We observed that when an image was not automatically calibrated, the 3-D sparse points were not extracted for the corresponding image. Consequently, some gaps occurred in the 3-D sparse points structure. Although it is fixable by collecting as many tie points as possible manually (often more than 8 tie points are required for manual calibration), but this process is time-consuming and less precise because the thermal images have little contrast which makes the manual identification of the corresponding points between images difficult. We experienced that the manual calibration of a thermal image took approximately 5 to 7 minutes. If the automatic calibration rates are only 90%, it means that we need to calibrate at least 800 thermal images manually (from more than 8000 images in total). In that case, the IBM workflow will not be practical for producing an orthoimage from the large number of airborne TIR images.

In this study, we solved the uncalibrated image problem by carrying out internal camera parameter optimizations of the two training areas then used the optimized parameters that yielded 100% rates of the automatic image calibration. From the three iterations, we found a significant difference between the optimized camera parameters as compared to the default parameters for the FLIR x6570sc camera. The biggest discrepancy is given by the intrinsic principal point X and Y, where the maximum difference is about 0.25 mm in X and Y directions (Table 3.3 and 3.4). However, this discrepancy is somewhat expected as the characteristic of a thermal camera where the performance stability and repeatability are influenced by the ambient and device's temperature (Adamczyk & Sitnik, 2018). In this case, the long period of the image acquisition has potentially caused the variation of the ambient temperature and the increase of camera temperature that made some changes to the focal length and principal point of the FLIR camera. This phenomenon also explains the discrepancy of the optimized interior parameter of Block A and Block B which were acquired on different days.

The initial processing of the IBM workflow has resulted in an overall 97% calibrated images for Block A and Block B. The other 3% of thermal images were not calibrated automatically. Consequently, some gaps occurred in the 3-D sparse point structures. This problem occurred due to several reasons that related to the exterior flight parameters such as lack of side overlaps, an abrupt change of topography, and change of altitude of the aircraft. These problems were difficult to solve, especially in areas near the Block edges where the aircraft was turning around (see location 2 in Fig 3.6) and at the part that has high topographic relief (see location 1 in Fig 3.6).

Some unexpected errors occurred in the middle of Block B (see location 3 and 4 in Fig 3.6). In this location, the thermal images have been automatically calibrated, but the orientation of some images in the single flight line was tilted (off-nadir) therefore the 3-D sparse points structure in this location was dislocated and produced a rectangular gap. For this unexpected problem, the two technical solutions were implemented by collecting manual tie points to re-calibrate the dislocated images and then re-optimize the 3-D sparse point structure. Secondly, when the first solution was not successful, we created a smaller (sub-)project that covered the location of the unexpected error, then the resulted 3-D sparse points were patched to the bigger block project. Although this merging likely resulted in a geometric misfit between the two projects, this option is helpful to fill the gaps of the unexpected error as well as preserves the airborne TIR information in this particular area.

A high horizontal error (> 5 meters) in Block A (see Fig 3.5) is attributed mainly to the inconsistency (high standard deviation) of flying altitude and surface elevation as shown in Table 3.2. Consequently, there was a significant number of images (~15%) in Block A has a different scale compared to the neighboring lines due to an abrupt change of flying height. This scale inconsistency caused the feature detection and matching algorithm in Pix4D mapper works less reliably. Hence, the image orientation tends to be inaccurate. Moreover, the high topographic area in Block A mostly covered by the dense forest. This landcover type produced fewer automated tie points due to its relatively less texture and a homogenous pattern in the thermal images. This problem might emanate a geometric distortion in the 3-D sparse point structure as well as in the final orthoimage products.

The difference of multi-beam signal characteristic of LiDAR and FLIR sensors is considered to explain the variation of the DoD. The response signal for these sensors works differently, where the LiDAR signal have deeper penetration and could receive multi returns signal for the object like vegetation. Meanwhile, the FLIR camera always captures the emitted signal from the top of objects for all land cover types. In the analysis, we observed an unexpected result (see Fig 3.9) where the building and ground have a different average and standard deviation DoD statistics (supposedly similar in an ideal condition). Here, the building class has a low standard deviation. Meanwhile, the ground shows a high standard deviation (we expected a lower value). A possible explanation for this difference might be that the bare grounds cover high relief topographies with big elevation difference like hilly terrain and valleys which makes the 3-D sparse point reconstruction from thermal images inaccurate. Consequently, the standard deviation of DoD for the ground class is higher, which is what we observe in Block A. Meanwhile, Block B with relatively low topographic relief has a smaller standard deviation DoD for the ground class.

With the output of sub-meter GSD, the overall horizontal accuracy of 4 – 8 meters, and the average vertical error of 1 – 5 meters, the airborne TIR orthoimage products is considered sufficiently accurate for geothermal temperature anomalies mapping. Although the absolute horizontal accuracy is relatively low (more than 10 pixels), this problem is fixable by using *rubber sheeting* technique since the horizontal error is mostly systematic. Therefore, the integration of airborne TIR orthoimage with the other datasets is possible to be conducted for the investigation of the geothermal anomalies. Moreover, the vertical accuracy is less critical for this study because analysis of the airborne TIR orthoimage was carried out in 2-D mapping. Besides, the DSM that was derived from airborne TIR data using the IBM workflow is not the primary target since the LiDAR DSM with higher accuracy is available.

In the technical point of view, the orthoimage production using the IBM approach was very efficient in term of processing time. In this thesis, for a typical thermal image used per block with the total number of 2,000 - 6,000 images (at 640 x 512 pixels resolution), using a 64-bit window system on a 3.10 GHz CPU, 49 GB RAM, the total processing time ranging from 12 – 36 hours. The time cost given by the IBM workflow is more efficient compared to the traditional photogrammetric approach that possibly requires several weeks to process the same number of images. Besides, the lack of ground control points (GCP) makes the traditional photogrammetric workflow very challenging. Hence, the used of the IBM approach is inevitable for future application.

However, we remind that the thermal camera (FLIR x6570sc) is not made for airborne applications. Unlike a commercial Thermal Airborne Broadband Imager (TABI) which is conceived to be on an aircraft and well-synchronized with GNSS/IMU system, FLIR x6570sc camera is less reliable as compared to TABI because it is not calibrated for an airborne environment, also because its internal delay (time to open the shutter) with the GNSS/IMU system was not modeled (F. Nex, personal communication,

January 10, 2019). Hence, the airborne TIR orthoimage products derived from the FLIR camera might be less accurate for the domain of photogrammetry, but still sufficient for geothermal anomaly mapping.

7.2.   Geothermal temperature anomalies detection using airborne TIR images

The results from Chapter 5 show that the airborne TIR orthoimages with GSD of sub-meter are able to present the pattern of geothermal anomalies in the study area, while the previous studies using the spaceborne TIR image failed to detect these features (Hecker et al., 2017; Urai et al., 2002). However, there is an unexpected problem where the temperature given by the airborne TIR data underestimated the actual temperature of geothermal anomalies that was measured using Fluke IR thermometer. Fig 4.9 indicates that the linear regression between airborne-based and ground-based temperature has a considerably high intercept of 43 – 49°C for Preset 0, Preset 1, and Preset 2. The all preset seems to be saturated at the range between 45 – 50°C. This finding is different to the calibration range shown in Table 3.1 where the Preset 0 has maximum sensitivity at 30.6°C, Preset 1 at 63.2°C, and Preset 2 at 150°C. If the problem was occurred due to different calibration characteristic, we expected that the hotspots temperature given by the three presets should not be similar, but here they show relatively same temperature ranges.

The explanation of this problem could be addressed to the internal and external variables during the data acquisition. The internal source is respected to the difference field-of-view (FOV) and the ground sampling distance (GSD) between Fluke IR thermometer with the FLIR camera. While the Fluke IR measures the object with the diameter FOV of 1-2 cm, the FLIR orthoimages represent the surface temperature with GSD of 51 cm. When the field-based measurement captured the hottest point of the geothermal hotspots, the FLIR camera potentially captured a mixture of uneven hotspot's surface temperature (contain the high and intermediate temperatures) within a pixel. For example, according to Fig 4.9, the temperature difference between airborne-based and field-based measurement for the fumaroles is higher than the steaming grounds, which is because of the hottest part (outlets/holes) of the fumaroles often smaller than 10 cm, meanwhile the steaming grounds mostly extended more than 1 meters with relatively regular surface temperatures. This shows that the different temperature between airborne and field-based measurements depends on the size and type of geothermal manifestations.

Concerning the external variables, we interpret that the atmosphere might interfere with the temperature reading of the FLIR camera. Since the aircraft was flown at 750 – 1000 meters above the grounds, the tropospheric column below the aircraft with humidity above 80% (The World Weather Online, 2018) could interfere the emitted infrared signal from the surface. Hence, the radiance signal that received by the FLIR sensor contained only a fraction of the emitted signal from the earth surface, and the emitted signal from the atmosphere itself (at a much lower temperature). Consequently, the actual temperature of geothermal hotspots is underestimated by the airborne TIR images. Here, this external problem is not solved because it requires radiative transfer modeling, which goes beyond the scope of this research. In spite of that, the absolute temperature of the geothermal hotspots is not the main concern in this thesis, but the spatial pattern and spatial relationship with structures.

The results of Chapter 4 suggested that the DTC is effective in reducing false anomalies in the airborne TIR data. Particularly for the daytime acquisition with large variabilities given by the sun-illumination and different land cover types. The combination of albedo and hillshade variables in the DTC model is consistent with the simplified heat energy model described in Section 4.1.1. Besides, the used of DTF result as a variable in the DTC model has the advantage to transform the solar-heating dependent input (the airborne TIR orthoimages) into an independent input that does not contain a solar-heating effect anymore. Additionally, the land use images derived from LiDAR point clouds is effective to eliminate the

false anomalies associated with buildings and high vegetations. Based on the established DTC model, we suggest the optimal statistical thresholds to determine the true anomalies in the case study area are albedo > 0.134, hillshade < 0.244, the DTF value > 0.89, and the landcover type should be either bare grounds or low vegetations. The proposed DTC model might be reproducible for the application in the other geothermal fields. However, the optimal thresholds might be different in the other area depending on the type of geothermal manifestations, geographic and topographic settings

However, the current DTC model could not thoroughly remove the false anomalies that have similar characteristics with the geothermal anomalies for the specified variables (albedo, hillshade, DTF, and land-use). This limitation was encountered by the absence of the thermal inertia parameter in the DTC model since it was not available in this research. The current used hillshaded LiDAR DSM and albedo parameters could only compensate the effect of multi-directional sun illumination over the study area for the discrete time, instead of the integrated times as suggested by Coolbaugh et al. (2007). To model the integrated temperature variations of the different surface materials during the images acquisition requires the thermal inertia which determines the capacity and rates of heating and cooling of an object during the diurnal (24 hours) cycle. Hence, by including the thermal inertia we expected that the false anomalies with the same characteristic with geothermal anomalies (high albedo, low hillshade, and high DTF value) could be discriminated and fully removed.

7.3.   Structural analysis using airborne LiDAR DEM

The modified MHHC method (including LINE module) described in Chapter 5 has been able to map the detailed lineaments from LiDAR DEM in an automatic way. However, we noticed that the parameter settings in the LINE module have a significant effect on the extracted lineaments in term of the length and the pattern (see Fig 5.3). Through some iterations and tweaking parameters, we found that the most sensitive parameter in the LINE module is LTHR which represents the threshold value for curve length. The small LTHR value (<50 pixels) resulted in many noises since the unwanted features like agriculture fields and buildings were dominant. Therefore, the higher value was required to avoid noises, but by using too high value the detailed lineaments likely to be ignored. Here, we used 200 pixels (correspond to 100 meters) as an optimal value because it reduced the unwanted features significantly but also kept the detailed lineaments. The parameters shown in Fig 5.1 were found to be the optimal parameters for detecting detailed lineaments using LiDAR DEM with GSD of 0.5 meters.

The result given in Fig 5.5 shows the main lineaments direction of Block B correlates with *en échelon* structures that marked out the main regional structure of Flores Island with orientation NE-SW. This orientation also aligns with one of the magmatic lineament in Bajawa area as interpreted by Akasako et al. (2002) based on the alignment of monogenetic volcanoes in NE-SW directions. On the other hand, the extracted lineaments in Block A (Fig 5.5) with the main orientation E-W do not correlate with any regional structures pattern in Flores Island. This E-W pattern has a perpendicular direction to the clustered monogenetic volcanoes that are extending in the north-south direction. Hence, we infer that these lineaments are dominantly controlled by the volcanic morphology of the Inielika volcanic complex rather than the tectonic structures.

From the lineament density indices, some of the areas with moderate lineament frequency (3 – 6 counts/cell) might correlate with the highly-fractured zones where the geothermal fluids elevated. This zone coincides with the location of geothermal temperature anomalies that were identified in Chapter 4 (see location E and F in Fig 5.7). On the other hand, at locations A, B, C, and D with high lineament density, no link to surface anomalies could be established. Therefore, the interpretation of lineament density should be taken with caution because the high-density lineaments do not always relate with the up-flow or outflow zone of a geothermal system.

Based on the integrated interpretation in Chapter 6, we find that the occurrence of geothermal manifestations and structures at the surface is relevant as an indicator for geothermal fluid circulation at the subsurface. However, the main pattern of the surface features is different from what we observed in the subsurface data, where the surface features show the main NE-SW trend, meanwhile the subsurface trend is NW-SE. A possible explanation for this difference might be that the NW-SE trend associated with relatively deep structures that are covered by the younger volcanic products of the monogenetic volcanoes surrounding the geothermal prospect location (MGF). Hence, the detailed lineaments derived from LiDAR DEM could not identify these structures.

With this difference, it does not necessarily mean no link could be established between surface indicators provided by the airborne data with the subsurface features. Instead, we emphasize this difference as additional information to reveal something that is still missing and unreported in the previous studies that mostly focused on finding the main structures for the drilling target. Here, based on the findings of the NE-SW trend in the airborne TIR and LiDAR data but does not appear in the subsurface data, we suggest this structure is a secondary pathway that controls the geothermal fluids circulation at a shallow depth in Mataloko Geothermal Field (MGF). This structure might be an addition to the Wae Luja Fault that has been interpreted as a primary pathway.

We conclude that the integration of the airborne TIR and LiDAR data provides promising information at the reconnaissance stage as well as for developmental stages. The combination of these two sensors has an advantage over the satellite-based remote sensing data that has limitation due to their low spatial resolution. However, a comprehensive interpretation of the geothermal system using airborne data is difficult without any information from 3-G data (geology, geophysical, and geochemical). We envisage that the integration between airborne remote sensing with 3-G data is a necessity for geothermal energy development in the future.

8. CONCLUSION AND RECOMMENDATION

8.1. Conclusion

In this research, the integration of airborne TIR and LiDAR data has been examined to investigate surface temperature anomalies and structures as predictors of the subsurface geothermal features in Bajawa area, Indonesia. Besides, the research also focused on answering technical problem related to the orthoimage production of the airborne TIR data using Image Based Modeling (IBM) workflow. Based on the results and discussion in the previous chapters, the following conclusion can be drawn to answer the research questions stated in Section 1.4:

1. What is the horizontal and vertical accuracy of the airborne TIR orthoimage product derived from IBM?

   The horizontal and vertical accuracy of the airborne TIR orthoimages is in the range between 3.9 – 7.6 meters and 1.2 – 4.5 meters, respectively, which is considered sufficient for geothermal anomaly mapping. The output Ground Sampling Distance (GSD) of the airborne TIR orthoimages in this dataset is between 0.4 – 0.5 meters, which is a very high resolution as compared to the spaceborne TIR data.

2. How significant is the influence of internal camera parameters and external parameters (terrain, flying height, side overlap, and land cover type) to the reliability of IBM on producing orthoimage from airborne TIR data?

   The internal and external camera parameters significantly influence the quality of the IBM products. The error in the orthoimages is attributed due to the variation of exterior parameter including side overlaps and flying height. More consistent flight parameter resulted in a better quality of the IBM outcomes. The landcover also influence the quality of IBM products, where the dense forest with relatively less texture and a homogeneous pattern is not ideal for the IBM workflow. The instability of the FLIR camera during the data acquisition is considered as a significant factor that causes a systematic error in the airborne TIR orthoimages. The automatic optimization of the internal camera parameters become a must in the IBM workflow to minimize the error.

3. What is the typical temperature and size of the surface temperature anomalies? Which types of geothermal manifestations are associated with these features?

   The geothermal temperature anomalies are mainly distributed in the Mataloko Geothermal Field (MGF). They associated with geothermal manifestation such as hot springs, fumaroles, mud pools, mud volcanoes, and steaming grounds with the actual temperature between 34-95°C. There is a significant discrepancy between airborne-based and ground-based temperature of the geothermal hotspots where the airborne TIR measurement underestimates the actual temperatures.

4. How to differentiate the geothermal temperature anomalies from non-geothermal (false) anomalies?

   The integrated use of the Dynamic Threshold Filter (DTF) and Decision Tree Classification (DTC) is able to automatically detect the geothermal temperature anomalies and filter the false anomalies with the level of accuracy of 87.9%. The geothermal anomalies in the study area are characterized by a relatively high albedo (> 0.134), low hillshade (< 0.244), and the DTF value > 0.89. The false anomalies mainly are associated with buildings and vegetations. Also, the bare

grounds and the low vegetations with hillshade > 0.244 and albedo < 0.134 also associated with the false anomalies.

5. What are the orientations and the density of the identified surface structures? How do they relate to the occurrence of geothermal temperature anomalies?

   The lineaments derived from the LiDAR DEM using the modified MHHC workflow show an apparent correlation with the regional NE-SW structures and the geothermal temperature anomalies pattern. Meanwhile, the E-W trend does not correlate with any regional structures but aligns with the drainage pattern of the Inielika volcanoes. The moderate lineament frequency, lineament length, and lineament intersection indices show a good agreement with the occurrence of geothermal temperature anomalies in MGF.

6. How do geothermal temperature anomalies and surface structures link with subsurface features? What additional information can be provided by this link to predict geothermal reservoir condition and fluid pathways in the subsurface of the research area?

   The interpretation of geothermal anomalies pattern identified from the airborne TIR images and the LiDAR DEM revealed additional information of the local and shallow structures (NE-SW orientation) in the MGF that does not show up in the subsurface data and was not reported in the previous studies. We suggest that these structures are the secondary pathway of the geothermal fluids up-flow in MGF as an addition to the Wae Luja Fault (NW-SE trend) that appear in the resistivity data and potentially acted as the primary pathway. The MT data shows an alteration caprock at a depth of 400-500 meters that is characterized by low resistivity (<10 Ωm), and a geothermal reservoir at depth >900 meters that are characterized by high resistivity (>100 Ωm). The water, gas, and mineral geochemistry indicate the high-temperature reservoir (~283°C) beneath the MGF.

8.2. Recommendation

This research encountered challenges and some new problems that still unsolved and potential as the directions for future research. The following recommendations are the outlook to improve and to develop this research in the future:

1. Consider the high discrepancy between the geothermal temperature anomalies measured at the field with the airborne TIR orthoimages. Some modeling could be conducted to understand the reason and solve the problem, such as:
   - Radiative transfer modeling is expected to improve the radiometric accuracy of the airborne TIR images. Currently, the atmospheric correction method is still limited to a specific FLIR sensor. A collaboration with the meteorological agency may be helpful to obtain the atmospheric parameters in the study area.
   - Resampling airborne TIR images into some different spatial resolutions and analyze the effect of pixel size to the temperature of geothermal anomalies. This analysis could answer the research question about the correlation between geothermal types and sizes to the temperature given by airborne TIR images.

2. The nighttime acquisition is highly recommended for a future project to minimize the false positive issue. Besides, some additional instruments are highly recommended to be installed in the aircraft such as a multispectral sensor that can be used to derived thermal inertia and emissivity of the surface. These physical surface parameters could be used to thoroughly filters the false anomalies using the DTC model for future work.

3. After the radiometric correction, the quantification of geothermal heat flux from airborne TIR orthoimages temperature could be valuable information to calculate the total heat loss of geothermal energy.

4. The use of a specialize airborne thermal infrared sensor like TABI might provide a better geometric and radiometric accuracy than the current used FLIR x6570sc camera. Additionally, some Ground control points (GCPs) is highly recommended to be taken during the data acquisition for the image orientation and external quality assessment of Image-Based Modeling (IBM) products.

LIST OF REFERENCES

Abdullah, A., Akhir, J. M., & Abdullah, I. (2010). Automatic Mapping of Lineaments Using Shaded Relief Images Derived from Digital Elevation Model (DEMs) in the Maran – Sungi Lembing Area. *EJGE*, *15*, 949–957.

Adamczyk, M., & Sitnik, R. (2018). Temperature Compensation Method for Digital Cameras in 2D and 3D Measurement Applications. *MDPI - Sensors*. https://doi.org/10.3390/s18003685

Akasako, H., Matsuda, K., Tagomori, K., Koseki, T., Takahashi, H., & Dwipa, S. (2002). Conceptual models for geothermal system in the Wolo Bobo, Nage and Mataloko fields, Bajawa area, Central Flores, Indonesia. *Bulletin of the Geological Survey of Japan*, *53*, 375–387.

Aldrich, C., & Auret, L. (2013). Tree-Based Methods. In *Unsupervised Process Monitoring and Fault Diagnosis with Machine Learning Methods* (pp. 183–220). London: Springer London. https://doi.org/10.1007/978-1-4471-5185-2_5

Cagatay, G. (2015). Global Geothermal Alliance launches in Paris COP21. Retrieved July 31, 2018, from https://www.aa.com.tr/en/energy/renewable/global-geothermal-alliance-launches-in-paris-cop21/8107

Coolbaugh, M. F., Kratt, C., Fallacaro, A., Calvin, W. M., & Taranik, J. V. (2007). Detection of geothermal anomalies using Advanced Spaceborne Thermal Emission and Reflection Radiometer (ASTER) thermal infrared images at Bradys Hot Springs, Nevada, USA. *Remote Sensing of Environment*, *106*(3), 350–359. https://doi.org/10.1016/j.rse.2006.09.001

Curewitz, D., & Karson, J. A. (1997). Structural settings of hydrothermal outflow: Fracture permeability maintained by fault propagation and interaction. *Journal of Volcanology and Geothermal Research*, *79*(3–4), 149–168. https://doi.org/10.1016/S0377-0273(97)00027-9

Dwipa, S., Uchida, T., Yasukawa, K., Honda, M., & Andan, A. (2001). Integrated Geophysical Exploration in Mataloko Geothermal Area , Central Flores - East Nusa Tenggara. *INAGA Annual Scientific Conference and Exhibition Yogyakarta, March 7 – 10, 2001*.

Eneva, M., & Coolbaugh, M. F. (2009). Importance of elevation and temperature inversions for the interpretation of thermal infrared satellite images used in geothermal exploration. *GRC Transactions*, *33*, 467–470.

ESRI. (2016a). Help page - How Hillshade works. Retrieved December 26, 2018, from http://desktop.arcgis.com/en/arcmap/10.3/tools/spatial-analyst-toolbox/how-hillshade-works.htm

ESRI. (2016b). Help page - Spatial adjustment rubbersheeting. Retrieved January 2, 2019, from http://desktop.arcgis.com/en/arcmap/10.3/manage-data/editing-existing-features/about-spatial-adjustment-rubbersheeting.htm

ESRI. (2018a). Help page - Grouping Analysis. Retrieved December 20, 2018, from http://pro.arcgis.com/en/pro-app/tool-reference/spatial-statistics/grouping-analysis.htm

ESRI. (2018b). Help page - How Linear Directional Mean works. Retrieved December 20, 2018, from http://pro.arcgis.com/en/pro-app/tool-reference/spatial-statistics/h-how-linear-directional-mean-spatial-statistics-w.htm

Fitton, N. C., & Cox, S. J. D. (1998). Optimising the application of the Hough transform for automatic feature extraction from geoscientific images. *Computers & Geosciences*, *24*(10), 933–951. https://doi.org/https://doi.org/10.1016/S0098-3004(98)00070-3

Förstner, W. (1998). On the Theoretical Accuracy of Multi Image Matching, Restoration and Triangulation. *Institut Für Photogrammetrie, Universitat Hannover*, (227), 105–118.

Gutiérrez, F. J., Lemus, M., Parada, M. A., Benavente, O. M., & Aguilera, F. A. (2012). Contribution of ground surface altitude difference to thermal anomaly detection using satellite images: Application to volcanic/geothermal complexes in the Andes of Central Chile. *Journal of Volcanology and Geothermal Research*, *237–238*, 69–80. https://doi.org/10.1016/j.jvolgeores.2012.05.016

Han, L., Liu, Z., Ning, Y., & Zhao, Z. (2018). Extraction and analysis of geological lineaments combining a DEM and remote sensing images from the northern Baoji loess area. *Advances in Space Research*. https://doi.org/10.1016/j.asr.2018.07.030

Harvey, M. C., & Luketina, K. (2014). Thermal Infrared Cameras and Drones: a Match Made in Heaven for Cost- Effective Geothermal Exploration, Monitoring and Development. In *New Zealand Geothermal Workshop 2014 Proceedings* (pp. 1–4).

Harvey, M. C., Rowland, J. . ., & Luketina, K. M. (2016). Drone with thermal infrared camera provides

high resolution georeferenced imagery of the Waikite geothermal area , New Zealand. *Journal of Volcanology and Geothermal Research*, *325*, 61–69. https://doi.org/10.1016/j.jvolgeores.2016.06.014

Haselwimmer, C., & Prakash, A. (2013). Thermal Infrared Remote Sensing of Geothermal Systems. In *Thermal Infrared Remote Sensing Sensors, Methods, Applications* (Vol. 17, pp. 453–473). Dordrecht: Springer. https://doi.org/10.1007/978-94-007-6639-6

Haselwimmer, C., Prakash, A., & Holdmann, G. (2013). Quantifying the heat flux and outflow rate of hot springs using airborne thermal imagery: Case study from Pilgrim Hot Springs, Alaska. *Remote Sensing of Environment*, *136*, 37–46. https://doi.org/10.1016/j.rse.2013.04.008

Hecker, C., Hewson, R., Setianto, A., Saepuloh, A., & van der Meer, F. D. (2017). Multi-source remote sensing data analysis for geothermal targeting on Flores island. *Proceedings The 5th Indonesia International Geothermal Convention & Exhibition (IIGCE) 2017*, 1–7.

Hodder, D. T. (1970). Application of remote sensing to geothermal prospecting. *Geothermics*, *2*(Part 1). https://doi.org/10.1016/0375-6505(70)90035-0

Hoffmann, T. (2018). Sun position for the Bajawa area. Retrieved November 30, 2018, from https://www.suncalc.org/#/-8.7874,120.9733,16/2018.05.26/14:34/1/3

Hothorn, T. (n.d.). ctree_control function | R Documentation. Retrieved December 30, 2018, from https://www.rdocumentation.org/packages/partykit/versions/1.2-3/topics/ctree_control

Houwers, M. E., Heijnen, L. J., Becker, A., & Rijkers, R. (2015). A Workflow for the Estimation of Fault Zone Permeability for Geothermal Production A General Model Applied on the Roer Valley Graben in the Netherlands. *Proceedings World Geothermal Congress 2015*, (April), 9.

International Finance Corporation. (2013). *Success of geothermal wells: A global study. International Finance Corporation - World Bank Group.* https://doi.org/10.1016/S0185-0849(15)30010-4

ITACA. (n.d.). Calculating Solar Angles. Retrieved December 26, 2018, from https://www.itacanet.org/the-sun-as-a-source-of-energy/part-3-calculating-solar-angles/

Jaworowski, C., Heasler, H. P., Neale, C. M. U., & Sivarajan, S. (2010). Using thermal infrared imagery and LiDAR in Yellowstone geyser basins. *Yellowstone Science*, *18*(1), 8–19.

Koike, K., Nagano, S., & Ohmi, M. (1995). Lineament analysis of satellite images using a Segment Tracing Algorithm (STA). *Computers & Geosciences*, *21*(9), 1091–1104. https://doi.org/https://doi.org/10.1016/0098-3004(95)00042-7

Kuenzer, C., Hecker, C., Zhang, J., Wessling, S., & Wagner, W. (2008). The potential of multidiurnal MODIS thermal band data for coal fire detection. *International Journal of Remote Sensing*, *29*(3), 923–944. https://doi.org/10.1080/01431160701352147

Mallast, U., Gloaguen, R., Geyer, S., Rodiger, T., & Siebert, C. (2011). Derivation of groundwater flow-paths based on semi-automatic extraction of lineaments from remote sensing data. *Hydrology and Earth System Sciences*, *15*, 2665–2678. https://doi.org/10.5194/hess-15-2665-2011

Masoud, A. A., & Koike, K. (2011). Auto-detection and integration of tectonically significant lineaments from SRTM DEM and remotely-sensed geophysical data. *ISPRS Journal of Photogrammetry and Remote Sensing*, *66*(6), 818–832. https://doi.org/10.1016/j.isprsjprs.2011.08.003

Meixner, J., Grimmer, J. C., Becker, A., Schill, E., & Kohl, T. (2017). Comparison of different digital elevation models and satellite imagery for lineament analysis: Implications for identification and spatial arrangement of fault zones in crystalline basement rocks of the southern Black Forest (Germany). *Journal of Structural Geology*, *108*(November 2017), 256–268. https://doi.org/10.1016/j.jsg.2017.11.006

Munandar, A., Andan, A., & Simanjuntak, J. (2002). Head-on measurement to locate the Wai Luja Fault in the Mataloko Geothermal field, Flores Island, East Nusa Tenggara, Indonesia. *Bulletin of the Geological Survey of Japan*, *53*, 247–251.

Muraoka, H., Nasution, A., Simanjuntak, J., Dwipa, S., Takahashi, M., & Takahashi, H. (2005). Geology and Geothermal Systems in the Bajawa Volcanic Rift Zone, Flores, Eastern Indonesia. *World Geothermal Congress 2005*, (April), 24–29.

Muraoka, H., Nasution, A., Urai, M., Takahashi, M., Takashima, I., Simanjuntak, J., … Koseki, T. (2002). Tectonic, volcanic and stratigraphic geology of the Bajawa geothermal field, central Flores, Indonesia. *Bulletin of the Geological Survey of Japan.*

Nanlohy, F., Kusnadi, D., & Sulaeman, B. (2001). Geology and Geochemistry of Mataloko Geothermal Field Central Flores – East Nusa Tenggara. *Proceeding of the 5th INAGA Annual Science Conference and Exhibitions.*

Nanlohy, F., Sitorus, K., Kasbani, Dwipa, S., & Simanjuntak, J. (2002). Subsurface geology of the Mataloko geothermal field deduced from MTL-1, MT-1 and MT-2 wells, central Flores, East Nusa

Tenggara, Indonesia. *Bulletin of the Geological Survey of Japan*, *53*, 329–336.

Nasution, A., Takashima, I., Muraoka, H., Takahashi, H., & Matsuda, K. (2000). the Geology and Geochemistry of Mataloko -Nage-Bobo Geothermal Areas , Central Flores , Indonesia. *Development*, (February), 2165–2170.

PCI Geomatics. (2018). LINE (Lineament extraction). Retrieved February 2, 2019, from http://www.pcigeomatics.com/geomatica-help/references/pciFunction_r/python/P_line.html

PT ASI Pudjiastuti Geosurvey. (2018). *Airborne LiDAR Survey for Geothermal Project: A Project Report*. Jakarta.

PT PLN Geothermal. (2010). *Laporan studi Geoscience lapangan panas bumi Mataloko, Kabupaten Ngada, Nusa Tenggara Timur*. Jakarta.

Richter, A. (2018a). Indonesia reaches 1,925 MW installed geothermal power generation capacity | Think GeoEnergy - Geothermal Energy News. Retrieved July 23, 2018, from http://www.thinkgeoenergy.com/indonesia-reaches-1925-mw-installed-geothermal-power-generation-capacity/

Richter, A. (2018b). PLN assigned three geothermal working areas of total up to 70 MW | Think GeoEnergy - Geothermal Energy News. Retrieved July 26, 2018, from http://www.thinkgeoenergy.com/pln-assigned-three-geothermal-working-areas-of-total-up-to-70-mw/

Saepuloh, A., Haeruddin, H., Heriawan, M. N., Kubo, T., Koike, K., & Malik, D. (2018). Application of lineament density extracted from dual orbit of synthetic aperture radar (SAR) images to detecting fluids paths in the Wayang Windu geothermal field (West Java, Indonesia). *Geothermics*, *72*(November 2017), 145–155. https://doi.org/10.1016/j.geothermics.2017.11.010

Scheiber, T., Fredin, O., Viola, G., Jarna, A., Gasser, D., & Łapińska-Viola, R. (2015). Manual extraction of bedrock lineaments from high-resolution LiDAR data: methodological bias and human perception. *Gff*, *137*(4), 362–372. https://doi.org/10.1080/11035897.2015.1085434

Šilhavy, J., Minár, J., Mentlík, P., & Sládek, J. (2016). A new artefacts resistant method for automatic lineament extraction using Multi-Hillshade Hierarchic Clustering (MHHC). *Computer and Geoscience*, *92*, 9–20. https://doi.org/10.1016/j.cageo.2016.03.015

Stober, I., & Bucher, K. (2013). *Geothermal energy: from theoritical models to exploration and development*. Heidelberg: Springer. https://doi.org/10.1007/978-3-642-13352-7

Szeliski, R. (2011). Structure From Motion. In *Computer Vision: Algorithms and Applications* (pp. 303–334). London: Springer, London. https://doi.org/10.1016/B978-0-12-236530-0.50012-1

Tagomori, K., Saito, H., Koseki, T., Takahashi, H., Dwipa, S., & Futagoishi, M. (2002). Geology and hydrothermal alterations, and those correlations to physical properties obtained from gravity and resistivity measurements in the Mataloko geothermal field. *Bulletin of the Geological Survey of Japan*, *53*, 365–374.

The World Bank. (2018). Geothermal Energy is on a Hot Path. Retrieved June 4, 2018, from http://www.worldbank.org/en/news/feature/2018/05/03/geothermal-energy-development-investment

The World Weather Online. (2018). Bajawa, East Nusa Tenggara, Indonesia Historical Weather Almanac. Retrieved February 5, 2019, from https://www.worldweatheronline.com/bajawa-weather-history/east-nusa-tenggara/id.aspx

Uchida, T., Lee, T. J., Honda, M., Ashari, & Andan, A. (2002). 2-D and 3-D interpretation of magnetotelluric data in the Bajawa geothermal field, central Flores, Indonesi. *Bulletin of the Geological Survey of Japan*, *53*(2/3), 265–283.

Urai, M., Muraoka, H., & Nasution, A. (2002). Satellite remote sensing data and their interpretation for geothermal applications: A case study on the Ngada District, Central Flores, Indonesia. *Bulletin of the Geological Survey of Japan*, *53*, 99–108.

Van der Meer, F., Hecker, C., van Ruitenbeek, F., van der Werff, H., de Wijkerslooth, C., & Wechsler, C. (2014). Geologic Remote Sensing for Geothermal Exploration: A Review. *International Journal of Applied Earth Observation and Geoinformation*, *33*(1), 255–269. https://doi.org/10.1016/j.jag.2014.05.007

Van Veen, A. (2017). *Preparing an Airborne Multi-Sensor Remote Sensing Survey on Flores , East Nusa-Tenggara , Indonesia*. Internship report, Enschede.

Varghese, J. (2016). *Detecting the Effect of Soil Moisture and Hot Spot Siza on Geothermal Anomalies via Remote sensing Technique*. MSc thesis - University of Twente. Retrieved from https://webapps.itc.utwente.nl/librarywww/papers_2016/msc/aes/varghese.pdf

Westoby, M. J., Brasington, J., Glasser, N. F., Hambrey, M. J., & Reynolds, J. M. (2012). "Structure-from-

Motion" photogrammetry: A low-cost, effective tool for geoscience applications. *Geomorphology*, *179*, 300–314. https://doi.org/10.1016/j.geomorph.2012.08.021

Yasukawa, K., Andan, A., Kusuma, D. S., Uchida, T., & Kikuchi, T. (2002). Self-potential mapping of the Mataloko and Nage geothermal fields, Central Flores, Indonesia for applications on reservoir modeling. *Bulletin of the Geological Survery of Japan*, *53*, 285–294.

Yilmaz, Ö., & Karakuş, F. (2016). Stereo and KinectFusion for continuous 3D reconstruction and visual odometry. *Turkish Journal of Electrical Engineering and Computer Sciences*, *24*(4), 2756–2770. https://doi.org/10.3906/elk-1401-273

Zhang, J. (2004). *Spatial and statistical analysis of thermal satellite imagery for extraction of coal fire related anomalies*. Phd thesis - Vienna University of Technology. https://doi.org/10.1007/s13398-014-0173-7.2

9. APPENDIXES

Appendix A – Instruction for using a Dynamic Histogram Stretching (DHS) in Pix4D

This appendix provides an instruction how to use a Dynamic Histogram Stretching (DHS) in Pix4D mapper. This DHS was designed to improves feature extraction and matching of thermal images by enhancing their contrast. Below is the detail instruction:

1. Create a new project in Pix4D
2. Load the input thermal images
3. Load the CSV file containing geolocation and orientation of thermal images
4. Setting the camera type and internal camera parameters
5. Choose advanced workflow for thermal images
6. Close the project
7. Open the .p4d file that located in the project directory using text editor
8. Below the <tangentialT2> and above the <cameraModelSource> lines, add the following code:
    <pixelValue pixelType="float32" min="-1" max="-1"/>
9. Re-open the project file using Pix4D mapper
10. Run the initial processing

More detailed information can be found in the Pix4D support: https://support.pix4d.com/hc/en-us/articles/360000173463-Processing-thermal-images#label8

Appendix B – Instruction for file transfer of the FLIR images using *command prompt*

This appendix explains the procedure of FLIR images transfer for each sub-block project. This code works in *command prompt* windows. It was written to allow importing multiple images selection in Pix4D software for each sub-block project. The procedure is described as follows:

1. Plot the FLIR images in ArcMap using their geolocation as a feature class (points)
2. Select the points according to the spatial extent of the sub-block project and open their attribute table
3. Copy the filename of the selected point (FLIR images) and paste them on a text editor
4. Open command prompt
5. Copy the code below for bulk copy of image files according to the list of header/filename

   for /f "delims=" %f in (Directory_X\"filename".txt) do (xcopy "Directory_Y\%f" "Directory_Z\")
   where,
   Directory_X   : The location of the txt file containing a list of filenames of the FLIR images
   Directory_Y   : The location of FLIR images
   Directory_Z   : The target location to put the copied FLIR images per sub-block

6. Run the command
7. Re-do step 2 to step 6 by modifying the list of filenames of FLIR images according to the sub-block project

Appendix C – R-programming scripts for Decision Tree Classification (DTC)

```
# input library that required to build DTC model
library(raster)
library(ggplot2)
library(caret)
library(party)
library(rpart)
library(rpart.plot)
library(partykit)

#Set working directory
setwd("C:\\Users\\dell\\Documents\\Education\\ITC\\Thesis\\Decision tree\\Input update\\")

#Load input variable images for training
Albedo<-raster("Input_All_B_Train.tif", band=2)
Relief<-raster("Input_All_B_Train.tif", band=3)
Land_cover<-raster("Input_All_B_Train.tif", band=6)
Filter<-raster("Input_All_B_Train.tif", band=7)
Training_feature<-raster("Training_Feature_B_Train2.tif")

#Make a dataframe from input variables
all<-stack(Albedo, Relief, Land_cover, Filter, Training_feature)
names(all)<- c(paste0("B",1:4, coll=""), "B5")
input<-data.frame(na.omit(values(all)))

#Convert the predictand into "class" data type
input$TrueFalse <- factor(input$B5)

#Convert the dataset into CSV file
write.csv(input, file="Training_DTC_4.csv", row.names=FALSE, na="")
img<-read.csv("Training_DTC_4.csv")
img$TrueFalse <- factor(img$TrueFalse)

#Build the training dataset and validation dataset with proportion of 70% and 30% respectively
set.seed(1234)
pd<-sample(2,nrow(img),replace=TRUE, prob=c(0.7,0.3))
train<-img[pd==1,]
validate<-img[pd==2,]

#Build decision tree model from training dataset
tree<-ctree(TrueFalse~B1+B2+B3+B4,data=train, control = ctree_control(mincriterion=0.95,minsplit=1000, maxdepth=4))
plot(tree)

#Produce a confusion matrix to validate the DTC model using the validation dataset
test<-predict(tree, validate)
confusionMatrix(test,validate$TrueFalse)
```

```
#Store and load decision tree model
saveRDS(tree,"DTC_4.rds")
load_tree<-readRDS("DTC_4.rds")


#Load test data for Block A
Albedo_A<-raster("Input_All_A.tif", band=2)
Relief_A<-raster("Input_All_A.tif", band=3)
Land_cover_A<-raster("Input_All_A.tif", band=6)
Filter_A<-raster("Input_All_A.tif", band=7)
img_A<-stack(Albedo_A,Relief_A,Land_cover_A,Filter_A)
names(img_A)<- c(paste0("B",1:3, coll=""), "B4")


#Load test data for Block B
Albedo_B<-raster("Input_All_B.tif", band=2)
Relief_B<-raster("Input_All_B.tif", band=3)
Land_cover_B<-raster("Input_All_B.tif", band=6)
Filter_B<-raster("Input_All_B.tif", band=7)
img_B<-stack(Albedo_B,Relief_B,Land_cover_B,Filter_B)
names(img_B)<- c(paste0("B",1:3, coll=""), "B4")


#Predict the probability of DTC model for the entire Block A and Block B, the output is tiff image
predict(img_A, load_tree, filename="A_Prob_DTC_4.tif", fun=predict, type="prob")
predict(img_B, load_tree, filename="B_Prob_DTC_4.tif", fun=predict, type="prob")
```

## Appendix D – Temperature measurement of the geothermal hotspots

This appendix provides detail information of the temperature measurement at field using Fluke IR thermometer and from the airborne TIR orthoimage preset 0, preset 1, and preset 2. Note that the airborne-based temperature here is the maximum temperature of each hotspot that were digitized in airborne TIR orthoimages. In total there are 77 measured hotspots in Mataloko Geothermal Field (MGF) and 1 measured hotspot in the river near Golewa village. Some measurement using glass mercury thermometer is given in some locations to calibrate the Fluke IR thermometer. The projection for the coordinate is UTM zone 51 south with datum WGS 1984.

ID	Coordinate		Location	Fluke IR (°C)	Mercury therm. (°C)	Airborne temp. (°C)			Size (m²)	Type
	X	Y				P0	P1	P2		
1	286896.6	9022712.2	Mataloko	75.4		45.0	57.9	56.6	93.4	Mud pool
2	286900.3	9022728.6	Mataloko	68.1		41.9	42.2	42.2	30.3	Fumaroles
3	286898.5	9022733.3	Mataloko	79.6		37.5	37.6	37.2	6.0	Fumaroles
4	286890.0	9022731.9	Mataloko	41.0		38.7	39.1	39.1	16.1	Steaming ground
5	286893.9	9022733.8	Mataloko	65.4		37.9	37.7	37.7	8.0	Steaming ground
6	286888.8	9022724.0	Mataloko	66.4		40.8	40.5	40.5	25.8	Steaming ground
7	286864.5	9022732.3	Mataloko	51.5		30.1	30.3	30.4	10.4	Mud pool
8	286855.3	9022723.6	Mataloko	51.2		34.9	33.8	34.2	5.6	Mud pool
9	286858.1	9022719.8	Mataloko	65.2		22.4	21.6	21.3	1.1	Mud pool
10	286853.7	9022707.4	Mataloko	81.9		25.9	26.0	25.6	3.1	Fumaroles
11	286845.7	9022707.5	Mataloko	47.7		26.2	26.0	25.9	5.8	Mud pool
12	286850.3	9022707.6	Mataloko	73.0		23.0	22.7	23.0	3.8	Fumaroles
13	286855.2	9022704.1	Mataloko	74.0		23.7	23.6	23.6	1.7	Fumaroles
14	286871.0	9022709.5	Mataloko	45.9		35.6	34.8	35.5	5.5	Steaming ground
15	286873.7	9022704.4	Mataloko	50.3		29.7	29.6	29.7	2.7	Steaming ground
16	286889.7	9022685.4	Mataloko	90.2		37.9	38.6	38.6	22.1	Fumaroles
17	286890.7	9022698.9	Mataloko	74.2		33.0	32.6	32.7	2.2	Mud pool
18	286898.9	9022693.3	Mataloko	83.0		29.3	29.3	29.1	1.4	Fumaroles
19	286903.3	9022694.6	Mataloko	91.2		33.5	33.4	33.7	4.4	Fumaroles
20	286892.5	9022707.6	Mataloko	42.5		32.6	32.8	32.8	1.9	Steaming ground
21	286882.7	9022704.3	Mataloko	91.3		31.2	30.0	30.9	0.5	Fumaroles
22	286881.5	9022701.3	Mataloko	95.3		35.0	35.1	35.1	6.0	Fumaroles
23	286900.7	9022688.0	Mataloko	89.9		32.9	32.3	32.7	6.5	Fumaroles
24	286899.2	9022703.2	Mataloko	68.8		30.9	31.5	31.4	2.0	Fumaroles
25	286895.2	9022705.4	Mataloko	70.0		30.7	31.9	32.4	1.4	Fumaroles
26	286884.2	9022708.3	Mataloko	58.0		30.4	30.2	30.4	2.3	Steaming ground
27	286888.6	9022707.9	Mataloko	88.6		30.4	28.7	28.7	0.7	Fumaroles
28	286887.7	9022714.1	Mataloko	63.4		35.1	35.9	36.2	3.5	Mud pool
29	286921.5	9022729.2	Mataloko	43.8		28.9	25.9	25.5	0.7	Steaming ground
30	286912.8	9022741.8	Mataloko	74.6		25.9	25.7	25.7	3.8	Fumaroles
31	286921.1	9022735.7	Mataloko	47.3		30.4	30.7	30.4	2.4	Fumaroles
32	286807.5	9022654.7	Mataloko	84.1		38.1	38.1	38.1	7.3	Fumaroles
33	287018.4	9022664.1	Mataloko	95.2		37.7	37.8	38.0	8.1	Fumaroles
34	287019.3	9022668.7	Mataloko	92.4		43.5	45.6	45.0	40.4	Fumaroles
35	287032.8	9022662.5	Mataloko	92.7		32.6	32.9	32.4	6.6	Fumaroles
36	287023.3	9022660.7	Mataloko	82.5		26.9	27.1	26.0	1.2	Fumaroles
37	287026.9	9022661.2	Mataloko	94.3		27.7	27.9	27.4	6.2	Fumaroles
38	287083.4	9022635.4	Mataloko	77.4		21.9	21.4	21.5	2.7	Fumaroles
39	287075.4	9022609.2	Mataloko	46.2		21.4	21.8	21.9	2.1	Warm ground
40	287081.0	9022609.8	Mataloko	37.5		21.2	20.9	21.0	1.9	Warm ground
41	286794.5	9022616.9	Mataloko	72.5	73.0	35.0	33.3	33.6	7.2	Hot spring
42	286787.9	9022613.2	Mataloko	80.4	78.0	29.2	28.7	29.3	0.8	Hot spring
43	286784.5	9022602.8	Mataloko	88.8		28.7	28.0	28.4	2.9	Hot spring
44	286777.2	9022585.8	Mataloko	87.3		36.6	37.1	36.7	7.2	Mud pool
45	286793.9	9022570.6	Mataloko	82.4	81.0	27.1	26.3	26.6	1.9	Hot spring
46	286785.0	9022581.0	Mataloko	87.0		30.8	30.5	30.7	2.3	Mud volcano

ID	Coordinate X	Coordinate Y	Location	Fluke IR (°C)	Mercury therm. (°C)	Airborne temp. (°C) P0	P1	P2	Size (m²)	Type
47	286786.9	9022578.9	Mataloko	83.9		34.1	33.6	33.9	6.5	Hot spring
48	286833.0	9022523.9	Mataloko	46.2		22.6	22.8	23.2	2.5	Hot spring
49	286843.7	9022521.1	Mataloko	58.8		26.8	26.8	26.9	1.8	Hot spring
50	286844.3	9022518.8	Mataloko	60.0		28.0	27.9	28.6	1.2	Hot spring
51	286848.0	9022519.3	Mataloko	52.5		29.4	29.6	29.0	2.4	Hot spring
52	286854.4	9022518.9	Mataloko	57.4		26.7	26.8	26.7	1.5	Hot spring
53	286733.8	9022601.9	Mataloko	58.9		19.4	19.4	19.3	3.0	Hot spring
54	286694.3	9022598.6	Mataloko	48.1	46.0	21.6	21.5	21.8	1.4	Hot spring
55	286695.4	9022594.3	Mataloko	48.1		22.6	22.2	21.8	2.7	Hot spring
56	286623.3	9022555.9	Mataloko	47.9		26.8	26.8	26.4	2.3	Steaming ground
57	286630.5	9022586.1	Mataloko	89.6		25.3	24.7	24.5	3.5	Fumaroles
58	286617.8	9022582.1	Mataloko	78.7		20.2	20.3	19.9	1.9	Fumaroles
59	286607.0	9022531.5	Mataloko	49.9		35.1	35.2	34.7	2.6	Steaming ground
60	286602.1	9022529.3	Mataloko	49.6		31.0	31.6	30.8	3.4	Steaming ground
61	286622.0	9022503.0	Mataloko	80.5		27.8	27.6	27.2	1.3	Fumaroles
62	286621.6	9022507.8	Mataloko	84.8		32.1	31.7	31.4	3.7	Fumaroles
63	286576.6	9022517.0	Mataloko	53.1		27.8	28.1	28.0	2.8	Steaming ground
64	286570.8	9022517.6	Mataloko	76.3		27.4	27.6	27.6	1.9	Fumaroles
65	286568.3	9022518.3	Mataloko	53.1		31.5	31.7	30.9	2.0	Fumaroles
66	286568.6	9022521.3	Mataloko	86.9		33.8	34.0	33.8	9.7	Fumaroles
67	286529.2	9022503.3	Mataloko	83.3		40.5	41.4	41.2	16.4	Fumaroles
68	286534.7	9022496.6	Mataloko	45.0		27.7	27.7	27.6	8.3	Steaming ground
69	286543.0	9022497.1	Mataloko	86.7		28.2	28.2	27.9	2.8	Fumaroles
70	286527.8	9022491.9	Mataloko	76.0		36.0	36.3	35.8	31.5	Mud pool
71	286536.8	9022483.6	Mataloko	84.1		38.3	37.6	37.6	49.5	Mud pool
72	286493.4	9022476.3	Mataloko	83.8		38.3	38.2	38.4	47.9	Mud pool
73	286504.1	9022472.4	Mataloko	55.3		22.6	22.4	38.4	2.5	Mud pool
74	286499.2	9022480.8	Mataloko	54.1		30.2	29.1	29.1	2.5	Mud pool
75	286502.6	9022496.6	Mataloko	83.9		32.1	32.3	32.2	5.0	Mud pool
76	286509.1	9022497.5	Mataloko	85.6		28.6	28.4	28.6	5.3	Mud pool
77	286511.2	9022500.9	Mataloko	68.6		29.6	29.8	30.2	5.4	Mud pool
78	285450.3	9023322.5	Golewa	33.4		19.9	20.0	19.9	2.1	Warm spring

Appendix E – Documentation of the geothermal manifestations in Mataloko Geothermal Field

This appendix shows the location of geothermal manifestations that were measured during the fieldwork. This also shows the footages representing the actual expression of the geothermal manifestations. The identification number (ID) in the pictures correspond to ID number in appendix D.
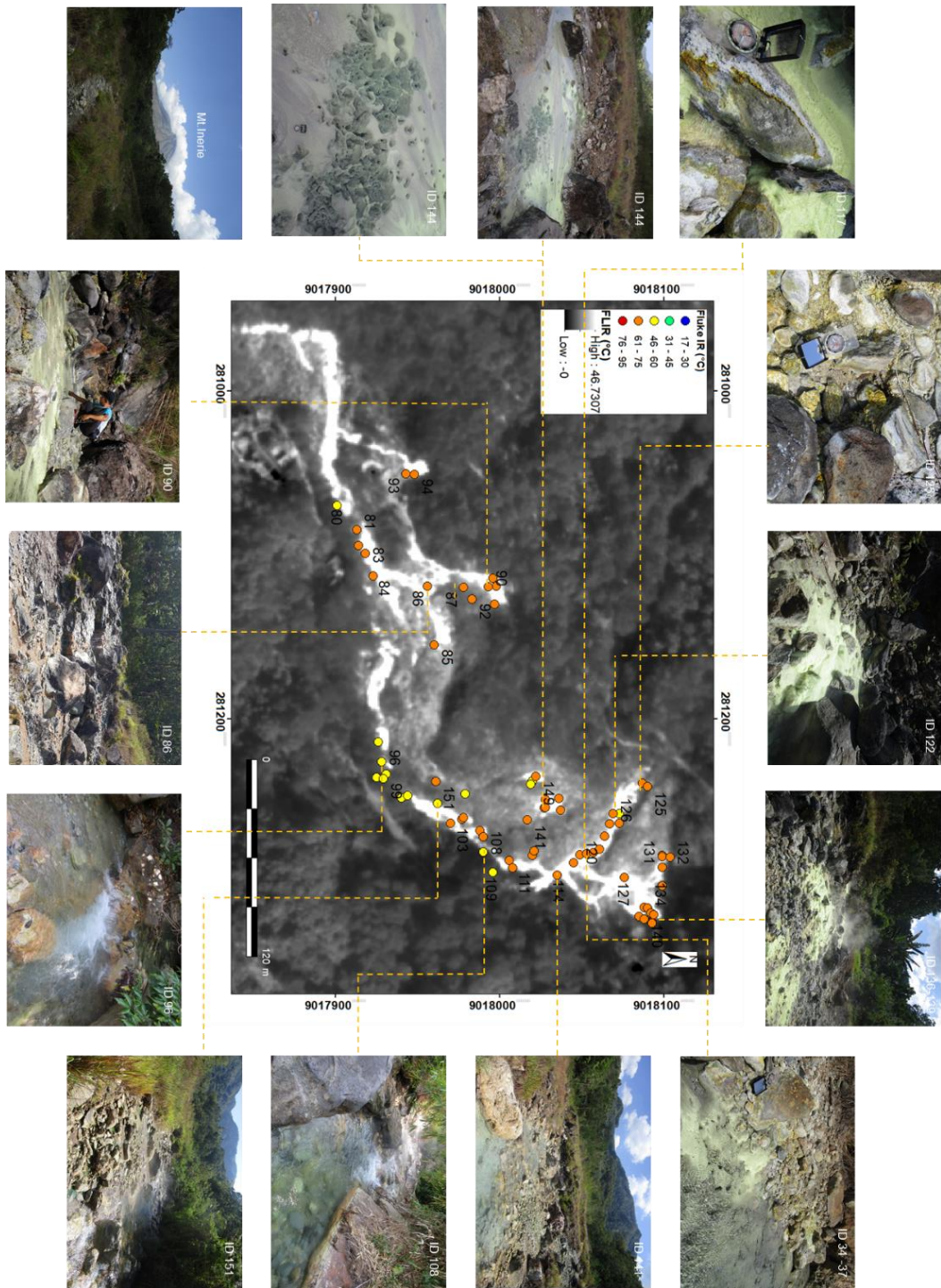

Location: Mataloko Geothermal Field (MGF)
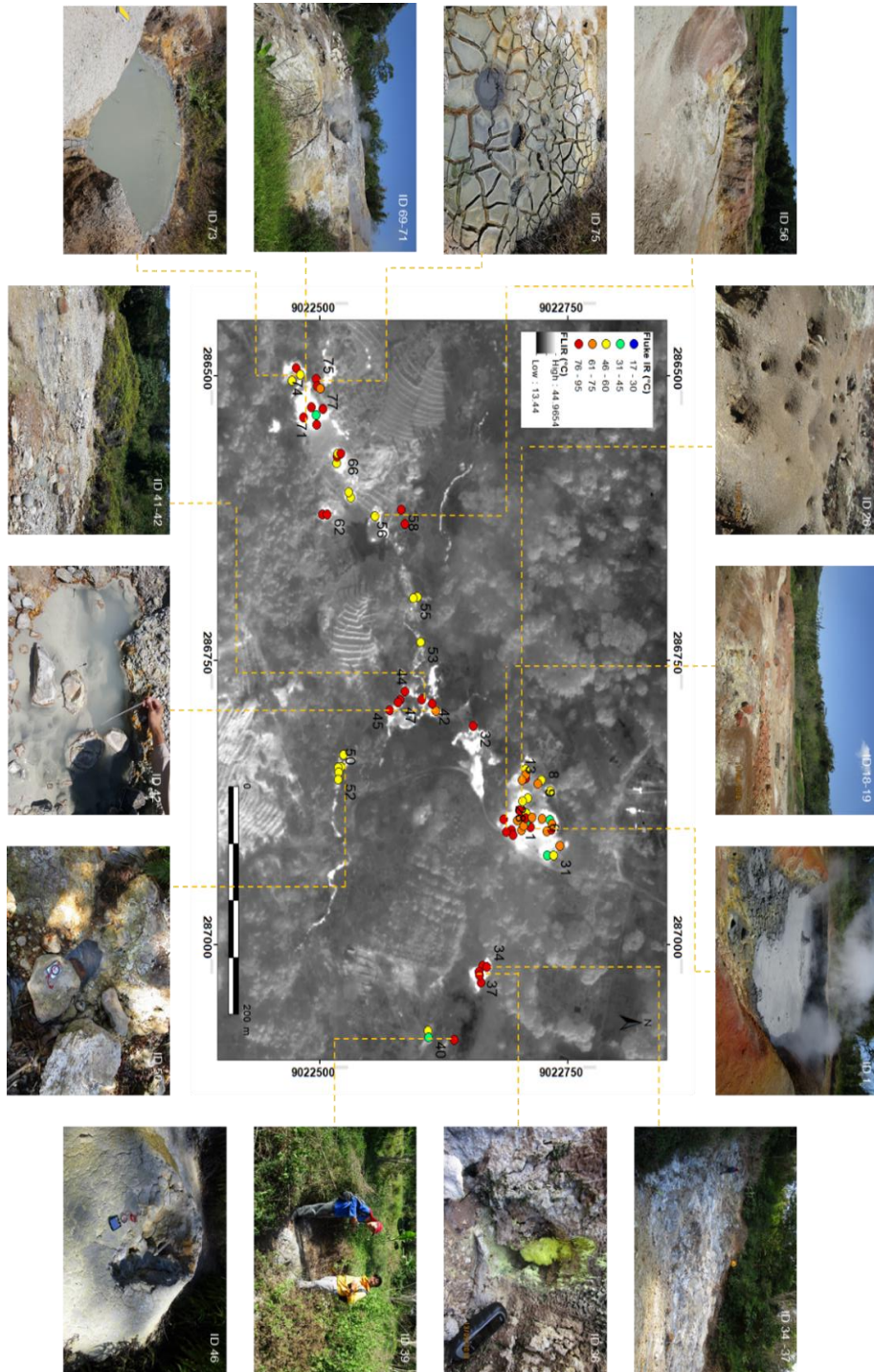
Appendix F – Documentation of the geothermal manifestations in Malanage area

This appendix shows the location of geothermal manifestations in Nage river that were measured during the fieldwork but are not covered by the airborne LiDAR data. This also shows the footages representing the actual expression of the geothermal manifestations (the next page). Here the hotspots mainly associated with hot springs with temperature ranging between 48 – 75°C. The detailed temperature measurements using Fluke IR and airborne TIR orthoimage (Preset 0) are given in the table below.

ID	Coordinate		Fluke IR (°C)	Airborne Preset0 (°C)	ID	Coordinate		Fluke IR (°C)	Airborne Preset0 (°C)
	X	Y				X	Y		
79	281069.6	9017901.0	58.6	40.6	115	281282.8	9018049.0	70.1	43.8
80	281084.4	9017913.0	68.4	27.6	116	281281.9	9018053.0	71.1	40.4
81	281094.1	9017914.0	69.4	40.3	117	281281.3	9018057.0	70.6	41.8
82	281099.1	9017918.0	68	40.0	118	281279.3	9018061.0	65.5	43.0
83	281113.0	9017923.0	65.1	40.5	119	281271.3	9018064.0	67.9	42.0
84	281154.9	9017960.0	71.2	43.4	120	281263.8	9018067.0	65.6	41.5
85	281119.0	9017956.0	61.8	38.0	121	281263.6	9018073.0	74	40.1
86	281119.6	9017978.0	65.6	28.1	122	281257.5	9018073.0	57.1	41.3
87	281114.1	9017996.0	67.6	40.7	123	281238.9	9018087.0	68	33.8
88	281118.9	9017998.0	70.6	43.3	124	281241.2	9018090.0	71.1	32.1
89	281119.4	9017993.0	70.9	40.8	125	281257.7	9018069.0	73.2	41.0
90	281130.1	9017997.0	71.2	41.2	126	281296.5	9018076.0	69.6	42.0
91	281127.1	9017983.0	72	25.4	127	281301.6	9018099.0	74.6	35.3
92	281050.4	9017943.0	70.6	40.9	128	281290.1	9018099.0	67.2	37.7
93	281050.9	9017948.0	71.7	42.9	129	281283.0	9018099.0	74.1	34.5
94	281213.8	9017926.0	55.1	41.1	130	281283.9	9018099.0	74	34.4
95	281225.8	9017928.0	56.2	33.8	131	281284.2	9018104.0	70	34.5
96	281233.6	9017931.0	56.4	29.9	132	281314.8	9018088.0	68.6	43.2
97	281235.5	9017925.0	56.7	22.3	133	281315.1	9018090.0	74.1	40.9
98	281236.4	9017929.0	56.7	28.7	134	281320.0	9018085.0	74.4	38.1
99	281248.1	9017940.0	57.1	25.1	135	281318.1	9018092.0	75	41.2
100	281246.7	9017944.0	57.3	37.9	136	281323.4	9018093.0	75.2	42.6
101	281251.4	9017962.0	57.6	41.0	137	281324.2	9018093.0	74.8	42.6
102	281263.4	9017970.0	61	40.5	138	281319.0	9018094.0	74	41.5
103	281261.0	9017977.0	65.3	39.9	139	281321.9	9018088.0	72.5	34.1
104	281260.0	9017978.0	61.4	41.1	140	281261.5	9018017.0	68.8	28.6
105	281268.1	9017988.0	64.4	40.5	141	281254.1	9018027.0	68	43.4
106	281271.8	9017990.0	63.9	35.0	142	281253.8	9018028.0	65.1	43.7
107	281280.9	9017990.0	59.8	32.6	143	281255.5	9018037.0	71.1	37.5
108	281293.2	9017996.0	60	35.4	144	281248.2	9018036.0	70.8	40.2
109	281286.1	9018006.0	61	37.2	145	281249.2	9018028.0	70.7	43.2
110	281290.5	9018008.0	61.2	36.6	146	281237.6	9018020.0	58.4	39.3
111	281283.1	9018020.0	67	28.2	147	281239.9	9018019.0	57.4	38.5
112	281280.3	9018021.0	68.7	27.6	148	281234.9	9018022.0	70.6	41.9
113	281295.1	9018035.0	63.8	43.6	149	281245.6	9017979.0	48	28.2
114	281287.4	9018045.0	66	43.9	150	281237.9	9017961.0	68.4	31.4

Location: Nage River

Appendix G – Documentation of the geothermal manifestations near Mt. Inielika

This appendix shows the location of geothermal manifestations near Mt. Inielika that were observed during the fieldwork. Some of them are located inside the study area such as the Wawomudha crater that was erupted in 2001, and some relict alterations located at the western flank of Wawomudha crater. Some manifestations are in the east side of the study area including Gou and Boba hot springs with water temperature is around 45°C. These hot springs location is not covered both in LiDAR and TIR images.

Location: Inielika volcanic complex